ISBN: 978-90-9026502-5

In Vivo Blood Analysis System

B. Iliev

In Vivo Blood Analysis System

Blagoy P. Iliev

In Vivo Blood Analysis System

Blagoy P. Iliev

In Vivo Blood Analysis System

Proefschrift

ter verkrijging van de graad van doctor
aan de Technische Universiteit Delft,
op gezag van de Rector Magnificus prof. ir. K. C. A. M. Luyben
voorzitter van het College voor Promoties,
in het openbaar te verdedigen op 17 januari 2012 om 10.00 uur

door

Blagoy Petrov ILIEV

Master of Science in Automatics and Circuit Engineering
Technical University - Sofia, Branch Plovdiv, Bulgaria
geboren te Smolyan, Bulgarije

Dit proefschrift is goedgekeurd door de promotor:
Prof. dr. ir. G. C. M. Meijer

Copromotor: Dr. G. A. M. Pop

Samenstelling promotiecommissie:

Rector Magnificus	voorzitter
Prof. dr. ir. G. C. M. Meijer	Technische Universiteit Delft, promotor
Dr. G. A. M. Pop	St Radboud UMC Nijmegen, copromotor
Prof. dr. P. J. French	Technische Universiteit Delft
Prof. dr. ir. N. de Jong	Erasmus MC Rotterdam
Prof. dr. D. J. G. M. Duncker	Earsmus MC Rotterdam
Prof. dr. J. Dankelman	Technische Universiteit Delft
Dr. S. N. Nihtianov	Technische Universiteit Delft
Prof. F. C. T. van der Helm	Technische Universiteit Delft, reservelid

This research was funded by the Dutch Technology Foundation STW (project DMR.5294) and Martil Instruments BV.

ISBN: 978-90-9026502-5

Printed in The Netherlands

Table of contents

List of constants and symbols

Physical constants

Symbol	*Name*	*Value*	*Unit*
F	Faraday constant	96 485.3383	$[C.mol^{-1}]$
q	Electron charge	$1.6022x10^{-19}$	[C]
k	Boltzmann's constant	$1.380622x10^{-23}$	$[J.K^{-1}]$
R	Universal gas constant	8.314472	$[J.K^{-1}.mol^{-1}]$
ε_0	Permittivity of free space	$8.8542.10^{-12}$	$[F.m^{-1}]$

Variables (Roman)

Symbol	*Name*	*Unit*
A	Area	$[m^2]$
C	Capacitance	[F]
C_m	Cell membrane capacitance	$[F.m^{-1}]$
C_b	Whole blood capacitance	$[F.m^{-1}]$
C_{0m}	Specific cell membrane capacitance	$[F.m^{-2}]$
C_d	Double layer capacitance	$[F.m^{-2}]$
C_e	Red-blood-cell form factor constant	[-]
C_s	Stray capacitance	[F]

D	Diameter	[m]
E	Half-cell potential	[V]
E^0	Electrode potential	[V]
F	Force	[N]
G	Transimpedance conversion factor	[Ω]
f	Frequency	[Hz]
f_r	Relaxation frequency	[Hz]
f_{res}	Resonance frequency	[Hz]
Ht	Hematocrit	[%]
k	Cell constant	[m^{-1}]
L	Length	[m]
N	Suspended-particles-geometry constant	[-]
n^0	Ion bulk concentration	[$mol.m^{-3}$]
p	Pressure	[Pa]
Q	Volumetric flow rate	[$m^3.s^{-1}$]
Q	Quality factor	[-]
r	Distance	[m]
R	Radius	[m]
Re	Reynolds number	[-]
R_e	Electrode resistance	[Ω]
R_b	Specific whole blood resistance	[Ω.m]
R_o	Amplifier output resistance	[Ω]
R_p	Specific plasma resistance	[Ω.m]
T	Absolute temperature	[K]
T_p	Patient temperature	[ºC]
T_{ref}	Reference temperature	[ºC]
U_g	Gain channel voltage (Phase gain analyzer)	[V]
U_{gslp}	Gain channel slope voltage (Phase gain analyzer)	[V/decade]
U_I	Current channel voltage	[V]
U_{phs}	Phase channel voltage (Phase gain analyzer)	[V]
U_{pslp}	Phase channel slope voltage (Phase gain analyzer)	[V/deg]
U_s	Excitation source voltage	[V]
U_U	Voltage channel voltage	[V]
U_z	Voltage over the measured impedance	[V]
v	Flow velocity	[$m.s^{-1}$]
Δp	Pressure gradient	[Pa]
Δx	Relative displacement	[m]
Δy	Body height	[m]
z	Charge magnitude	[C]
Z_b	Specific blood complex impedance	[Ω.m]

Variables (Greek)

Symbol	*Name*	*Unit*
α	Flow curve slope angle	[rad]
α_p	Specific plasma resistance temperature coefficient	[$^oC^{-1}$]
δ	Nernst diffusion layer thickness	[m]
ε	Permittivity	[$F.m^{-1}$]
ε^*	Complex permittivity	[$F.m^{-1}$]
ε_r	Relative permittivity	[-]
$\bar{v}$	Mean velocity	[$m.s^{-1}$]
γ	Shear strain	[-]
$\dot{\gamma}$	Shear rate	[s^{-1}]
η	Viscosity	[Pa.s]
η^*	Complex coefficient of viscosity	[Pa.s]
κ	Debye length	[m]
ρ	Fluid density	[$kg.m^{-3}$]
ρ_p	Specific plasma resistance	[Ω.m]
σ	Electrical conductivity	[$S.m^{-1}$]
σ^*	Complex conductivity	[$S.m^{-1}$]
σ^M	Surface charge concentration	[$C.m^{-2}$]
τ	Shear stress	[Pa]
τ	Time constant	[s]
τ_a	Erythrocyte aggregation time constant	[s]
τ_d	Relaxation time	[s]
τ_{da}	Erythrocyte disaggregation time constant	[s]
τ_y	Yield stress	[Pa]
Φ	Spatial potential	[V]
Φ_0	Potential difference	[V]
ζ	Zeta potential	[V]

Introduction 1

The thesis before you describes a newly developed online hematology and cardiology diagnostic system designed to perform the electrical analysis of whole blood *in vivo*. From the electrical parameters of whole blood, the system derives a number of blood rheological characteristics, the most important of which is whole blood viscosity.

1.1 Motivation

Several studies have shown that blood electrical impedance and in particular two of its components–plasma resistance R_p and cell membrane capacitance C_m–can be of a great value for the development of biomedical instrumentation [1.1-1.5]. There is clear evidence that the last two parameters can be correlated with the hematocrit *Ht* [1.6] and whole blood viscosity η, respectively [1.7, 1.8].

Blood is a suspension of red cells (RBC), white cells, and platelets in plasma. A simplified three-element electrical model (Fig. 1-1) was first described by Hugo Fricke [1.6]. The volume of red blood cells is called hematocrit, which in the equivalent electrical model is associated with R_p. The interior resistance of the cell is represented by R_i, while the bulk cell membrane capacitance, depicted by C_m, shows a high degree of

correlation with the whole blood viscosity and therefore is considered to be a reliable measure for it.

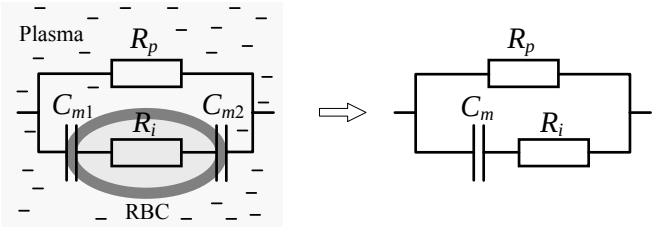

Figure 1-1: *Whole blood equivalent electrical model. The left-hand side shows an impression of the electrical model related to the properties of blood plasma and the red blood cells. The right-hand side shows the resultant equivalent electrical model of whole blood.*

Whole blood viscosity is mainly determined by the hematocrit, but also by the presence of aggregating proteins, such as the acute-phase proteins fibrinogen and C-reactive protein (CRP). Blood is a non-Newtonian liquid, which means that its viscosity varies according to the shear rate. At a lower shear rate, blood viscosity increases sharply. Hence, although R_p is an accurate measure for the hematocrit it is not sufficient to reflect the level of blood viscosity. A proper viscosity measurement requires an accurate C_m estimation which also takes into account the presence of the acute-phase proteins and the shearing properties of the sample being tested.

In the pathophysiology of vascular diseases, blood viscosity is a major factor, having implications in the hemodynamic load of the heart and the tissue perfusion [1.8-1.12]. The hemodynamic significance of blood viscosity is depicted in the Hagen-Poiseuille law:

$$\eta = \frac{R^4 \pi \Delta p}{8LQ} \quad , \tag{1-1}$$

where Q is the volumetric flow rate through a vessel, R is the vessel's internal radius, and Δp is the pressure difference that creates the flow between two points which are at a distance L apart.

An elevated blood viscosity increases the thromboembolic risk and can also be correlated with systemic inflammatory activities [1.13-1.15].

1.2 Objectives

Despite the obvious applicability of measuring whole blood viscosity in many clinical areas, scientists have failed so far to introduce it into the daily clinical practice. The main reason for this lies in the fact that blood viscosity strongly depends on the shear rate, as a result of which the *in vitro* whole blood analysis draws a significantly inaccurate representation of the actual *in vivo* situation. For example, by using an *in vitro* viscometer, one can measure the viscosity of a blood sample taken from the right atrium; however, the measured value will not reflect the actual *in vivo* viscosity level because the exact shear rate in the atrium at the moment when the sample is collected is unknown. This invalidates the viscometer results, which are measured at an assumed theoretically defined shear rate. In addition, blood changes rapidly in rheological terms once it is outside of the body. The unavoidable addition of anticoagulants distorts the measurement results even further.

Considering the afore-listed technical difficulties and the potential clinical significance of whole blood viscosity, which clinicians have not been adequately aware of until now, we have defined the following as the main objectives of our work:

- Performing a controlled *in vitro* characterization of R_p versus hematocrit and C_m versus whole blood viscosity and deriving the corresponding correlations.
- Developing an *in vivo* whole-blood viscosity analysis sensor, which is based on blood electrical-impedance measurements.
- Developing an electronic device to interface the above-mentioned sensor.
- Validating the derived R_p versus hematocrit and C_m versus whole-blood viscosity correlations in an *in vivo* setting, i.e. conducting a clinical trial.

Before we define the places these objectives take in the thesis structure, we should mention that the sensor carrier has been preliminarily selected. It is a standard central venous catheter, which is widely used in modern clinical practices and is proven to be a feasible option as far as an *in vivo* blood electrical-impedance analysis is concerned [1.16].

1.3 Organization of the thesis

Chapter 2 describes the composition of blood and its rheology. The essence of whole blood viscosity and the related key blood analysis issues are revealed in detail. This chapter also discusses the clinical relevance of whole blood viscosity.

Chapter 3 describes the electrical aspects of blood analysis. It explores the challenges the complex impedance measurement techniques face when analysing physiological phenomena and recording bioelectrical events. This chapter also gives a detailed theoretical explanation of the equivalent electrical model of whole blood.

Chapter 4 lists the design considerations used to create and optimize an *in vivo* electrical impedance sensor. The interface electronics developed and the biocompatibility, electromagnetic and safety features incorporated into the complete system can be found in this chapter as well.

Chapter 5 depicts the results derived during an *in vitro* study with human blood and a human *in vivo* pilot study in patients who underwent an autologous peripheral blood stem-cell transplantation.

Finally, Chapter 6 draws the conclusions deduced as a result of our work and shows a number of directions, in which the system can be further improved.

1.4 References

1.1 H. P. Shwan, “The Practical Success of Impedance Techniques from an Historical Perspective”, Annals of the New York Academy of Sciences, 1999, Vol. 873, pp. 1-12

1.2 J. Nyboer, “Electrorheometric properties of tissues and fluids”, Int. Conf. on Bioelectrical Impedance, 30 July, 1970, ed S. E. Markovich Ann. NY Acad. Sci. 170, pp. 410–20

1.3 Tian-xian Zhao, Bertil Jacobson and Tommy Ribbe, “Triple-frequency method for measuring blood impedance”, Physiol. Meas., Vol. 14, 145-156, 1993, UK

1.4 A. Pribush, D. Meyerstein, N. Meyerstein, “Study of red blood cell aggreagtion by admitance measurements”, Biorheology, Vol. 33, No. 2, 1996, pp. 139-151

1.5 Tian-Xian Zhao, B. Jacobson, “Quantitative correlation among fibrinogen concentration, sedimentation rate and electrical impedance of blood”, Medical & Biological Engineering & Computing, May 1997, pp. 181-185

1.6 H. Fricke, S. Morse, “The electrical resistance and capacity of blood for frequencies between 800 and $4\frac{1}{2}$ million cycles”, The Journal of General Physiology 9, pp. 153-157, 1925

1.7 G. A. M. Pop, W. J. Hop, L. Moraru, M. van der Jagt, J. Quak, D. Dekkers, Z. Chang, F. J. Gijsen, D. J. Duncker, C. J. Slager, “Blood electrical impedance closely matches whole blood viscosity as parameter of hemorheology and inflammation”, Applied Rheology, 2003, Vol. 12, pp. 305-312

1.8 G. A. M. Pop, D. J. Duncker, M. Gardien, P. Vranckx, S. Versluis, D. Hasan, C. J. Slager, “The clinical significance of whole blood viscosity in (cardio)vascular medicine”, Netherlands Heart Journal, Volume 10, December 2002, pp. 512-516

1.9 O. K. Baskurt, “Pathophysiological significance of blood rheology”, Turk J Med Sci, 2003, Vol. 33, pp. 347-355

1.10 M. Woodward, A. Rumley, H. Tunstall-Pedoe, G. D. O. Lowe, “Does sticky blood predict a sticky end? Associations of blood viscosity, haematocrit and fibrinogen with mortality and the West of Scotland”, British Journal of Haematology, 2003, Vol. 122, pp. 645-650

1.11 E. W. Merrill, E. R. Gilliland, G. Cokelet, H. Shin, A. Britten, R. E. Wells, “Rheology of blood and flow in the microcirculation “, J Appl Physiol, 1963, Vol. 18, pp. 255-260

1.12 S. K. Jeong, Y. I. Cho, M. Duey, R. S. Rosenson, “Cardiovascular risks of anemia correction with erythrocyte stimulating agents: should blood viscosity be monitored for risk assessment?”, Cardiovasc Drugs Ther., 2010 Apr; 24(2), pp. 151-60

1.13 R. Ben Ami, G. Barshtein, D. Zeltser, Y. Goldberg, I. Shapira, A. Roth, G. Keren, H. Miller, V. Prochorov, A. Eldor, S. Berliner and S. Yedgar, “Parameters of red blood cell aggregation as correlates of the inflammatory state”, AJP - Heart, 2001, Vol. 280, pp. 1982-1988

1.14 G. D. Sloop, “A unifying theory of atherogenesis”, Medical Hypotheses, 1999, Vol. 47, pp. 321-325

1.15 R. Ross, “The pathogenesis of atherosclerosis: an update” New Engl Med, 1986, pp. 488-500

1.16 G. A. M. Pop, Z. Chang, C. J. Slager, B. J. Kooij, E. D. van Deel, L. Moraru, J. Quak, G. C. M. Meijer, D. J. Duncker, “Catheter-based impedance measurements in the right atrium for continuously monitoring hematocrit and estimating blood viscosity changes; an in vivo feasibility study in swine”, Biosensors and Bioelectronics, 2004, Vol. 19, pp. 1685-169

2 *Basic concepts and clinical aspects of blood rheology*

This chapter describes the basics of blood rheology and the related clinical aspects. The latest are explored and applied to real clinical situations. To this end, the clinical relevance of blood rheology is revealed and the potential benefit of measuring blood rheological properties is explained.

2.1 Blood constituents

Blood takes up approximately 7% to 9% of the total body weight of an adult person. An averaged-sized man has 5 to 6 litres of blood, and an averaged-sized woman has 4 to 5 litres of blood [2.1, 2.2]. While circulating through the body, blood performs three basic functions:

- Transport of oxygen from the lungs to body tissues; transport of the waste products for eventual removal from the body; and transport of nutrients, hormones, and enzymes through the body.
- Regulation of body temperature by adjusting the flow to the skin for optimal heat exchange; regulation of pH through the distribution of buffers; and regulation of renal control over the amount of water and electrolytes.

- Protection against harmful substances by contributing white cells, proteins and antibodies to the immune and inflammatory reactions. Additionally, blood contains a subtle balance of clotting factors to prevent bleeding, and lytic factors to prevent clotting.

The work presented in this thesis has a direct or indirect link to all three functions. Measuring of the number of cells in whole blood can be associated with the transport mechanism. The regulatory function can be evaluated by observing the blood flow, which depends on whole blood viscosity. As blood viscosity is altered by protein levels, it may also serve as an inflammation marker.

2.1.1 Cellular phase

Blood is a suspension of red blood cells (RBC or erythrocytes), white blood cells (leukocytes), and platelets (thrombocytes) in plasma. The cells make up approximately half of the volume of human blood. Most are erythrocytes–almost 95%. Less than 0.15% of the volume consists of leukocytes and the remaining, close to 5%, consists of thrombocytes.

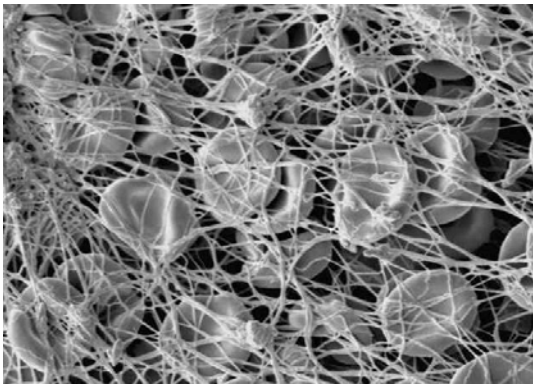

Figure 2-1: *Red blood cells trapped in a fibrinogen net.*

An erythrocyte resembles a biconcave disk that is 7 μm in diameter and about 2 μm thick (Fig. 2-1). This shape provides a large surface area for gas diffusion and ensures greater flexibility when passing through the capillaries. There are about 5.5 million erythrocytes per cubic millimeter in the blood of an adult male and about 4.8 million in the blood of an adult female, respectively. The volume percentage of RBC in whole blood is

called hematocrit (*Ht*). Typically, *Ht* ranges from 40% to 45% for males and from 36% to 41% for females.

Almost the entire weight of an erythrocyte consists of hemoglobin, which is enveloped by a thin cell membrane (plasma membrane) [2.3, 2.4]. Hemoglobin is a globular protein. Its ability to combine with oxygen defines the main role of the erythrocytes, i.e. to transport oxygen from the lungs to body tissue. The cell membrane that separates the intracellular from the extracellular volume is a structured bilayer of phospholipids and protein molecules. It allows transport of water, oxygen, carbon dioxide, glucose, urea, etc., but it prevents hemoglobin and other large proteins from passing through. The phospholipid bilayer is electrically inert. It is very thin, which results in high specific electrical membrane capacitance (C_{0m}), in the order of 0.8 $\mu F.cm^{-2}$ - 1 $\mu F.cm^{-2}$ [2.5].

An average adult has between 4000 and 11000 leukocytes per cubic millimeter. In the case of infection this amount might rise up to 25000 per cubic millimeter. The main function of leukocytes is to destroy microorganisms at infection sites and remove foreign molecules or debris that result from dead or injured tissues.

Thrombocytes are more numerous than leukocytes–more than 150000 per cubic millimeter for an adult. They are four times smaller than the erythrocytes and their main function is to start the process of blood clotting to prevent bleeding in the case of injured blood vessels.

The functions of leukocytes and thrombocytes and their properties are beyond the scope of the current work and therefore will not be examined in details.

2.1.2 Blood plasma

Blood cells are suspended in plasma. It is the liquid part of blood and consists of about 90% water content. The water maintains the body's hydration and serves as a solvent for both extracellular and intracellular chemical reactions. Some 7% of the plasma belongs to a group of proteins. The remaining 3% is composed of electrolytes, amino acids, glucose, nutrients, various enzymes, hormones, metabolic wastes, and traces of other organic and inorganic compounds.

There are three groups of plasma proteins: albumins, globulins and fibrinogen. The albumins, which comprise about 60% of all proteins, promote water retention in the blood in order to maintain normal blood volume and pressure. The globulins are about 36% of all plasma proteins. They are responsible for the transport of lipids, fat-soluble vitamins,

cholesterol and triglycerides between the liver and various body cells. Some globulins play role of antibodies that help to prevent diseases such as measles, tetanus, and poliomyelitis. The last in the group of plasma proteins is fibrinogen. It is only 4% of all proteins but plays an essential role in erythrocyte aggregation and blood clotting [2.6, 2.7]. The last two mechanisms are strongly related to blood viscosity [2.8], which is one of the main topics of this research.

Of the remaining 3% of plasma, our focus will be on the electrolytes only. These include the cations – sodium Na^+, potassium K^+, calcium Ca^{2+}, magnesium Mg^{2+} and the anions – chloride Cl^-, bicarbonate HCO_3^-, phosphate HPO_4^{2-}, and sulfate SO_4^{2-}. What will be important for our work are those ions that influence the electrical properties of plasma and especially the specific plasma resistance (ρ_p).

2.2 Blood rheology

Rheology is the study of deformation and flow of matter. One of the major issues it deals with is viscosity. Viscosity is a measure of a fluid's intrinsic resistance to flow. In blood it arises from the frictional interaction between all major blood constituents: plasma, plasma proteins and blood cells. Red blood cells, being the main constituent of the cellular phase of blood, greatly influence whole blood viscosity. At low shear, blood cells aggregate, which induces a sharp increase in viscosity, while at high shear, blood cells disaggregate, deform and align in the direction of flow. In addition, whole blood viscosity is affected by the presence of macromolecules in the medium, by the temperature, and by the deformability of the cells [2.9, 2.10].

Whole blood viscosity has a significant clinical relevance. Its most important role is in microcirculation, where it contributes significantly to the peripheral resistance and may cause sludging in the postcapillary venules. At the sites of severe atherosclerotic obstructions or at vasospastic locations, where a change in vessel diameter is limited, blood viscosity contributes to stenotic resistance by obstructing tissue perfusion. Besides the haemodynamic effects, an increase in blood viscosity at a low shear rate and as a result of RBC aggregation is associated with a thrombotic risk. Moreover, an increased aggregation is a good marker for inflammatory activity [2.11, 2.12].

Apart from the direct clinical relevance, blood viscosity and flow dynamics indirectly influence the electrical parameters of flowing blood.

Consequently, these electrical parameters can be associated with the aforementioned clinical aspects. However, proper understanding of blood viscosity and rheology mechanisms is essential before deriving any correlations between particular electrical parameters and the corresponding clinical ones.

2.2.1 Shear stress, shear rate, viscosity, viscoelasticity

Every material body subjected to external forces changes shape and size. Such a change involves displacement of material points within the body, which is referred to as deformation. If this deformation changes continuously over time, the body can be defined as flowing. In this sense, three main categories of materials can be distinguished: solids, fluids, and viscoelastic materials. Viscoelastic materials display a combination of solid and fluid behaviours. Since blood is a mixture in which separate particles (blood cells) are suspended in a viscous liquid (plasma), it therefore falls into the category of viscoelastic materials [2.9, 2.13].

A viscous-fluid material flows continuously when any unbalanced forces are applied to it. If the flow rate is proportional to the applied forces, the fluid is called Newtonian. Newtonian fluids are also referred to as linear fluids. Blood is a non-Newtonian, nonlinear liquid the flow rate of which is not proportional to the applied forces. What does this mean? Let us assume that the degree of deformation of a body depends on the force applied per unit area. Then the stress τ is defined as:

$$\tau = \frac{F}{A} \quad , \tag{2-1}$$

where F is the force and A is the area. In principle, F can be split into two components: parallel and perpendicular to the surface. The force per unit area acting parallel to A is defined as shear stress τ (in [N/m^2] or [Pa]). Figure 2-2 illustrates a body subjected to shear stress. The resultant deformation is known as shear strain and equals:

$$\gamma = \frac{\Delta x}{\Delta y} \quad , \tag{2-2}$$

where Δx is the relative displacement of the top layer versus the bottom layer, and Δy is the body height.

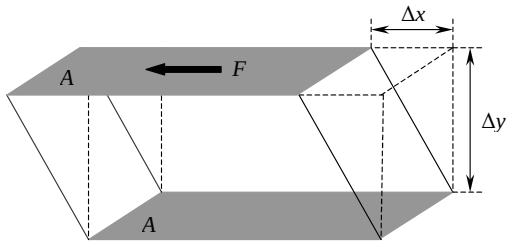

Figure 2-2: *Body subjected to shear stress by shear force F.*

In a flow situation where continuing deformation is observed, the shear rate is defined as the shear deformation in unit time. The shear rate is also known as a velocity gradient, which is measured in [s^{-1}]:

$$\dot{\gamma} = \frac{\Delta v}{\Delta y} \quad , \tag{2-3}$$

where $\Delta v = v_1 - v_2$ is the difference in velocity, as depicted in Fig. 2-3.

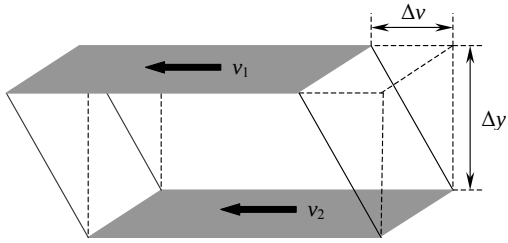

Figure 2-3: *Velocity gradient between two parallel laminas.*

A fluid is defined as viscous when the shear rate is a function of the shear stress. For a linear (Newtonian) fluid, viscosity is expressed as the ratio of the shear stress and shear rate:

$$\eta = \frac{\tau}{\dot{\gamma}} \quad . \tag{2-4}$$

The basic unit for viscosity is [Pa.s] (Pascal-second). For a non-Newtonian fluid this function is nonlinear. In a more digestible

manner this means that a Newtonian fluid has constant viscosity at all shear rates (Fig. 2-4a) while a non-Newtonian fluid viscosity varies with the shear rate (Fig. 2-4, b and c). Figure 2-4 shows the measured viscosity, using a Contraves LS30, of two blood samples with a hematocrit of 46% (curve b) and 31% (curve c), respectively. Curve "a" reflects the behaviour of a Newtonian fluid. The increase in viscosity at a low shear rate is due to an effect called cell aggregation. At a high shear rate, blood cells disaggregate and viscosity drops significantly.

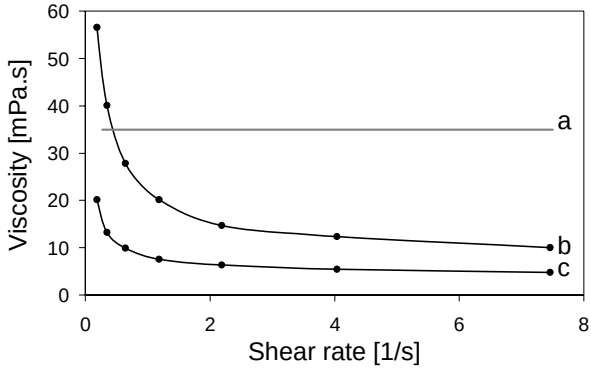

Figure 2-4: *Viscosity versus shear rate of two blood samples with a hematocrit of 46% (b) and 31% (c), respectively. Curve "a" is theoretical and represents Newtonian liquid.*

The difference between Newtonian and non-Newtonian liquid can also be nicely illustrated by plotting their respective flow curves (Fig. 2-5).

A Newtonian liquid exhibits a straight-line flow curve (Fig. 2-5b), the slope of which is a measure of the viscosity

$$\eta = \tan \alpha \quad . \tag{2-5}$$

The flow curve of blood is not a straight line and starts at a finite shear stress, τ_y, called yield stress.

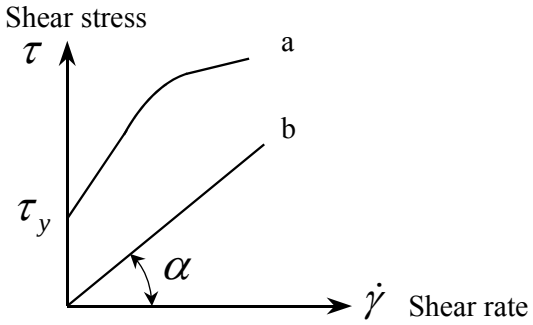

Figure 2-5: *Flow curves of blood (a) and a Newtonian liquid (b).*

The flow behaviour of some non-Newtonian liquids, including blood, depends on their shearing history. Consequently, the liquid properties may also be time-dependent. For example, blood has a high viscosity when first sheared. As time progresses, viscosity decreases and this phenomenon is repeatable after the sample is allowed to rest for a while. This is usually a result of a partial destruction of internal structures, e.g. cell formations, caused by the shearing. While at rest, the internal structures may build up again, recovering some of the initial liquid properties. Thus, whole blood demonstrates viscous and elastic properties and is therefore associated with the group of viscoelastic materials.

In order for blood to flow easily, the size of the cell aggregates must be reduced. The disaggregating forces also produce an elastic deformation and orientation of the cells. Consequently, some elastic energy is stored in the cellular structure of blood. In a further flow process, the sliding of the cellular structure requires a continuous input of energy, which is dissipated by the viscous friction. The viscous and elastic components of whole blood are expressed by the complex coefficient of viscosity:

$$\eta^* = \eta' - \mathrm{i}\,\eta'' \quad , \tag{2-6}$$

where η' and η'' are the real and imaginary part of viscosity [2.10]. The viscous component η' is associated with the energy dissipation, while η'' is the elastic component and is associated with the energy storage. Both components depend on the hematocrit and shear rate. At a very low hematocrit, η'' is almost undetectable. With the increased energy-storage capabilities at a high hematocrit, η' and η'' approach stable values when

the shear rate is low. A higher shear rate results in a decrease in η', which finally tends to settle at a constant value. A similar trend is observed with η''. However, albeit slightly, it continues to decrease when the shear rate is further elevated. It is evident that the deformability of the red blood cells has a large influence on the viscoelasticity and hence on whole blood viscosity, especially at high shear rates.

2.2.2 Plasma viscosity

Plasma viscosity is determined by its dissolved macromolecular components and its primary component, water [2.9, 2.13, 2.14]. Being a fluid with dissolved macromolecular structures, plasma behaves slightly as a non-Newtonian liquid. It has a viscosity of about 1.2 mPa.s at 37°C. The contribution of each individual protein to the viscous component of plasma is a function of its concentration, mass and shape of the molecule. Fibrinogen, having the longest dimension of any of the other constituents (about 50 nm), has a strong effect on plasma viscosity. Immunoglobulins additionally demonstrate high capacity for increasing plasma viscosity. Smaller globular molecules, for example albumin, are less influential. Nevertheless, the high concentration they may have can make them relevant as well [2.15]. Serum–plasma from which the clotting factors such as fibrinogen have been removed–has about a 0.1 mPa.s to 0.15 mPa.s lower viscosity than that of plasma. This is due to the fibrinogen extraction. Plasma viscosity is found to be dependent on the age and sex for different individuals but it shows small interindividual variation.

2.2.3 Blood viscosity

The fluid properties of blood are determined by various factors such as shear properties, temperature, deformability and concentration of the red blood cells, plasma viscosity, and the interaction between the cellular and liquid phase of blood. Such interaction creates the erythrocyte aggregates, which are formed as a result of bridging between the cells. The bridging is helped by the plasma proteins, fibrinogen and globulins that are absorbed at the cell surface. The process of aggregation and the forces involved are counteracted by an electrostatic repulsion and by the mechanical shearing; therefore this effect is fully reversible and occurs mainly at low shear rates [2.6, 2.8, 2.15-2.29]. In fact, almost none of the aforementioned effects contribute to the viscosity of blood independently

and often one is the consequence of another. Frequently, this causes misunderstandings and may even lead to the wrong conclusions, so let us start with a brief grouping based on the shear properties [2.16-2.19]. At low shear rates ($\dot{\gamma} < 1\ s^{-1}$), red blood cells form polymerized cell networks and blood response resembles plastic-like characteristics. With such shear properties, the important viscosity determinants are cell aggregation, adhesive strengths, and cell deformability. At intermediate shear rates ($1\ s^{-1} < \dot{\gamma} < 50\ s^{-1}$), cell aggregates are dispersed and individual cells are deformed. Cell rigidity and conformation become important properties in this shear range, where plasma proteins have a diminished influence on the viscous characteristics. Finally, at high shear rates ($\dot{\gamma} > 50\ s^{-1}$), all aggregates are fully dispersed as cells are continuously deformed. Viscosity is no longer dependent on aggregates and plasma proteins, and is mainly determined by the hematocrit. However, let us not forget that hematocrit is the main determinant of blood viscosity in the entire shear range. Unlike red blood cells, white blood cells and thrombocytes have very little effect on bulk viscosity in normal concentrations.

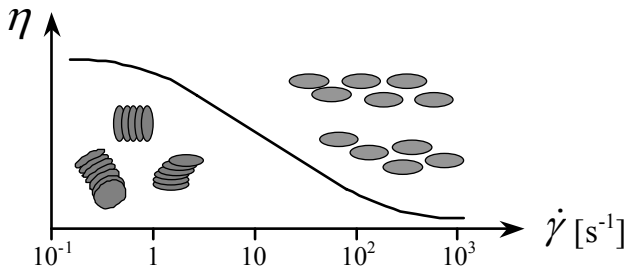

Figure 2-6: *Typical viscosity versus shear rate curve and the corresponding cell formations.*

The effect of hematocrit on whole blood viscosity can be explained by adopting the theoretical considerations related to suspensions, where rheological properties are strongly influenced by the suspended particle concentration. For blood, the relationship between viscosity and *Ht* can be approximated by the function:

$$\log \eta = k + k'Ht \quad , \tag{2-7}$$

where k and k' are constants, related to the specific blood sample [2.15, 2.19, 2.20]. In particular, k represents plasma viscosity, while k' is a function of the shear properties of the liquid. Adopting a universal, concrete formula is challenging, since k and k' may demonstrate considerable spread for different groups of test subjects. Also, note that the shear properties must be well defined as far as viscosity versus hematocrit characterization is concerned. In addition, the comparison of two blood samples in terms of viscosity is relevant only when performed at a fixed, "standard" hematocrit. Figure 2-7 shows the change in whole blood viscosity versus *Ht* at different shear rates measured with a Contraves LS30.

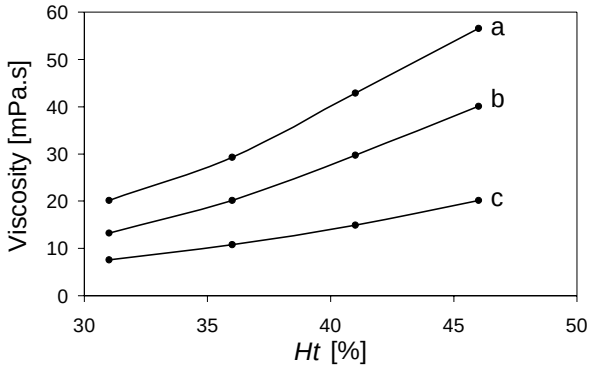

Figure 2-7: *Viscosity versus hematocrit measured at shear rates of 0.19 s^{-1} (a), 0.35 s^{-1} (b) and 1.18 s^{-1} (c).*

The results shown in Fig. 2-7 were obtained by means of dilution with Voluven. The fibrinogen level was not kept constant and was 5.7 g/l at the highest hematocrit, and 2.8 g/l at the lowest hematocrit, respectively. However, additional measurements have shown that fibrinogen is far less influential than the hematocrit with respect to whole blood viscosity.

All blood cells tend to participate in aggregation reactions. Rouleaux are the most spread cell aggregates (Fig. 2-8). They are created by red blood cells and in the presence of macromolecules such as fibrinogen. Such muticellular structures provoke increased viscosity and affect blood flow [2.6-2.8, 2.16-2.18, 2.21-2.26].

Besides the rheology of blood, rouleaux formations substantially affect *in vivo* hemodynamics and can seriously disturb the red blood cell distribution and flow dynamics in the microcirculation [2.11]. Moreover,

the level of aggregation may rise enormously in some clinical disorders such as sepsis, diabetes, myocardial ischaemia, and renal failure.

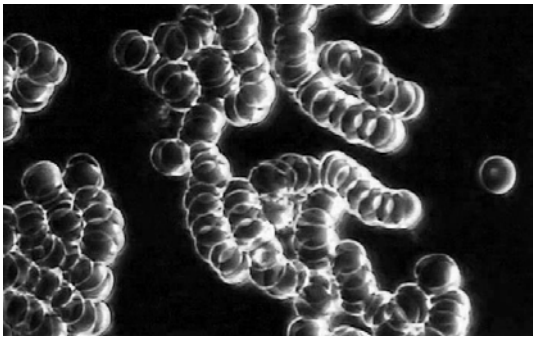

Figure 2-8: *Rouleaux formations.*

There are two basic hypotheses on how and why aggregates are formed: cross-bridging hypothesis and depletion layer hypothesis [2.21]. The bridging is thought to occur when the bridging forces, which are due to adsorption of macromolecules onto an adjacent cell surface, exceed the disaggregating forces. The disaggregating forces arise from electrostatic repulsion, membrane strain or mechanical shearing. In the depletion model, aggregation is associated with the osmotic gradient and movement of fluid away from the intercellular gap, thus promoting aggregation by decreasing cell-solvent affinity. Surprisingly, this can occur only at lower protein or polymer concentrations near the cell versus the suspending medium surface. The contradiction is evident as the bridging model predicts a higher aggregation tendency at higher protein and polymer concentrations, whereas the depletion model states the opposite. Based on the experience of the majority of authors [2.6, 2.8, 2.17, 2.20, 2.23, 2.24], as well as on our own experience (Fig. 2-9), we strongly believe in the bridging hypothesis.

Some cell-specific factors are found to have a certain role in the formation of aggregates as well. These are cell age, cell surface charge arrangement [2.23], cytoplasmic and membrane viscosity, etc. Yet, while inflammatory reaction is in the focus of our investigation, we shall concentrate on the protein-induced aggregation (Fig. 2-9), and specifically on fibrinogen, which is the most important bridging macromolecule. Other cell-specific factors causing cell aggregation will be neglected for the moment.

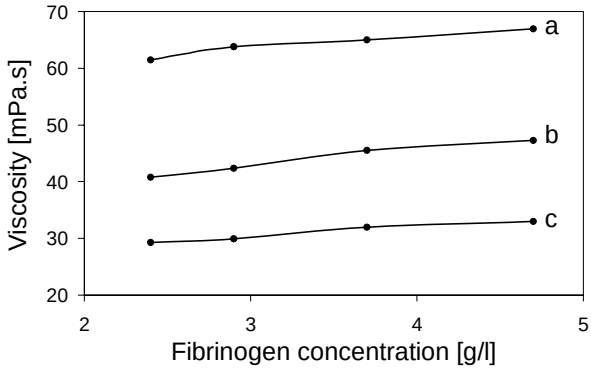

Figure 2-9: *Fibrinogen-induced change in whole blood viscosity at a constant hematocrit of 48% and shear rates of 0.19 s^{-1} (a), 0.35 s^{-1} (b) and 0.64 s^{-1} (c).*

A quantitative estimation of the rouleaux size versus the shear rate seems to be difficult task. Some analytical models predict the shear rate effect, rouleaux size, aggregation/disaggregation rates, and resultant viscosity with a high degree of accuracy [2.16]. Personally, we did not consider these issues because they are irrelevant for the course of the current project.

So far, the shear rate, hematocrit, fibrinogen concentration, and rouleaux formations have been considered as contributors to the viscosity of whole blood. The last parameter belonging to this group is temperature. Increased temperature induces lower viscosity for both plasma and whole blood. It is suggested that mechanically rouleaux are more stable at lower temperatures, hence red cell aggregates are more resistant to hydrodynamic dispersion [2.27]. This is more pronounced at low shear rates. Also, it has been found that diminished temperature causes an increase in the adsorptive energy of red-cell aggregation, which is due to a stronger molecular adsorption stress and/or weaker electrostatic repulsion [2.28, 2.29]. Additionally, red blood cell deformability is impaired when a temperature decrease is followed by a larger contact area between aggregating cells. Another factor is the plasma protein adsorption, which is a process already related previously to the formation of rouleaux. This process is exothermic and is therefore stronger at lower temperatures.

Figure 2-10 shows the observed change in whole blood viscosity versus temperature at a hematocrit of 46%, a fibrinogen concentration of 2.6 g/l, and shear rates of 0.19 s^{-1} (a), 0.35 s^{-1} (b) and 1.18 s^{-1} (c).

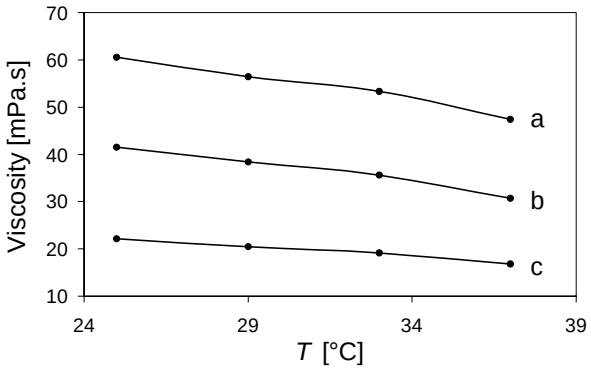

Figure 2-10: *Viscosity versus temperature measured at shear rates of 0.19 s^{-1} (a), 0.35 s^{-1} (b) and 1.18 s^{-1} (c).*

2.2.4 Flow dynamics

A few of the liquid properties concerning rheology, i.e. viscosity, shear stress and shear rate, were already presented in the previous section. This section will concentrate on the way blood flows through tubes and vessels. The complexity of the involved mechanisms requires the explanation of some basic definitions [2.9-2.11, 2.13, 2.17, 2.29, 2.30]:

- Laminar and turbulent flow [2.9]: A viscous liquid whose particles move in parallel planes or sheets (laminae), when flowing between parallel plates, is referred to as laminar flow. On the contrary, a turbulent flow has no smooth streamlines, but is chaotic with a random component of velocity superimposed on the mean flow. The streamlines do not necessarily have to be linear; they may be curved, non-uniform, etc. However, it is important that they are smooth, permanent and not changed over time. Some transition phenomena that occur when a fluid transforms from a laminar into a turbulent state, or vice versa, are correctly described as flow instabilities.

- Plastic flow system [2.29]: A system, in which flow will not take place until the applied shearing stress exceeds a certain yield level (Fig. 2-11). A blood-flow system behaves similarly to a plastic flow system.

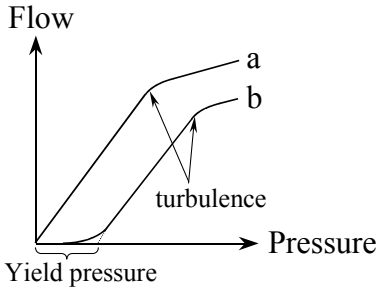

Figure 2-11: *Pressure-flow diagram of a Newtonian fluid (a) and in a plastic flow system (b).*

The importance of these definitions will be stressed during the course of the current work when an *in vitro* blood-characterization setup is designed. The shear properties of the fluid will have to be well defined and controllable in order to avoid undesired flow-related parasitic components. In laminar flow, the pressure drop and energy loss are dependent on the shear stresses. On the other hand, shear stresses are in strong correlation with the flow rate; thus achieving the desired set of shear parameters by setting the flow in the pipe system is possible only when no flow instabilities are present. The existence of flow instabilities or even turbulence may have dramatic effects on the diffusion of suspended matter, on the stress field, and on the pressure drop. Theoretically derived quantitative estimation of whether flow instabilities or turbulence exist in a certain system is given by the *Reynolds number* [2.30]:

$$\mathrm{Re} = \bar{v}\frac{D\rho}{\eta} \quad , \tag{2-8}$$

were v [m/s] is the mean velocity in the pipe, D [m] is the pipe diameter, ρ [kg/m^3] is the density of the fluid, and η [Pa.s] is the viscosity. The Reynolds number *Re* is dimensionless. Blood density ranges between 1052 kg/m^3 and 1061 kg/m^3 [2.2].

When *Re* is below 100, the flow is laminar. For *Re* between 100 and 2000, flow instabilities or even turbulences are to be expected. This depends on the entrance conditions, bends or other curvatures the pipe system may have. Almost certainly, the flow in a pipe is turbulent when *Re* is greater than 2000. In turbulent flow, the flow resistance is increased by internal effects. They are proportional to the square of the velocity and depend on the roughness of the tube wall and many other factors when a complex pipe system is used.

Blood fluidity, i.e. the reciprocal of its viscosity, in a tube or vessel partly depends upon the tendency of the erythrocytes to accumulate along the central core of the flowing stream. This effect leaves a cell-free layer of plasma in contact with the wall (Fig. 2-12). As a result, the flow becomes "lubricated" and shearing energy is conserved.

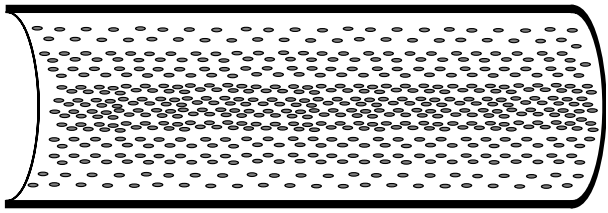

Figure 2-12: *Axial accumulation of erythrocytes.*

For a homogeneous liquid, the shear stress is zero at the tube axis and increases linearly with the distance from the axis. The highest value is reached at the wall. The same holds for the shear rate, which is zero on the axis and has its peak at the wall. A non-Newtonian liquid behaves in a slightly different manner. It shows a non-linear shear rate profile because of the yield stress. In a blood stream, for example, the shear rate remains zero for some distance from the tube axis until the shear stress reaches the yield stress (Fig. 2-5). The central core of the fluid moves at uniform velocity without being sheared. Such a flow is referred to as "plug flow" (Fig. 2-13) [2.30].

Regarding the measurement of viscosity, it is important to note that for a non-Newtonian fluid, viscosity varies across the tube or vessel cross section due to the shear rate variation. An electrical-impedance-based viscosity sensor, which covers the entire tube with its electrical field, will always reflect the average viscosity. A sensor with a shallow electrical-field distribution will only sense the local viscosity and might show distorted or even irrelevant results. For example, this can happen

when the sensor is located near a wall where the shear rate is at its highest level.

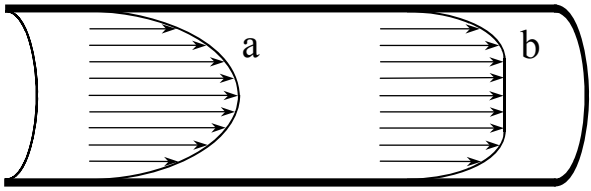

Figure 2-13: *Flow velocity profile of a Newtonian (a) and non-Newtonian (b) liquids.*

When a viscosity sensor is off the tube axis, the following considerations must be applied: the flow is the result of a pressure difference, Δp, between two points, which are at a distance L apart. For a homogeneous liquid, the shear stress at a distance r from the tube axis is calculated with:

$$\tau_r = \frac{\Delta p r}{2L} \quad . \tag{2-9}$$

The quotient $\Delta p/L$ is known as the "pressure gradient". The link between viscosity, shear stress and the shear rate is defined by Eq. 2-4, hence the shear rate at the distance r from the axis is:

$$\dot{\gamma}_r = \frac{\Delta p r}{2L\eta} \quad . \tag{2-10}$$

In principle, for a Newtonian liquid, viscosity is a direct reflection of the pressure gradient and the tube geometry:

$$\eta = \frac{R^4 \pi \Delta p}{8LQ} \quad , \tag{2-11}$$

where R is the internal radius of the tube, and Q is the volumetric flow rate. Expression 2-11 is known as the Hagen-Poiseuille equation. It can be also applied to non-Newtonian liquids where the result is called "apparent viscosity" and effectively represents the average viscosity of the sample volume covered by the sensor [2.9, 2.13, 2.30].

2.3 Blood-viscosity analysis: clinical relevance

The viscosity of blood could provide useful information for diagnostics and treatment of cardiovascular diseases. Its most important role is in microcirculation where it contributes to the peripheral resistance and can cause sludging in the postcapillary venules. Additionally, at the sites of severe atherosclerotic obstructions or at vasospastic locations, when the change in vessel diameter is limited, blood viscosity contributes to stenotic resistance, badly hampering tissue perfusion. Apart from the direct haemodynamic relevance, an increase in blood viscosity at low shear, by means of cell aggregation, is associated with high thrombotic risk. Moreover, an increased red blood cell aggregation reflects inflammation, and hyperviscosity has been established as one of the inflammatory activity markers [2.9, 2.11, 2.13, 2.31]. Online blood viscosity monitoring may become equally important in intensive-care as well. During on-pump heart surgery, for example, considerable variation in blood viscosity is observed, which requires opportune monitoring and control [2.32, 2.33]. There are many other less apparent clinical situations where elevated viscosity could be detected. A wide spread disease such as diabetes is only one of them. It is accompanied by altered blood flow and protein concentration, increased viscosity and erythrocyte aggregation. Subsequently, complications arise in the development of atherosclerosis and myocardial infarction among diabetics [2.39-2.41]. While viscosity cannot be seen as the main marker for this particular disease, it is important to stress the relevance of whole blood viscosity in the "cause-effect" chain in a broad range of clinical situations.

2.3.1 Haemodynamic implications of blood viscosity

The flow of blood in the cardiovascular system is determined by the pressure difference, vessel dimension and blood viscosity. This is clearly seen in Hagen-Poiseuille equation 2-11 if the flow, Q, is expressed. A proper tissue perfusion requires maintenance of a sufficient pressure gradient generated by the heart and/or adequately low-blood viscosity. For example, a rise in the hematocrit increases viscosity and may result in lower tissue perfusion. At the same time, high levels of aggregating proteins, e.g. fibrinogen, or other "acute-phase" proteins, can cause an additional increase in viscosity. In such cases normal tissue perfusion could be restored by lowering the hematocrit. Thus, an optimal hematocrit for tissue perfusion exists [2.34]. If optimal hematocrit cannot be

achieved, widening of the vessel lumen by applying vasodilating drugs can compensate for the high viscosity and have a great impact on the peripheral resistance, too. However, in atherosclerotic arteries, in which the dilating capacity is limited, blood viscosity remains an important factor [2.35]. Some studies list increased blood viscosity as one of the factors in hypertension and atherosclerosis that contribute to the morbidity and eventually mortality associated with tissue ischemia. In these cases, a decrease in viscosity, by means of hemodilution, for example, has been found to be much more beneficial than vasodilation [2.36, 2.37, 2.38].

2.3.2 Microcirculation

The Hagen-Poiseuille equation (2-11) foresees the haemodynamic influence of whole blood viscosity on the flow of blood through a single vessel and defines the required pressure difference when a certain flow rate has to be maintained. On the macroscale level, which concerns the entire cardiovascular system, about 90% of the total pressure drop between the aorta in the left heart and the right part of the heart occurs in the arterioles, capillaries, and venules, i.e. in the microcirculation [2.41, 2.42]. Reaching the arterioles, red blood cells aggregates disperse due to increased shear properties. Cells flow individually through the capillaries, and then aggregate back within the collecting venules. Thus, the flow resistance in the capillaries is determined by the cell's deformability. In the venules, flow resistant factors are associated with an increased aggregation tendency, due to the low shear properties and provoked by the presence of fibrinogen or other acute-phase proteins [2.43]. An increased viscosity and erythrocyte hyperaggregation may lead to the sludging of the blood in the venules and can certainly impair tissue oxygenation, limit blood supply (ischemia), etc. [2.44]. In on-pump heart surgery, for instance, extracorporeal circulation and hypothermia affect the deformability of the cells and an acute-phase reaction is induced. Consequently, diffuse cerebral microcirculatory disorders may occur. Ultimately, there is enough evidence that hemorheological factors are important in coronary and cerebral circulation, and early detection of one of them, which is viscosity, may radically improve the outcome of microcirculation-related abnormalities [2.9].

2.3.3 Inflammation and atherosclerosis

Inflammation is the first response of the immune system to infection or irritation. An acute inflammation may be caused by physical damage, chemical substances, micro-organisms or other agents. The inflammatory response consists of changes in blood flow, increased blood-vessels permeability and the escape of cells from the blood into the tissues. The affected areas are occupied by a transient material called acute inflammatory exudate. The exudate carries proteins (acute-phase proteins), fluid and cells from local blood vessels into the damaged area to mediate local defences. When an infective agent, e.g. bacteria, is present in the damaged area, it can be destroyed and eliminated by components of the exudate. The damaged tissue can be broken down and partially liquefied, and the debris removed from the site of the damage. A strong link has been found between the inflammatory indexes (C-reactive protein (CRP) and fibrinogen) and a pronounced RBC aggregation [2.45, 2.46]. The latter has already been mentioned as one of the primary factors in whole blood viscosity.

Research shows that too much inflammation can sometimes have adverse effects on the blood vessels that transport oxygen and nutrients throughout the body. Atherosclerosis, which involves the formation of fatty deposits or plaques in the inner walls of the arteries, is now considered in many ways a chronic inflammatory disorder of the blood vessels. An increased blood viscosity is a mechanism, by which all major risk factors promote atherosclerosis [2.47]. Decreased blood flow, as a consequence of a higher viscosity, prolongs the residence time of atherogenic elements such as lipoproteins and platelets in the vicinity of the endothelium. A prolonged residence time would facilitate plate adhesion to the endothelium, aggregation, and release of growth factors. The latter are the basis for an atherogenesis [2.48].

Inflammation not only affects the atherosclerotic phase of heart disease, but also the rupturing of plaque, which can then interfere with the blood, causing a heart attack [2.49]. In any way shape or form, inflammatory activity results in a higher aggregation tendency and ultimately in a higher blood and plasma viscosity.

2.3.4 Intensive care and blood viscosity

Some recent studies have focused on intensive-care monitoring, by specifically considering blood flow, temperature, viscosity, hematocrit,

etc. [2.32, 2.33, 2.50]. Blood viscosity particularly, may prove to be a valuable clinical parameter when monitored online. It will help in selecting the optimal hemodilution to counteract the negative effects of hyperviscosity. Several studies have observed reduced red blood cell deformability after on-pump surgery, which adversely affects tissue oxygenation. Hypothermia has been pointed out as one of the causes [2.51, 2.52]. Additionally, post-operative cerebral and renal dysfunctions are also believed to occur partly because of hyperviscosity. Experiments during on-pump open-chest heart surgery have shown reliable estimation of hematocrit, which is the most important determinant of viscosity, by measuring blood resistivity at low frequencies (few tens of kHz). However, those studies involved measurements at a high shear rate and were unable to reliably sense the viscosity fluctuations that are induced by the acute-phase proteins. As explained earlier in this chapter, the effect of the acute phase proteins are present mainly in low shear conditions.

The outcome of the medical treatment of patients with aneurysmal subarachnoid haemorrhage [2.35] may be dramatically improved if accurate measurement of blood viscosity is performed. The treatment in this situation involves hemodilution (Triple-H therapy) to increase blood flow, which is reduced due to severe cerebral vasospasm. [2.53]. According to the Hagen-Poiseuille law, blood flow can be increased if the perfusion pressure is increased or blood viscosity is decreased. In the case of severe vasospasm, lowering blood viscosity is the only way to increase the blood flow in the post-stenotic area. In such situations adequate monitoring of blood viscosity may give optimal results.

2.4 Conclusions

Blood rheology and particularly whole blood viscosity depends largely upon the packed cell volume, i.e. the amount of erythrocytes (red blood cells). The effect of leukocytes and thrombocytes on viscosity can be neglected, whereas a linear increase in hematocrit (red blood cell concentration) leads to an exponential rise in blood viscosity.

The viscosity of plasma is mainly determined by the concentration of high molecular weight proteins such as fibrinogen or immunoglobulins. Smaller globular molecules such as albumin for example are less significant.

Red cell aggregation is the prime factor in whole blood viscosity at a low shear rate. It is a reversible process caused by large proteins, e.g.

fibrinogen and immunoglobulins, which form bridges between the cells. In large vessels, aggregates provoke the migration of cells to the vessel axis and create plug flow. Such a flow profile improves blood fluidity and oxygen transport. However, in low-flow situations, aggregation induces blood viscidation, which impairs tissue perfusion.

Red blood cell deformability plays an important role in blood rheology, too. It is defined by the mechanical properties of the cell membrane and the cell-content viscosity. In microcirculation, red cell deformability and plasma viscosity are the main determinants of resistance to flow.

When blood flows through a vessel, it splits into layers with different velocities, due to the high cellular content. The quantitative measure of this effect is called the shear rate. The frictional force between two adjacent layers is directly proportional to the shear rate and to the internal frictional property of the fluid, i.e. its viscosity. This interaction defines the non-Newtonian characteristics of blood, the viscosity of which is not constant but changes with the shear rate.

In the pathophysiology of vascular diseases, blood viscosity is a major factor, having implications in cardiovascular hemodynamics and tissue perfusion. An elevated blood viscosity also increases the thromboembolic risk and can be correlated with systemic inflammatory activity.

2.5 References

2.1 D. Van Wynsberghe, C. N. Nobak, R. Carola, “Human anatomy & physiology”, Third edition, McGraw Hill, 1995, ISBN: 0-07-011171-5

2.2 B. D. Ratner, A. S. Hoffman, F. J. Schoen, J. E. Lemons, “Biomaterial science – An introduction to materials in medicine, 2nd Edition”, ELSEVIES ACADEMIC PRESS, 2004, ISBN: 0-12-582463-7

2.3 L. A. Geddes, L. E. Baker, “Principles of applied biomedical instrumentation”, John Wiley & Sons, 1989, ISBN: 0-471-60899-8

2.4 J. D. Bronzino, “The biomedical engineering handbook”, CRC Press, 1995, ISBN: 0-8493-8346-3

2.5 L. C. Stoner, F. M. Kregenow, “A single-cell technique for the measurement of membrane potential, membrane conductance, and the efflux of rapidly penetrating solutes in amphiuma erythrocytes”, J. Gen. Physiol., The Rockefeller University Press, October 1980, Volume 76, pp. 455-478

2.6 N. Maeda, M. Seike, S. Kume, T. Takaku, T. Shiga, “Fibrinogen-induced erythrocyte aggregation: erythrocyte-binding site in the fibrinogen molecule”, Biochimica et Biophysica, ELSEVIER, 1987, pp. 81-91

2.7 W. T. Hung, A. F. Collings, J. Low, “Erythrocyte sedimentation rate studies in whole human blood”, Phys. Med. Biol., 1994, pp. 1855-1873

2.8 J. P. A. Weaver, A. Evans, D. N. “The effect of increased fibrinogen content on the viscosity of blood”, Clin. Sci., 1969, pp. 1-10

2.9 S. Chien, J. Dormandy, E. Ernst, A. Matrai, “Clinical hemorheology”, Martinus Nijhoff Publishers, Dordrecht, 1987, ISBN: 0-89838-807-4

2.10 G. B. Thurston, “Viscoelasticity of human blood”, Biophysical Journal, 1972, Volume 12, pp.1205-1217

2.11 G. A. M. Pop, D. J. Duncker, M. Gardien, P. Vranckx, S. Versluis, D. Hasan, C. J. Slager, “The clinical significance of whole blood viscosity in (cardio)vascular medicine”, Netherlands Heart Journal, Volume 10, December 2002, pp. 512-516

2.12 C. Gorman, A. Park, “The secret killer”, TIME, 24 February, 2004

2.13 W. W. Nichols, M. F. O'Rourke, “McDonald's Blood Flow in Arteries, Theoretical: Experimental and Clinical Principles”, Fifth edition, London, Hodder Arnold, 2005, ISBN: 0-340-80941-8

2.14 W. Koenig, M. Sund, B. Filipiak, A. Doring, H. Lowel, E. Ernst, “Plasma Viscosity and the Risk of Coronary Heart Disease”, Arterioscler Thromb Vasc Biol. 1998; Vol. 18, pp. 768-772

2.15 W. H. Reinhart, “Molecular biology and self-regulatory mechanisms of blood viscosity: A review”, Biorheology, 38, 2001, pp. 203–212

2.16 J. Chen, Z. Huang, “Analytical model for effects of shear rate on rouleau size and blood viscosity”, Biophysical Chemistry, 1996, Vol. 58, pp. 273-279

2.17 C. Picart, J. M. Piau, H. Galliard, P. Carpentier, “Blood low shear rate rheometry: influence of fibrinogen level and hematocrit on slip and migrational effects”, Biorheology, 1998, Vol. 35, pp. 335-353

2.18 C. J. Jen, L. V. McIntire, “Characteristics of shear-induced aggregation in whole blood”, J Lab Clin Med., January 1984, Vol. 103, pp. 115-24

2.19 R. E. Wells, E. W. Merrill, “The variability of blood viscosity”, The American Journal of Medicine, Occtober 1961, Vol. 31, pp. 505-509

2.20 S. Chien, S. Usami, H. M. Taylor, J. L. Lundberg, M. I. Gregersen, “Effects of hematocrit and plasma proteins on human blood rheology at low shear rates”, J Appl Physiol, 1966, Vol 21, pp. 81-87

2.21 M. W. Rampling, H. J. Meiselman, B. Neu, O. K. Baskurt, “Influence of cell-specific factors on red blood cell aggregation”, Biorheology, 2004, Vol. 41, pp. 91-112

2.22 Z. Marton, G. Kesmarky, J. Vekasi, A. Cser, R. Russai, B. Horvath, K. Toth, “Red blood cell aggregation measurements in whole blood and in fibrinogen solutions by different methods”, Clinical Hemorheology and Microcirculation, 2001, Vol. 24, pp. 75-83

2.23 Y. Izumida, A. Seiyama, N. Maeda, “Erythrocyte aggregation: bridging by macromolecules and electrostatic repulsion by sialic acid”, Biochimica et Biophysica Acta. 1991, Vol. 1067, pp. 221-226

2.24 D. R. Gilligan, A. C. Ernstene, “The relationship between the erythrocyte sedimentation rate and the fibrinogen content of plasma”, Am I. Med Sci, 1934, Vol. 187, pp. 552-556

2.25 T. L. Fabry, “Mechanism of erythrocyte aggregation and sedimentation”, Blood, November 1987, Vol. 70, pp. 1572-1576

2.26 L. Gustafsson, L. Appelgren, H. E. Myrvold, “Effects of increased plasma viscosity and red blood cell aggregation on blood viscosity in vivo”, Am J Physiol Heart Circ Physiol, 1981, pp. H513-H518

2.27 F. J. Neumann, H. Schmid-Schonbein, H. Malotta, “Effect of temperature dependent changes in mechanical stability of red blood cell aggregates on relative apparent whole blood viscosity”, Biorheology, 1987, Vol. 24, pp. 463-472

2.28 F. J. Neumann, H. Schmid-Schonbein, H. Ohlenbusch, “Temperature-dependence of red cell aggregation”, Pflugers Arch., May 1987, Vol. 408, pp. 524-530

2.29 B. Eiseman, F. C. Spencer, “Effect of hypothermia on the flow characteristics of blood”, Surgery, September 1962,Vol. 52, pp. 532-544

2.30 F. M. White, “Viscous fluid flow, Third edition”, McGraw-Hill International Edition, ISBN: 0390547743

2.31 G. A. M. Pop, W. J. Hop, L. Moraru, M. van der Jagt, J. Quak, D. Dekkers, Z. Chang, F. J. Gijsen, D. J. Duncker, C. J. Slager, “Blood electrical impedance closely matches whole blood viscosity as parameter of hemorheology and inflammation”, Applied Rheology, 2003, Vol. 12, pp. 305-312

2.32 G. A. M. Pop, Z. Chang, C. J. Slager, B. J. Kooij, E. D. van Deel, L. Moraru, J. Quak, G. C. M. Meijer, D. J. Duncker, “Catheter-based impedance measurements in the right atrium for continuously monitoring hematocrit and estimating blood viscosity changes; an in vivo feasibility study in swine”, Biosensors and Bioelectronics, 2004, Vol. 19, pp. 1685-169

2.33 G. A. M. Pop, T. L. M. de Backer, M. de Jong, P. C. Struijk, L. Moraru, Z. Chang, H. G. Goovaerts, C. J. Slager, A. J. J. C. Bogers, “On-line electrical impedance measurement for monitoring blood viscosity during on-pump heart surgery”, European Surgical Research, 2004, Vol. 36, pp. 259-265

2.34 J. W. Crowll, E. E. Smith, “Determinant of the optimal hematocrit”, J Appl Physiol., 1967, Vol. 22, pp. 924-930

2.35 F. H. Vermeij, D. Hasa, H. W. C. Bijvoet, C. J. J. Avezaat, “Impact of medical treatment on the outcome of patients after aneurysmal subarachnoid hemorrhage”, Stroke, 1998, Vol. 29, pp. 924-930

2.36 O. K. Baskurt, “Pathophysiological significance of blood rheology”, Turk J Med Sci, 2003, Vol. 33, pp. 347-355

2.37 Y. Cinar, G. Demir, M. Pac, A. B. Cinar, “Effect of hematocrit on blood pressure via hyperviscosity”, American Journal of Hypertension, 1999, Vol. 12, pp. 739-743

2.38 M. Woodward, A. Rumley, H. Tunstall-Pedoe, G. D. O. Lowe, "Does sticky blood predict a sticky end? Associations of blood viscosity, haematocrit and fibrinogen with mortality and the West of Scotland", British Journal of Haematology, 2003, Vol. 122, pp. 645-650

2.39 A. Hoieggen, E. Fossum, A. Moan, E. Enger, S. E. Kjeldsen, "Whole-blood viscosity and the insulin-resistance syndrome", Journal of Hypertension, 1998, Vol. 16, No. 2, pp. 203-210

2.40 R. E. Yodaiken, "The relationship between diabetic capillaropathy and myocardial infarction: a hypothesis", Diabetes, 1976, Vol. 25, pp. 928-30

2.41 E. W. Merrill, E. R. Gilliland, G. Cokelet, H. Shin, A. Britten, R. E. Wells, "Rheology of blood and flow in the microcirculation ", J Appl Physiol, 1963, Vol. 18, pp. 255-260

2.42 H. H. Lipowsky, J. C. Firrell, "Microvascular hemodynamics during systemic hemodilution and hemoconcentration", AJP - Heart and Circulatory Physiology, 1986, Vol. 250, Issue 6, pp. H908-H922

2.43 W. Koenig, E. Ernst, "The possible role of hemorheology in atherothrombogenesis", Atherosclerosis, 1992, Vol. 94, pp. 93-107

2.44 E. Vicaout, X. Hou, L. Decuypere, A. Taccoen, M. Duvelleroy, "Red blood cell aggregation and microcirculation in rat cremaster muscle", Int J Microcirc, 1994, Vol. 14, pp. 14-21

2.45 R. Ben Ami, G. Barshtein, D. Zeltser, Y. Goldberg, I. Shapira, A. Roth, G. Keren, H. Miller, V. Prochorov, A. Eldor, S. Berliner and S. Yedgar, "Parameters of red blood cell aggregation as correlates of the inflammatory state", AJP - Heart, 2001, Vol. 280, pp. 1982-1988

2.46 H. Schmid-Schonbein, H. Malotta, F. Striesow, "Erythrocyte aggregation: causes, consequences and methods of assessment", Tijdschr. NVKC, 1990, vol. 15, pp. 88-97

2.47 G. D. Sloop, "A unifying theory of atherogenesis", Medical Hypotheses, 1999, Vol. 47, pp. 321-325

2.48 R. Ross, "The pathogenesis of atherosclerosis: an update" New Engl Med, 1986, pp. 488-500

2.49 A. Hoffmeister, J. Hetzel,S. Sander, M. Kron, V. Hombach, W. Koenig, “Plasma viscosity and fibrinogen in relation to haemodynamic findings in chronic congestive heart failure”, European Journal of Heart Failure, 1999, Vol. 1, pp. 293-295

2.50 D. Tanase, B. P. Iliev, J. F. L. Goosen, Z. Chang, G. A. M. Pop, J. M. M. Verwiel, C. J. Slager, P. J. Trimp, L. Pakula, G. C. M. Meijer, P. J. French, “Investigation of multi-sensor techniques for cardiac-output measurements in intensive care”, Proceedings of IEEE-EMBS, Hawaii, May 2005

2.51 S. Chien, S. Usami, R. J. Dellenback, M. I. Gregersen, “Shear-dependent deformation of erythrocytes in rheology of human blood”, Am J Physiol, 1970, Vol. 219, pp. 136-142

2.52 S. Simchon, K. Jan, S. Chien, “Influence of reduced red cell deformability on regional blood flow”, Am J Physiol, 1987, Vol 253, pp. H898-H903

2.53 J. Sen, A. Belli, H. Albon, L. Morgan, A. Petzold, N. Kitchen, “Triple-H therapy in the management of aneurysmal subarachnoid haemorrhage”, The Lancet Neurology, 2003, Vol. 2, pp. 614-620

3 *Electrical aspects of blood analysis*

3.1 Electrical properties of body tissues

Electrical impedance measurements have been used to examine the bulk electrical properties of tissues since the eighteenth century [3.1]. These properties determine the electrical-current pathways through the body, which is of fundamental importance in studies of biological phenomena and the measurements of physiological parameters. In general, the investigations can be divided into two major categories:

- Studies conducted to investigate fundamental electrical properties and correlate these with tissue properties.
- Studies aimed at correlating the initially characterized tissue properties with physiological events, e.g. body fluid shift, respiration, blood flow, cardiac output, ventricular emptying, stroke volume, thoracic impedance, etc.

Due to the complexity of the human body, studies employing impedance spectroscopy require multi-frequency impedance measurement techniques that acquire both the real and the imaginary impedance components [3.2, 3.3]. The measured impedance is then graphically and numerically reconstructed to fit the complex arrangement models for different physiological events. The fundamental principles in this field

were established approximately one century ago. Below is a list of the early pioneers and their milestone achievements.

Rudolf Hoeber (1910s):

The first to recognize the frequency dependence of blood conductivity. He discovered the existence of the cell membranes and determined the interior conductivity of erythrocytes, which led to the discovery of β-dispersion.

Hugo Fricke, Kenneth (Kacy) Cole (1930s):

Explanation of the β-dispersion, which is also known as the Maxwell-Wagner effect. First nonlinear cell membrane studies and first electrical-impedance model of blood.

Herman Schwan (1950s):

Introduction to the principles of α-β-γ dispersions for the electric response of tissues and cell suspensions. An early dielectric spectroscopy of cells, vesicles, organelles, membranes, bacteria, proteins, DNA, etc.

3.1.1 Conduction and polarization

When an impedance measurement sensor is in contact with a tissue or an aqueous solution and an excitation signal is applied, conduction and polarization mechanisms occur. Some of the mechanisms reflect the electrical properties of the matter while others are the result of the electrode-tissue interaction. The later resembles parasitic components and must be thoroughly identified and cancelled in the final data analysis [3.4, 3.5].

The body tissues and fluids demonstrate a wide variety of electrical properties. As far as conduction is concerned, it occurs by means of electron, hole or ion transport. In most biological materials, ions are the predominant charge carriers and the resultant conductivity depends mainly on the ion concentration. Blood plasma, for instance, resembles a simple aqueous-ion solution, the conductivity of which is defined notably by the chloride, sodium and potassium ions. However, more complex structures, such as tissue or even blood, involve cell structures, which by themselves contain ionic conducting fluids but which are also bound by a poorly conducting membrane. The membrane consists of a lipid bilayer and is coated on either surface by protein molecules. Pores through the membrane ensure controlled transfer of selected molecules and ions. A bio-membrane has a high dielectric constant and, therefore, electrically it resembles a capacitance in parallel with a conductance due to the pores

[3.6]. Blood behaves similarly to a complex biological tissue; thus its electrical properties involve identical conduction and polarization mechanisms.

Electric polarization is associated with charge storage and reflects the electric field disturbance of the charge distribution. The electrical field displaces opposite charges and a dipole moment is created. The dipole moment is proportional to the charges and the distance between them. Inside a biomaterial system, the existence of a charge storage may be due to one or more mechanisms of polarization that can be categorized into the following classifications: electronic, ionic, dipole, interfacial, space charge, and Faradic or Warburg polarization. The first three exist in uniform bulk materials, while the others occur only in materials with discontinuities or a heterogeneous microstructure [3.7]. Figure 3-1 shows the main groups of relaxation processes that take place in biological systems.

Electronic polarization is observed when the center of a negative charge of electron clouds, surrounding the nucleus of an atom, is displaced with respect to the positive charge center of the nucleus. This polarization exists in all materials. However, its dipole moment is small and responds to variation in the electric field at frequencies approaching the ultraviolet region of the spectrum. At lower frequencies it leads to a constant level of polarization and almost no temperature dependence.

Ionic polarization can be seen in crystals with distinctly identifiable ions in the lattice. Each pair of oppositely charged neighbouring ions has a dipole moment. This mechanism is of little significance in biological materials. Nevertheless, its relaxation frequency coincides with some polarization effects unique for biological materials and therefore is depicted in Fig. 3-1.

Orientational polarization occurs when dipoles are free and orient themselves in an electrical field. A dipole is a molecule which has opposite charges separated from one another. The magnitude of the polarization depends on the dipole's nature and its concentration. As orientation occurs, charge is transported and transient conduction occurs. No further conduction takes place until the electric field is reversed. At high frequencies, dipoles are not able to follow changes in the field and no polarization or conduction is observed. There is, nonetheless, an intermediate frequency at which the dipoles are just oriented before the field is again reversed. The time required for orientation at this frequency is referred to as the relaxation time, τ_d, and the frequency is referred to as

the relaxation frequency, f_r. At the relaxation frequency, the conduction current is at its maximum and the polarization is in between the low-frequency and high-frequency values. The relaxation time associated with this polarization process depends on the dipole's size and the nature of the media, and is highly temperature-dependent.

Interfacial polarization can exist in materials that demonstrate a heterogeneous structure, for example, in materials where regions of high conductivity are in a matrix of low-conductivity material. This structure often represents biological materials with conductive cell interiors which are separated by relatively insulating membranes. In the case of highly resistive interfacial layers, where no transport of charge-conveying species is allowed, an accumulation of charge results in space-charge polarization. In biological materials, space-charge polarization is governed by ion transport and accumulation.

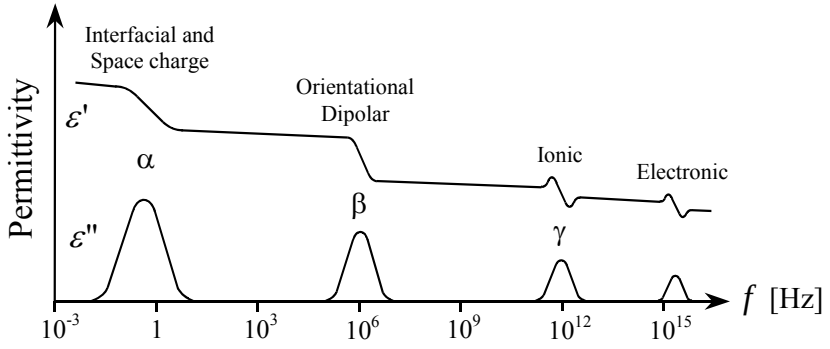

Figure 3-1: *The frequency dependence of the real and imaginary parts of the complex permittivity in the presence of various polarization mechanisms.*

Faradic or Warburg polarization, which is not depicted in Fig. 3-1 but would be situated to the left of the interfacial polarization, can occur if an accumulation of space charge at an interfacial boundary leads to a sufficient chemical potential to drive a reaction of the type $n_1 M^+ + n_2 e \leftrightarrow n_3 M$. Upon removal of the electrical field, the accumulated space charge decreases and the chemical reaction reverses.

In practice, space charge polarization cannot take place without the existence of interfacial polarization. Additionally, Faradic polarization cannot occur without the existence of space charge polarization. All three phenomena are highly dependent on the charge transport and reflect the

temperature dependence of the dominant conduction process in the material being investigated.

In the presence of various polarization mechanisms, the total polarization is the sum of all the contributions. It is also evident that the polarization mechanisms eventually disappears one by one when the frequency of the applied excitation signal increases.

In general, the charge storage capabilities of a medium is expressed by its complex permittivity:

$$\varepsilon^* = \varepsilon' - \mathrm{i}\varepsilon'' \quad . \tag{3-1}$$

The real part ε' reflects the accumulation of charge and equals the linear permittivity of the medium ε. The imaginary part ε'' is associated with the losses in the medium and equals $\sigma/\omega\varepsilon_0$, where ω is the angular frequency, and ε_0 is the permittivity of free space [3.8].

The losses in the medium can be expressed as:

$$\sigma^* = \sigma' + \mathrm{i}\sigma'' \quad , \tag{3-2}$$

where the real part σ' equals the electrical conductivity of the medium σ, while $\sigma'' = \omega\varepsilon\varepsilon_0$.

Both ε^* and σ^* are frequency-dependent and are related as follows [3.9]:

$$\sigma^* = \mathrm{i}\omega\varepsilon_0\varepsilon^* \quad . \tag{3-3}$$

In terms of an equivalent electrical diagram, the permittivity is presented by a capacitor and the conductivity by a conductor, respectively.

Since the early pioneering work on the characterization of biological materials, the formulation of all the afore-mentioned polarization mechanisms have changed slightly. The corresponding frequency dependence of permittivity is referred to as dielectric dispersion. More specifically, a dispersion is the transition from one polarization level to another. All the polarization phenomena observed in biological materials are divided in three major dispersion regions: at low frequencies, at radio frequencies, and at microwave frequencies. These regions are named α, β and γ, and in Fig. 3-1 they coincide with the interfacial, orientational and ionic polarization, respectively.

The α dispersion is generally associated with the interfacial (Maxwell-Wagner) polarization and is a result of the electrical double

layers and the surface ionic conduction effects that take place at the membrane boundaries. A large-magnitude, low-frequency α-dispersion has been observed in muscle tissue and is related partly to the tubular system. Colloidal particle suspensions also demonstrate behaviour, which is caused by the counterion atmosphere surrounding the charged surface.

At frequencies lower than several hundred kHz, the electric current passes through the extracellular space, where electrolytic conduction becomes dominant for the bulk conductivity. Thus, the tissue bulk conductivity is a function of the volume fraction of the cellular phase and the specific conductivity of the extracellular medium. In blood this can be associated with the blood cells volume fraction and the specific conductivity of plasma, respectively. At frequencies below the α dispersion, the relative permittivity reaches high levels mainly due to interfacial phenomena.

The radio frequency β dispersion was first investigated and recognized as a relaxation process caused by the cell membranes. In principle, it consists of two components, which originate from at least two sources: the capacitive shorting-out of membrane resistances, and the rotational relaxations of biomacromolecules. In blood it is due to the charging of the cell membranes through the intracellular and extracellular media. Above the β dispersion, the cell membranes have negligible impedance, and the current passes through both, the extracellular and the intracellular media without being affected by the membrane capacitance.

The γ dispersion is the last one to be found in biological materials and arises from the relaxation of abundant bulk water in the tissues [3.10].

As far as whole blood is concerned, it is important to note that α and β dispersions are mainly associated with the cell membrane, e.g. the cellular phase of whole blood, and not with the water and electrolyte content. As a result, the relative permittivity of whole blood drops markedly in the frequency range above 1 MHz.

3.1.2 Maxwell-Wagner effect

The Maxwell-Wagner effect was described above as a relaxation process occurring in all systems in which the electric current passes an interface between two different dielectrics. Figure 3-2 illustrates the effect by means of a plate capacitor with two different homogenous materials inserted between a pair of sensing electrodes.

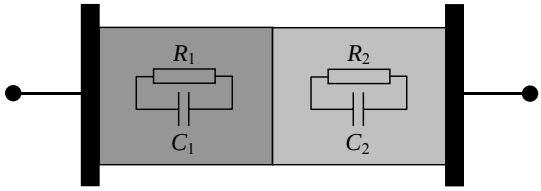

Figure 3-2: *Equivalent circuit of the Maxwell-Wagner effect in a simple dielectric model.*

The resultant capacitance between the electrodes is

$$C = (C_1 R_1^2 + C_2 R_2^2) / (R_1 + R_2)^2 \quad f \to 0$$

$$C = (C_1 C_2) / (C_1 + C_2) \quad f \to \infty .$$

The capacitance values converge both at low and at high frequencies as the low-frequency capacitance becomes higher than the high-frequency one. Thus, with the parallel model of two material slabs in series, a dispersion similar to Debye occurs even without any dipole relaxation being presented in the dielectric. Apparently, the dispersion is due to the conductance in parallel with the capacitance in each dielectric, so that the interface can be charged. In tissues and blood, this effect is observed on the boundaries between the cell membranes and the surrounding fluid. Maxwell derived an analytical solution for the conductivity, σ, of a dilute suspensions of spherical particles [3.11]:

$$\frac{\sigma - \sigma_2}{\sigma + 2\sigma_2} = \frac{p(\sigma_1 - \sigma_2)}{\sigma_1 + 2\sigma_2} \quad , \tag{3-4}$$

where p is the volume fraction of the spheres. The medium has a conductivity σ_2, and the intracellular particle conductivity is σ_1. The dielectric properties of a heterogeneous system are expressed in a similar fashion. For spherical, non-conducting particles with permittivity ε_1 that are dispersed in an insulating medium with the permittivity ε_2, it holds:

$$\varepsilon = \varepsilon_2 \left(1 + 3p \frac{\varepsilon_1 - \varepsilon_2}{2\varepsilon_2 + \varepsilon_1} \right) \quad . \tag{3-5}$$

However, Eq. 3-5 does not apply in the case depicted in Fig. 3-2 since it describes a heterogeneous system under the assumption that the conduction currents do not violate the local electroneutrality condition in the volume of the conducting components, e.g. if an ideal dielectric is considered. Extended theoretical considerations regarding real dielectrics, where ionic conduction exists, can be found in [3.12].

The dispersion system theory developed by Maxwell (Eqs. 3-4 and 3-5) is extended by Wagner for oblate or prolate spheroids. However, we will focus on Fricke's work, which specifically concerns the electric conductivity and capacity of whole blood.

3.2 Electrode-electrolyte interface

Regardless of the bioimpedance method used, the measurement instrument must be coupled to the tissue or body fluid being investigated by means of electrodes. Complex electrochemical reactions occur at the electrode-electrolyte interface and may result in significant measurement errors. The electrolyte can be a paste, a deliberately introduced electrolyte solution, or a tissue fluid in which electrodes are inserted directly. In all cases, there is a tendency for metal ions to migrate into the solution and for ions in the electrolyte to combine with the metal. This results in charge distribution in the vicinity of the electrode, and an electrical potential is manifested. When a current is passed, additional electrochemical reactions alter the charge distribution. Then, a phenomenon called polarization impedance arises [3.13, 3.14].

The potential brought by the polarization impedance is dependent upon the metal-electrolyte combination, current density, and frequency. For measuring bioimpedances, both direct current (DC) and alternating current (AC) can be applied. This should be considered when selecting the type of electrodes. Often electrodes that have excellent DC characteristics (i.e. they are non-polarizable) have poor AC performance and vice versa. For example, platinum and gold electrodes are well suited for AC measurements, but poor in DC conditions. In general, it is very difficult to find electrodes that simultaneously combine good DC characteristics and a low AC polarization impedance.

3.2.1 Polarization impedance

Two types of processes can occur at the electrode-electrolyte interface. The first type comprises of reactions in which charged particles cannot pass across the interface barrier. These interfaces are called non-faradic. The electrodes involved in a non-faradic interface are called ideal polarized electrodes, and they electrically resemble an ideal capacitor. Though the interface is inert, processes such as absorption and desorption within the electrolyte may still occur as a result of a varying potential or solution composition. The second type of electrode system, where charge transfer does occur, is called faradic. Under specific circumstances, any electrode-electrolyte interface will exhibit a range of potentials which enable charge particles to pass across the interface. Typically, this imposes oxidation or reduction, and indicates that the charge species in dissimilar phases, e.g. electrons in the conductor and ions in the electrolyte, interact and pass on the net charge to one another [3.15].

For both faradic and non-faradic electrodes, finding the equivalent electrical circuit model requires a good understanding of the ionic fluxes as well as their concentration profile. For systems in a nonequilibrium state such as faradic electrodes, spatial fluxes are nonzero for at least one ionic species, while with the ideal polarized electrode no net current exists.

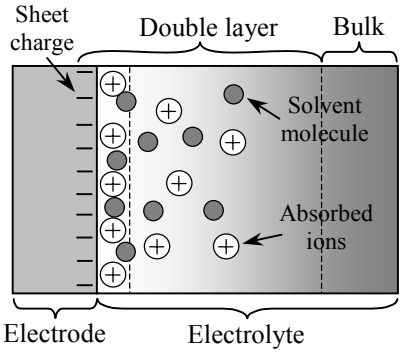

Figure 3-3: *Basic molecular-level structure of a non-faradic electrode and the corresponding double layer formation.*

The basic molecular-level structure of a faradic electrode is depicted in Fig. 3-3. No charge transfer occurs across the interface, but indeed charge can couple to the neighbouring phase, resulting in a capacitor-like

interface called a double layer. For a given spatial potential, a sheet charge exists on the metal electrode and a distributed charge exists in the solution. The latter is made up of an excess of either cations or anions in the proximity of the electrode surface. In general, the spatial potential in a system having only one cationic species and one anionic (symmetrical electrolyte), both with a charge magnitude z and total potential difference of Φ_0 on the interface, is expressed by:

$$\Phi(x) = \frac{4kT}{zq} \coth\left(\exp(-\kappa x) \tanh\left(\frac{zq}{4kT} \Phi_0 \right) \right) , \qquad (3\text{-}6)$$

where q is the charge of an electron, k is the Boltzmann constant, T is the absolute temperature, Φ_0 is the total potential difference on the interface, and κ is the Debye length, which is defined as:

$$\kappa = \left(\frac{2z^2 q^2 n^0}{\varepsilon_r \varepsilon_0 kT} \right)^{1/2} . \qquad (3\text{-}7)$$

The bulk concentration is denoted by n^0. The interfacial differential capacitance of the double layer then is found to be:

$$C_d = A \frac{\partial \sigma^M}{\partial \Phi_0} = A \left(\frac{2z^2 q^2 \varepsilon_r \varepsilon_0 n^0}{kT} \right)^{1/2} \cosh\left(\frac{zq\Phi_0}{2kT} \right) , \qquad (3\text{-}8)$$

where σ^M is the surface charge concentration on the electrode and A is its surface.

The double layer consists of two parts: an inner region, which includes ions bound relatively strongly to the surface, and an outer, or diffuse region, in which the ion distribution is determined by a balance of electrostatic forces and random thermal motion. The potential in this region decays as the distance from the surface increases until, at a sufficient distance, it reaches the bulk solution value. When subjected to an electric field, each particle and its most closely associated ions move through the solution as a unit. The potential at the boundary between this unit and the surrounding medium is known as the zeta potential ζ. In Fig. 3-3 this is associated with the layer of ions closest to the electrode. The dotted line, wrapped around this ion layer indicates surface at a

distance x_1, where the zeta potential is measured. When the two sub-layers in the electrolyte are considered separately, the double layer capacitance can be rewritten as:

$$\frac{1}{C_d} = \frac{x_1}{A\varepsilon_r\varepsilon_0} + \frac{1}{A\left(\frac{2z^2q^2\varepsilon_r\varepsilon_0 n^0}{kT}\right)^{1/2}\cosh\left(\frac{zq\zeta}{2kT}\right)} \quad . \tag{3-9}$$

Thus, C_d comprises of two components in series: C_H and C_D (see Fig. 3-4). The charges held in the inner layer form C_H, which is independent on the potential. C_D is the capacitance of the diffused charge. For the double layer capacitance C_d, it holds that:

$$\frac{1}{C_d} = \frac{1}{C_H} + \frac{1}{C_D} \quad . \tag{3-10}$$

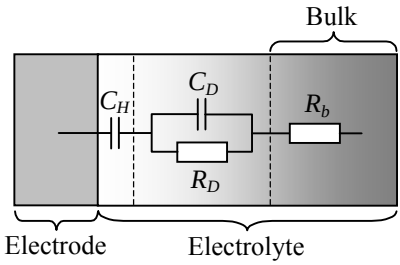

Figure 3-4: *Equivalent electrical model of a non-faradic electrode-electrolyte interface.*

In faradic electrodes, oxidizing and reducing species can transfer charge between the electrolyte and the electrode. When the solution is well mixed, the concentration in the bulk region is constant with respect to distance. Then, there is a region where the concentration drops, falling to zero at the electrode surface. This region is known as the Nernst diffusion layer.

The exact thickness, δ (see Fig. 3-5), of the Nernst diffusion layer depends upon the nature of the solution into which it extends. For a typical, well-stirred aqueous solutions it ranges between 1 μm and 10 μm. When a material reaches the surface of the electrode it is instantaneously oxidised or reduced, thereby maintaining a zero concentration at the

electrode surface. In addition, when the bulk solution reaches a high electrical conductivity, there is the possibility for the electric field, either generated by an external source or an intrinsic potential difference between the electrode and electrolyte, to exist solely within the diffusion layer.

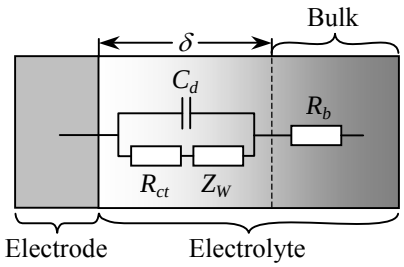

Figure 3-5: *Equivalent electrical model of a faradic electrode-electrolyte interface.*

The ion-concentration profile from the bulk to the electrode decays into a pseudo-exponential form. For simplicity, a linear concentration profile is considered instead, resulting in a quadratic electric-field function through the layer. The interfacial differential capacitance of the diffusion layer, C_d, then becomes:

$$C_d = A\frac{3\varepsilon\varepsilon_0}{\delta} \quad . \tag{3-11}$$

A complete electrical model of a faradic electrode includes an additional element that represents the faradic process. It is called the faradic impedance and comprises of a pure charge transfer resistance, R_{ct}, and a Warburg impedance, Z_W (Fig. 3-5). A typical Warburg element is modelled as both a resistive and a capacitive element in series. The capacitive element in most cases varies inversely with the square root of the frequency, $C = Kf^{-2}$, where K is a constant depending on the metal species, electrolyte concentration, and temperature.

Geddes et al. [3.14] have investigated the dependence of the series resistance and capacitance found in the polarization impedance, on the current density. For stainless steel electrodes in contact with saline solution, for example, it has been found that for a given frequency, the equivalent resistance decreases and the capacitance increases when current density is increased. The largest change has been observed at low

frequency. Similar results have been reported by Schwan for platinum electrodes [3.13]. These two materials are solely used in the current project.

Apparently, the electrode-electrolyte interface has a complex electric model, the impedance of which depends on many factors. When coupling a bioimpedance to interface electronics via electrodes, one should consider the nature of the electrode polarization impedance. The current through the sensing electrodes must be as small as possible so that minimal voltage noise is introduced by the electrode impedance. However, this is not always possible, therefore the electrode polarization must be considered in the total impedance model being studied. The Warburg model shown in Fig. 3-5 is not practical since it predicts infinite impedance for a direct current.

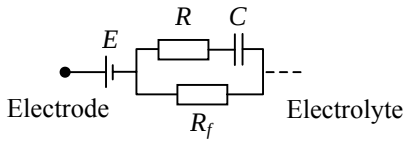

Figure 3-6: *An improved electrode-electrolyte electrical model.*

An improved electrode-electrolyte electrical model that also includes the half-cell potential, E, is shown in Fig. 3-6. In order to account for the low-frequency behaviour, a faradic leakage resistance R_f is added. This resistance behaves similarly to the Warburg element, i.e. the lower the frequency, the higher the R_f and vice versa.

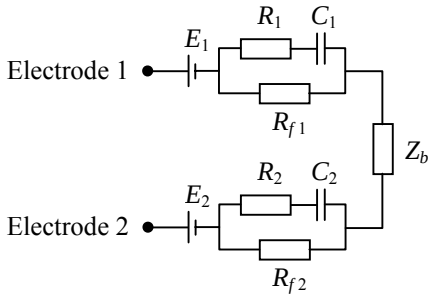

Figure 3-7: *An equivalent electrical diagram of a bioimpedance measurement cell.*

Let us consider a complete measurement setup which consists of a pair of electrodes and a bioimpedance, Z_b, in between. The total impedance then comprises of a Z_b and two electrode-polarization impedances connected in series (Fig. 3-7). The net impedance is strongly affected by the electrode polarization. This polarization effect is pronounced at low frequencies. It disappears at high frequencies, where the impedance between the pair of electrodes approximates Z_b (Fig. 3-8).

Though the electrode-electrolyte interfaces are well defined, i.e. non-faradic or perfectly polarized and faradic or nonpolarizable electrodes, it is difficult to account for the polarization impedance in a final post-processing mathematical algorithm.

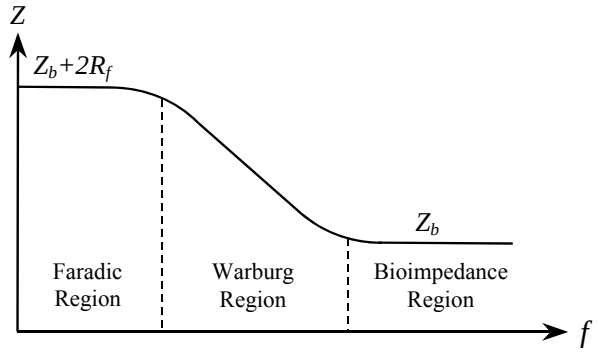

Figure 3-8: *Typical impedance-frequency characteristic of a bioimpedance measured by a two-electrode setup.*

3.2.2 Half-cell potential

An electrode-electrolyte contact is always accompanied by one of the following reactions: the electrode discharges some metallic ions into the electrolytic solution, increasing the number of free electrons in the electrode and the number of cations in the solution; or ions in the solution combine with the electrode, decreasing the number of free electrons in the electrode and the number of cations in the solution. As a result, a charge gradient builds up between the electrode and electrolyte and a potential difference arises. This is known as the half-cell potential. This potential

depends on the concentrations of the substances and the temperature, and can be calculated using the Nernst equation [3.16]:

$$E = E^0 - \left(\frac{RT}{nF}\right)\ln\left(\frac{a_{red}}{a_{ox}}\right) \quad , \tag{3-12}$$

where E^0 is the electrode potential, R is the universal gas constant, T is the absolute temperature, n is the charge number of the electrode reaction (the number of moles of electrons involved in the reaction), and F is the Faraday constant. The notation a_{red} represents the chemical activities of all of the species which appear on the reduced side of the electrode reaction. The notation a_{ox} represents the chemical activities of all of the species which appear on the oxidized side of the electrode reaction.

Table 3-1. *Electrode potentials for commonly used materials.*

Metal reaction	Electrode potential E^0 [V] at 25°C
$Al = Al^{3+} + 3e^-$	-1.662
$Zn = Zn^{2+} + 2e^-$	-0.7628
$Cr = Cr^{3+} + 3e^-$	-0.744
$Fe = Fe^{2+} + 2e^-$	-0.4402
$Ni = Ni^{2+} + 2e^-$	-0.25
$Pt(H_2)H^+$	0
$Ag + Cl^- = AgCl^+ + e^-$	+0.2225
$Cu = Cu^{2+} + 2e^-$	+0.337
$Cu = Cu^+ + e^-$	+0.521
$Ag = Ag^+ + e^-$	+0.7991
$Pt = Pt^{2+} + 2e^-$	+1.2
$Au = Au^{3+} + 3e^-$	+1.498
$Au = Au^+ + e^-$	+1.691

The electrode potential cannot be determined in isolation, but with a standard electrode with the potential E^0. Often a reference hydrogen electrode is used, which is considered to have zero potential. Table 3-1

shows the standard electrode potentials of commonly used materials for electrodes.

A complete measurement setup, which comprises of a pair of electrodes and bioimpedance Z_b in between, is depicted in Fig. 3-7. The half-cell potentials, E_1 and E_2, are in series. Consequently, the net potential difference between a pair of electrodes is the algebraic difference of the potentials if no excitation current exists.

In theory, two electrodes with the same geometry which are composed of the same material should not produce a potential difference when placed in the same electrolyte. In practise, however, a nonzero net potential exists, which moreover is not constant and like the electrode polarization impedance is influenced by many factors. From our experience, a pair of stainless steel electrodes immersed in a saline solution may create a potential difference in the range of a few tens of millivolts. Even higher differences were observed when using platinum electrodes. Such unstable potentials can be eliminated, for example, by connecting the electrodes together, allowing them to reach a stable equilibrium with the electrolyte. The method is simple, but does not eliminate the problem entirely. Moreover, it must be performed before each impedance reading, and it takes at least a few seconds until stability is achieved. Often stabilization of a pair of electrodes which are contaminated asymmetrically or have differences in the surface condition, is impossible. If the contaminant is a foreign metal, a short-circuited cell of dissimilar metals is formed. This causes the current to flow in the electrolyte, thereby creating a potential field between the electrodes. This type of current flow is extremely unstable and provokes fluctuations in the net potential.

Mechanical disturbance in the area around a sensor which is in contact with an electrolyte, is likely to create a potential difference as well. It is referred to as a movement artifact. The double layer is a region of charge gradient, and thus a source of potential. Disturbing this layer produces voltage fluctuations that can be even larger than those caused by the bioelectric event being investigated. Unfortunately, movement artifacts are often in the frequency range of some of these events, hence filtering techniques can seldom be successfully employed. We found such fluctuations during an electrocardiogram (ECG) recording inside the right atrium. These fluctuations appeared to be due to the contraction movement. Fortunately, the ECG happened to have a much higher amplitude than the fluctuations caused by the movement artifacts.

3.3 Blood electrical properties

Blood is a complex system, where all major conduction and polarization mechanisms can be observed. The magnitude of each particular effect can be estimated by means of impedance spectroscopy and subsequently linked to a specific state of the main blood constituents, i.e. blood plasma and the cellular phase dispersed in it. However, one should be aware that not all of the observed mechanisms are parasitic-free. For example, interfacial polarization heavily contributes to the electrode-electrolyte interface and adds a strong noise component to the measured blood impedance. This component arises from the electrode polarization impedance. As far as blood analysis is concerned, it is expected that this phenomenon will be virtually non-existent when the applied excitation signal is above several kHz (see Fig. 3-1). The use of a four-electrode measurement techniques can further diminish the effect of the electrode polarization on the final result. Nonetheless, the half-cell potential remains and needs to be dealt with separately.

The electrical properties of blood are largely defined by two of its components: blood plasma and the red blood cells. In principle, the other cell structures presented in the cellular phase must be taken into account as well. However, their contribution is negligible and therefore they are not included in our considerations.

Blood plasma resembles a NaCl solution, since Na^+ and Cl^- ions account for 87% of its conduction. The specific conductivity of plasma is maintained by the organism at a constant level of about 14 $mS.cm^{-1}$ - 16 $mS.cm^{-1}$. Nevertheless, changes in the plasma chemistry, and particularly changes in the NaCl and protein concentrations, can alter this constant level notably.

The cellular phase reacts in a different manner with respect to the electrical current, which passes through the blood sample. The red blood cells consist of haemoglobin enveloped by a thin cell membrane. The membrane separates the intracellular from the extracellular volume, and it is built from a structured bilayer of phospholipid and protein molecules. The phospholipid bilayer is electrically inert and very thin. This results in a high specific-electrical-membrane capacitance C_{0m}. It is found to be in the range of 0.8 $\mu F.cm^{-2}$ to 1 $\mu F.cm^{-2}$. The interior of the cells is highly conductive because of the Na^+, Cl^-, Mg^{+2} and HCO_3^- ions. The conductivity values that can be found in the literature are in the vicinity of 5 $mS.cm^{-1}$.

The specific plasma resistance, the specific cell-membrane capacitance and the specific cell-interior resistance are reported in various articles as being frequency-independent but temperature-dependent. For the plasma and the cell interior resistance this dependency arises from the water-ion solution, which resembles a saline solution. Structural changes in the phospholipid bilayer, on the other hand, are reported to have great influence on the specific membrane capacitance, especially in the range around and above 37°C [3.17, 3.18].

Red blood cells are negatively charged due to the amino acids. They attract fibrinogen and other plasma proteins to form a positively charged cloud around the cell membrane, thus neutralizing its surface charges. The heavy weight and low mobility of the fibrinogen molecules in particular result in a high mechanical resistance at the membrane-plasma interface. Additionally, because of the non-symmetric shape of the red blood cells, their orientation with respect to the electrical field affects the total complex impedance measured across the blood sample. This is even more pronounced when large rouleaux clusters are formed with the help of the protein molecules, as shown in Chapter 2. Though this explanation sounds simple and fairly understandable, it is fundamental and reveals the link between the rheology of blood and its electrical properties. On the one hand, the interaction between the cells and the proteins alter the rheology of the suspension, and especially its viscosity. On the other hand, the orientation of the cells and the clusters they form strongly affect the current pathways through the sample being studied.

3.3.1 Equivalent resistance of two-phase suspension

For simplicity, blood is considered to be a two-phase (colloidal) suspension of oblate ellipsoidal (instead of biconcave) particles, homogeneously dispersed in an electrolyte solution. The first complete mathematical treatment of the equivalent resistivity and permittivity of such a system was realized by Fricke [3.19, 3.20]. The equivalent resistance of the suspension is described by the following equation:

$$R_b = \rho_p \frac{1 + Ht(C_e - 1)}{1 - Ht} \quad , \tag{3-13}$$

where R_b is the resultant blood sample resistance, ρ_p is the specific plasma resistance, Ht is the hematocrit in volume fraction, and C_e is a

factor that depends on the geometry of the cells and their orientation with respect to the electrical field. Equation 3-13 is also known as the Maxwell-Fricke equation and is based upon the consideration that the suspended particles are nonconducting in comparison with the surrounding media. For ellipsoidal particles with the diameter 2*a* and length 2*b* (*a* < *b)*, the constant C_e equals:

$$C_{e1} = \frac{1}{M} \quad \text{or} \tag{3-14}$$

$$C_{e2} = \frac{2}{2 - M} \quad , \tag{3-15}$$

where C_{e1} and C_{e2} are the values of C_e with either the *a* axis or the *b* axis parallel to the electrical field. When $\frac{a}{b} = \cos(\varphi)$ and $a < b$, the constant *M* equals:

$$M = \frac{\varphi - \frac{1}{2}\sin(2\varphi)}{\sin^3(\varphi)}\cos(\varphi) \quad . \tag{3-16}$$

Although red blood cells are considered to be shaped like bioconcave disks, this only applies when no external forces work on the membrane surface. In reality, the cells are under constant deformation which is influenced by their deformability and the surrounding flow properties. Hence, Eq. 3.13 can provide rough estimations only. Detailed information on the flow dependency of the resistivity of flowing blood can be found in: [3.21, 3.22, 3.23].

3.3.2 Equivalent capacitance of two-phase suspension

Fricke considers the equivalent electrical model of blood to be a parallel combination of a resistive and a capacitive element. In most biological systems this capacity is rather large. This is due to the polarization at the interphases of the suspension, as explained earlier in this chapter, and the static capacity of the cell membranes. In blood this has two implications. Firstly, the total bulk capacitance will depend solely on the amount of cells, i.e. on the hematocrit, and secondly, the bulk capacitance will be influenced by the arrangement of the cell clusters in

the sample studied. Our focus will be mainly on the rheology of the sample and particularly on its viscosity. Hence, our task will be to distinguish the capacitive component, which is due to the *Ht*, from the capacitive component altered by the rheological properties.

The equivalent bulk capacitance of a simplified two-phase, whole-blood suspension can be expressed as:

$$C_b = 2NC_{0m}\left(\frac{\sigma}{\sigma_1}\right)\left(\frac{n}{1-Ht}\right) \quad , \tag{3-17}$$

where C_{0m} is the specific electrical membrane capacitance, *Ht* is the hematocrit in volume fraction, and σ and σ_1 are the specific conductivities of the suspension and the suspending medium, respectively [3.20]. The number of suspended particles per unit volume is *n*. *N* is a constant which defines the single suspended particle geometrically. For ellipsoidal particles with the diameter 2*a* and length 2*b* (*a* < *b)* the constant equals

$$N = \frac{8}{9}\pi a^2 b^2\left(\frac{C_{e1}}{4M^2} + \frac{2C_{e2}}{(2-M)^2}\right) \quad , \tag{3-18}$$

where *M* is defined by Eq. 3-16 and C_{e1} and C_{e2} are expressed by:

$$C_{e1} = \frac{3}{4}\left(1 + \frac{a^2}{2b^2e^2} - \frac{a^4}{2b^4e^3}\log\left(\frac{b+be}{a}\right)\right) \quad , \tag{3-19}$$

where $e = \sqrt{1-a^2/b^2}$ is a dimensionless constant, and:

$$C_{e2} = \frac{3}{4}\left(\frac{b}{a}\right)^2\left(1 + \frac{a}{be}\log\left(\frac{a+ae}{b}\right)\right) - \frac{3}{8}\left(\frac{b}{a}\right)^2\left(1 + \frac{a^2}{2b^2e^2} - \frac{a^4}{2b^4}\log\left(\frac{b+be}{a}\right)\right). \tag{3-20}$$

3.3.3 Whole-blood equivalent electrical model

The two-element equivalent electrical model of whole blood (Fig. 3-9a) used by Fricke is suitable for the Cole-Cole model and its semicircular graphical representation. It is also applicable in cases when the specific conductivity and permittivity of the medium must be calculated. However, we found that the three-element model (Fig. 3-9b)

was more suitable for our investigations, because it offers a true reflection of the actual whole-blood electrical properties (see Fig. 1-1). In this model, R_p is the product of the specific plasma resistance ρ_p and the amount, orientation, and form factor of the cells in the blood. The bulk cell-membrane capacitance is represented by C_m, while R_i reflects the equivalent cell intracellular resistance [3.24].

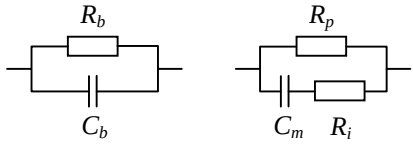

Figure 3-9: *Two-element (a) and three-element (b) equivalent electrical models of whole blood.*

The link between the two-element and three-element models at a given frequency ω can be expressed by:

$$\frac{1}{R_b(\omega)} = \frac{1}{R_p} + \frac{C_m^2 \omega^2 R_i^2}{R_i + C_m^2 \omega^2 R_i^3} \quad , \tag{3-21}$$

and

$$C_b(\omega) = \frac{C_m}{1 + C_m^2 \omega^2 R_i^2} \quad . \tag{3-22}$$

3.4 Conclusions

Complex-impedance measurement techniques demonstrate significant potential for analysing physiological phenomena and recording bioelectrical events. When an impedance-measurement sensor comes into contact with a tissue or an aqueous solution and an excitation signal is applied, conduction and polarization mechanisms occur. Blood behaves similarly to a complex biological tissue. Thus, its electrical properties involve identical conduction and polarization mechanisms. In general, the equivalent electrical model of whole blood consists of three main components: plasma resistance R_p, cell membrane capacitance C_m and cell

interior resistance R_i. The R_p component represents the specific plasma resistance affected by the amount and orientation of the cells in it. The resultant bulk cell-membrane capacitance is represented by C_m, while R_i reflects the equivalent cell intracellular resistance.

Electrodes used for impedance measurements exhibit DC offset potentials and polarization impedance, both of which can cause significant measurement errors. The offset potentials are frequently unstable and result in drift and noise. Yet, this drift is usually a low-frequency drift and can be filtered out by a read-out interface that operates in a higher frequency range. For applications that require extremely small DC offset potentials, proper selection of electrode materials is needed. The polarization impedance, at the same time, can cause a voltage drop in each sensor electrode. This can be avoided by using a sensor interface that has a high input impedance, thereby reducing the current flowing through the electrodes.

3.5 References

3.1 H. P. Shwan, “The Practical Success of Impedance Techniques from an Historical Perspective”, Annals of the New York Academy of Sciences, 1999, Vol. 873, pp. 1-12

3.2 J. J. Ackmann, M. A. Seitz, “Methods of complex impedance measurements in biologic tissue”, CRC Critical Reviews in Biomedical Engineering, 1984, Vol. 11, Issue 4, pp. 281-311

3.3 R. Peting, “Dielectric properties of body tissues”, Clin. Phys. Physiol. Meas., 1987, Vol. 8, Suppl. A, pp. 5-12

3.4 J. Nyboer, “Electrorheometric properties of tissues and fluids”, Int. Conf. on Bioelectrical Impedance, 30 July, 1970, ed S. E. Markovich Ann. NY Acad. Sci. 170, pp. 410–20

3.5 W. E. Nastuk, “Physical techniques in biological research / Volume VI, Electrophysiological methods, Prt B”, 1963, New York and London Academic press

3.6 M. E. R. Walford, “The body electric”, 1996, Phys. Educ., Vol. 31, pp. 211-215

3.7 S. O. Kasap, “Principles of electronic materials and devices”, Second edition, Mc Graw Hill, 2002, ISBN: 0072393424

3.8 J. D. Bronzino, “The biomedical engineering handbook”, CRC Press, 1995, ISBN: 0-8493-8346-3, pp. 1385-1394

3.9 U. S. Inan, A. S. Inan, “Engineering Electromagnetics“, Prentice Hall, 1998, ISBN: 0805344233

3.10 O. G. Martinsen, S. Grimnes, H. P. Schwan, “Interface Phenomena and Dielectric Properties of Biological Tissue”, Encyclopedia of Surface and Colloid Science, 2002, pp. 2643-2652

3.11 J. C. Maxwell, “Treatise on electricity and magnetism”, 1904, Clarendon

3.12 A. Bonincontro, C. Cametti, A. Di Biasio, “Effect of volume ion polarisation on Maxwell-Wagner dielectric dispersions”, J. Phys. D: Appl. Phys., 1980, Vol. 13, pp. 1529-1535

3.13 H. P. Schwan, “Electrode polarization impedance and measurements in biological materials”, Ann N Y Acad Sci. 1968, Feb. 1, Vol. 148 (1), pp. 191-209

3.14 L. A. Geddes, L. E. Baker, “Principles of applied biomedical instrumentation”, John Wiley & Sons, 1989, ISBN: 0-471-60899-8

3.15 A. Hassibi, R. Navid, R. W. Dutton, T. H. Lee, “Comprehensive study of noise processes in electrode electrolyte interfaces”, Journal of Applied Physics, 2004, Nov. 2, Vol. 96, pp. 1074-1082

3.16 P. T. Kissinger, W. R. Heineman, “Laboratory Techniques in Electroanalytical Chemistry”, Second Edition, Marcel Dekker, 1996, ISBN-0824794451

3.17 P. Heroux, M. Bourdages, “Monitoring living tissues by electrical impedance spectroscopy”, Annals of Biomedical Engineering, Vol. 22, pp. 328-337, 1994

3.18 Jian-Zhong Bao, C. Davis, R. Schmukler, “Frequency domain measurements of erythrocytes - Constant phase angle impedance characteristics and a phase transition”, Biophys. Journal, Vol. 61, May 1992, pp. 1427-1434

3.19 H. Fricke, “A mathematical treatment of the electric conductivity and capacity of disperse systems, I. The electric conductivity of a suspension of homogeneous spheroids”, Phys. Rev., 1924, Vol. 24, pp. 575-587

3.20 H. Fricke, “A mathematical treatment of the electric conductivity and capacity of disperse systems, II. The Capacity of a suspensions of conducting spheroids surrounded by a non-conducting membrane for a current of low frequency”, Phys. Rev., 1925, Vol. 26, pp. 678-681

3.21 K. R. Visser, “Electric properties of flowing blood and impedance cardiography”, Annals of Biomedical Engineering, Vol. 17, pp. 463-473, 1989

3.22 A. E. Hoetink, Th. J. C. Faes, K. R. Visser and R. M. Heethaar, “On the flow dependency of the electrical conductivity of blood”, IEEE Transactions on Biomedical Engineering, Vol. 51, No. 7, July 2004

3.23 J. Wtorek and A. Polinski, “The contribution of blood-flow-induced conductivity changes to measured impedance”, IEEE Transactions on Biomedical Engineering, Vol. 52, No. 1, January 2005

3.24 H. Fricke, S. Morse, “The electrical resistance and capacity of blood for frequencies between 800 and $4\frac{1}{2}$ million cycles”, The Journal of General Physiology 9, pp. 153-157, 1925

4 *In vivo blood analysis system*

The essence of the major blood rheological properties as well as the associated clinical applications were discussed in Chapter 2. Chapter 3 linked the main blood rheological properties to the corresponding blood electrical properties. The current chapter describes a dedicated impedance-measurement system, named HemoCard Vision (HCV), which has been designed to perform the electrical analysis of whole blood.

HemoCard Vision can be described as an online hematology and cardiology diagnostic system which comprises of:

- A central venous catheter (CVC)
- Interface electronics
- Data processing software
- A PC or PDA computer medium

Figure 4-1 shows the measurement system and its specially developed catheter. The catheter includes a four-electrode impedance sensor and a thermistor located at the distal end, near the tip. With the existing three lumens for administering fluid infusions and/or measuring atrial pressure, the catheter features all characteristic functionalities of a standard central venous catheter alongside with capabilities for the measurement of whole-blood impedance, intracardiac ECG, and temperature [4.1].

As a result of a direct measurement and/or additional data post-processing, the system derives a set of results that consists of:

- Hematocrit (derived from the plasma resistance R_p)
- Blood viscosity (derived from the cell membrane capacitance C_m)
- Intracardiac ECG
- Core body temperature

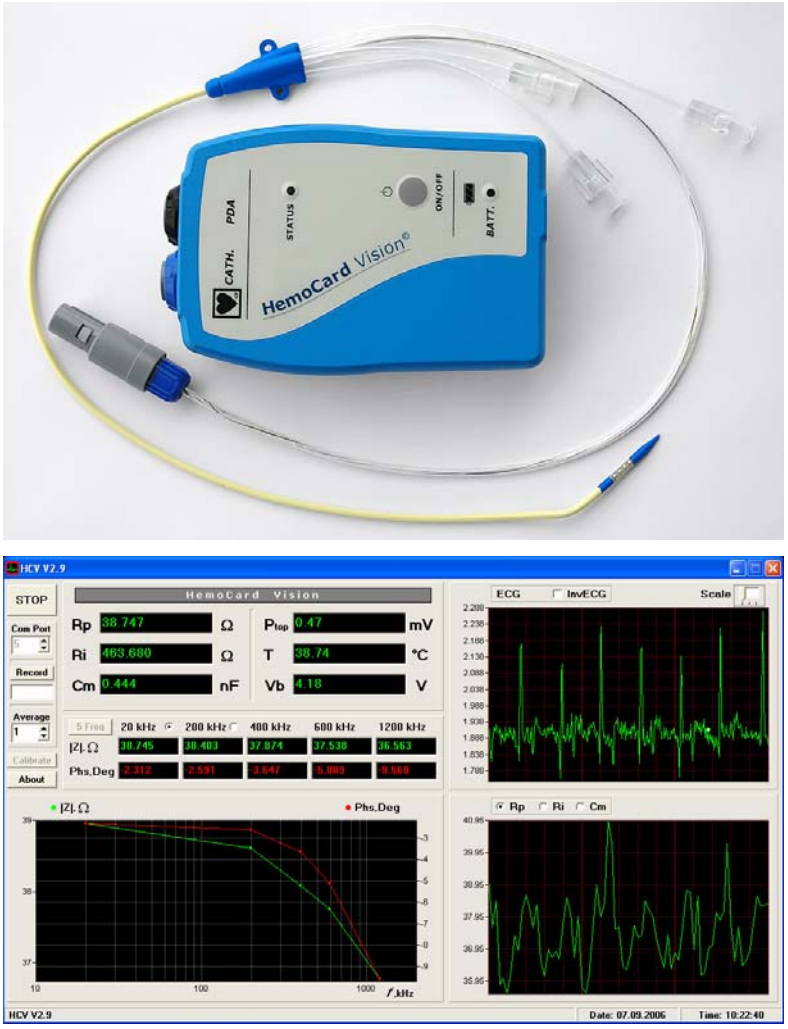

Figure 4-1: *HemoCard Vision blood analysis system.*

The measurement system can work in either continuous or trend mode. In continuous mode, it captures and displays a full set of results every 40 ms. The ECG signal is captured every 10 ms or every 1 ms depending on the measurement mode. In trend mode, a set of results covering 18 s in time is captured every 10 min and the data is stored in the internal memory for subsequent post-processing.

The system depicted in Fig. 4-1 was put to the test in a clinical *in vivo* pilot study, the results of which will be shown in Chapter 5. During this study, a number of shortcomings related to both the catheter and the interface electronics were identified. These shortcomings were rectified, resulting in the creation of a new, second generation HemoCard Vision which is also described in this chapter.

4.1 Central venous catheter

Figure 4-2 shows the HemoCard Vision catheter next to a standard central venous catheter made by Arrow.

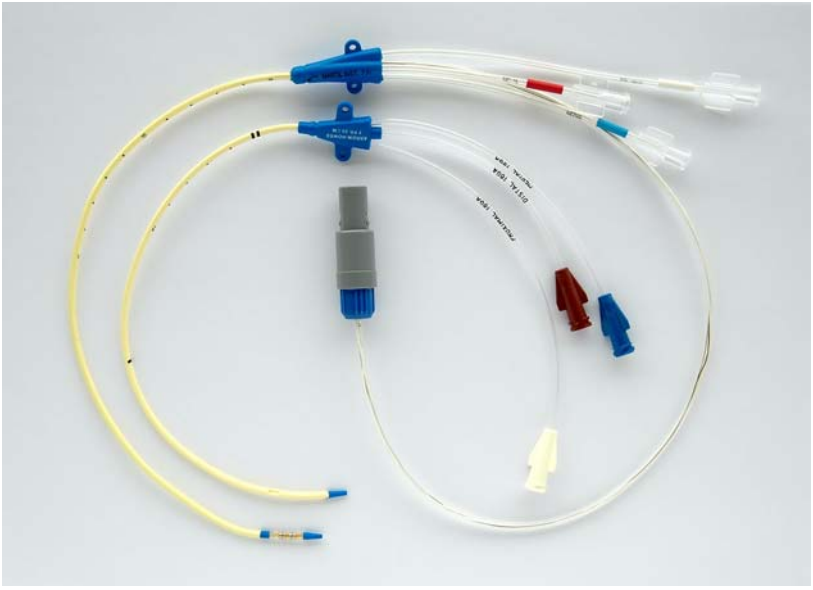

Figure 4-2: *A HemoCard Vision catheter next to a standard central venous catheter made by Arrow.*

The HemoCard Vision catheter is a 7.25 Fr (2.41 mm in diameter) catheter and measures 25 cm in length[1]. Normally, it is introduced by applying the standard Seldinger technique in either the left subclavian vein, the right subclavian vein or the right jugular vein of the patient, after which it is advanced through the superior vena cava into the right atrium. The catheter has been paired with a standard 0.022″ guidewire[2].

The body of the catheter is made of polyurethane. It is torsionally stiff, which enables proper orientation of the tip inside the right atrium. At the same time, the body is sufficiently soft so that the guidewire used during the introduction is able to straighten the bent tip section (Fig. 4-3). The angle of the bend is specifically set such that the tip of the catheter can be optimally positioned in the middle of the atrium and away from the atrial wall.

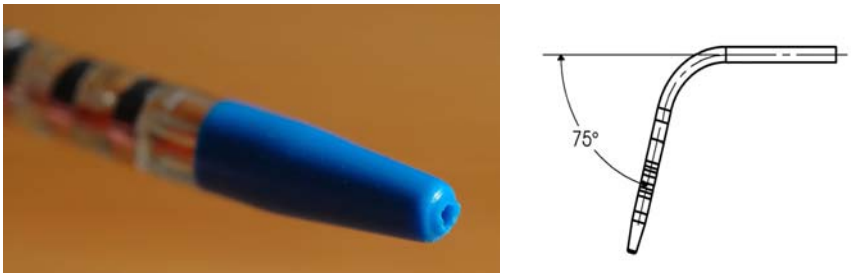

Figure 4-3: *Catheter tip section.*

In order to avoid mechanical bending, which may change the cell constant of the sensor, the electrode housing is made from stiffer polyurethane. The tip (distal section, Fig. 4-3) is made of extra soft material (polyurethane 80 ShA) to avoid damage of the atrial wall.

The catheter's extrusion profile reveals four lumens (Fig. 4-4). All of the cables are situated in the biggest lumen. The thermistor is placed in the same lumen. For better thermal contact, the cavity around the thermistor is filled with UV resin. Because of the catheter flexibility required to facilitate excessive bending, special care had to be taken to reduce the friction between the cables. Therefore, cables insulated with fluorinated ethylene-propylene were used.

[1] The French scale, abbreviated as Fr, is commonly used to measure the size (outside diameter) of a catheter. 1 Fr = 0.33 mm.
[2] It is typical for the catheter industry to denote the guidewire size (outside diameter) in inches.

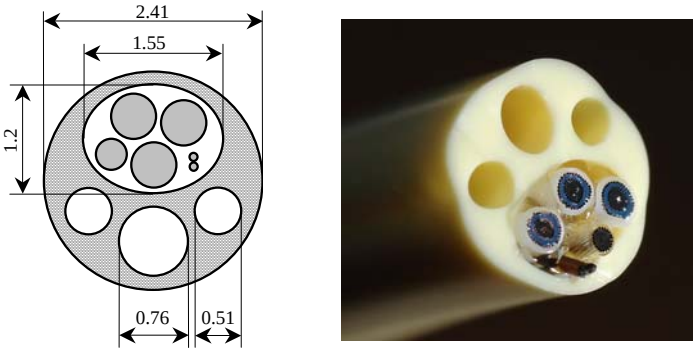

Figure 4-4: *Catheter extrusion profile (all sizes are in millimeters).*

The outlets of the two 25 GA (0.51 mm) lumens are located 10 cm (proximal lumen) and 5 cm (medial lumen), respectively, from the tip[1]. The 22 GA (0.76 mm) lumen outlet is at the tip of the catheter (see Fig. 4-3). This lumen is also know as the distal lumen.

The flow rates through the lumens were estimated by applying a standard test procedure using both NaCl and Voluven. The flow rate through the distal lumen averaged 715 ml/hr. The middle and proximal lumens had average flow rates of 311 ml/hr and 393 ml/hr, respectively. Such flow rates have been considered insufficient for a standard CVC. For comparison, a 7 Fr, three-lumen, 30 cm long Arrow catheter offers two 22 GA (0.76 mm) and one 19 GA (1.016 mm) lumen with flow rates of 1000 ml/hr and 2300 ml/hr, respectively. Additionally, the pilot study revealed difficulties advancing the catheter during introduction due to the excessive flexibility of the catheter and its 0.022″ guidewire.

In order to overcome these problems, we redesigned the catheter by increasing its overall size. The so-called second-generation HemoCard Vision catheter is a 8.25 Fr (2.74 mm in diameter) catheter and measures 30 cm in length. The distal lumen was increased to 19 GA (1.016 mm), while the size of the proximal and medial lumens was increased to 23 GA (0.61 mm). A stiffer 0.025″ guidewire could then be used during introduction. The combination of the bigger giuidewire and the stiffer catheter shaft ensures notably easier catheter introduction, with the dimensions of the sensor left unchanged.

[1] The standard wire gauge scale (S.W.G.), abbreviated as GA, is commonly used to measure the size (diameter) of the lumens.

Hydrophilic coating

The long-term stability of the measured results as well as the hemocompatibility of the HemoCard Vision catheter were enhanced by applying a hydrophilic coating [4.2, 4.3]. This coating prevents biolayer formation and greatly reduces the coefficient of friction between the catheter and the vessel wall, thus eliminating tissue irritation and damage. The entire catheter shaft, excluding the electrodes, is covered by the coating, which features the following key characteristics:

- Heparin-based hydrophilic coating
- Covalently bound technology–heparin is not eluted and does not have a systemic effect on the body
- Sterilization-compatible (EtO, gamma, e-beam)
- Thin conformal coating–less than 5 μm thick
- Reduced platelet adherence, thrombus formation, and insertion forces
- Resistant to enzymatic degradation

4.1.1 Impedance sensor and electrode housing

The electrode housing, shown in Fig. 4-5, supports the metal electrodes and provides distal lumen channelling. Establishing low-impedance contact with the blood is the main requirement for the impedance sensor. While it is in direct contact with the patient, capturing both, blood electrical impedance and ECG, the sensor should also:

- Provoke minimal tissue or allergic response
- Develop an adequate electrical field
- Create a low polarization impedance
- Maintain a stable half-cell potential
- Radiographically be visible

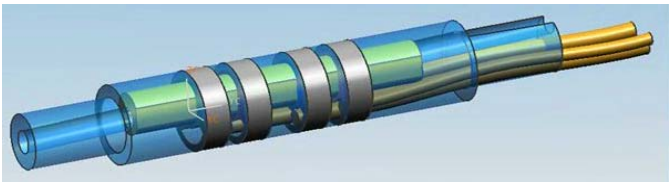

Figure 4-5: *Electrode housing and impedance sensor.*

Except for the electrical field distribution, which mainly depends on the sensor configuration and geometry, all of the above-listed requirements are related to the materials used for the sensor and its supporting structure. A comprehensive overview of the criteria for selecting materials for implanted electrodes can be found in [4.4].

Biocompatibility and Hemocompatibility

The body of the catheter is in direct contact with the patient when implanted. As such, it should not provoke a tissue allergic response, which depends on many factors. Under the assumption that biocompatible materials have been used for the catheter and its electrodes, one should concentrate on the surface-condition of the catheter in order to achieve sufficient biocompatibility and hemocompatibility.

When a metal is implanted, an inflammatory reaction occurs and triggers a response, which results in the encapsulation of the implant in a fibrous tissue. Such a tissue, also known as a biolayer, is shown in Fig. 4-6 (on the surface of the uncoated-catheter).

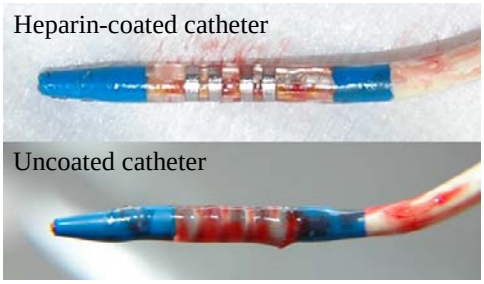

Figure 4-6: *A biolayer-free, heparin-coated catheter, and an uncoated catheter, encapsulated in a biolayer after being implanted for five days.*

The encapsulation may consist of fibroblast, fibrin, macrophages, lymphocytes, plasma cells and mast cells. Its thickness and surface adhesion depends on the implant material, surface shape and condition.

Figure 4-6 shows an uncoated catheter covered with an endothelium biolayer that formed over just a few days. The rest of the catheter was not affected. It has been concluded that the surface-roughness of the polycarbonate material that supports the electrodes triggers the encapsulation response. At a later stage, polyurethane was used instead of

polycarbonate. Additionally, the surface of the housing was coated with UV glue, which further improved the surface smoothness. Nonetheless, the formation of a biolayer was prevented completely only after introducing the heparin coating. With respect to the metal electrodes, no difference has been found between stainless steel and platinum electrodes.

Equivalent electrical model

The impedance of an electrode-electrolyte interface depends on the metal, the nature of the electrolyte, the surface area, the temperature, and the current density. This polarization impedance decreases when either the area or surface roughness of the electrode increases. An excitation signal with a higher frequency or a higher current density may further diminish the electrode-electrolyte-interface impedance. As described in Chapter 3, the equivalent electrical model of such an interface consists of a half-cell potential, a Warburg element and a Faradic impedance. The latter accounts for the very-low-frequency and direct-current properties, while the Warburg component accounts for the alternating-current impedance. The contribution of the polarization impedance to the final measurement can be cancelled by applying the following techniques:

Substitution technique: The sample being analyzed, which has unknown impedance properties, is replaced with a sample that has known properties. The latter is chosen such that its electrode impedance approximates that of the unknown sample and serves to determine the polarization impedance.

Electrode-distance variation technique: This technique is applicable when the cell constant of the sensor can be varied by changing the electrode distance or the geometry of the sample between the electrodes. For two different cell constants, the following equations apply:

$$Z_{m1} = Z_p + Z_{s1} \tag{4-1}$$

$$Z_{m2} = Z_p + Z_{s2} \ , \tag{4-2}$$

where Z_m is the impedance measured between the electrodes, Z_p is the polarization impedance, and Z_s is the impedance of the liquid. By subtracting:

$$Z_{m1} - Z_{m2} = Z_{s1} - Z_{s2} \quad , \tag{4-3}$$

which is independent of Z_p, one can accurately estimate the impedance of the sample portion.

Frequency-variation technique: Often the cell constant cannot be varied. In this case, the technique of choice is variation of the applied frequency, which provides a similar analysis of the observed results.

Four-electrode technique: This technique eliminates the electrode polarization effect on the measurement results altogether. Using sensing circuitries with a high input impedance eliminates the current flowing through the polarization impedances at the sensing electrodes. As a result, the measured signal is proportional to the current, which passes through the sample and the impedance between the electrodes.

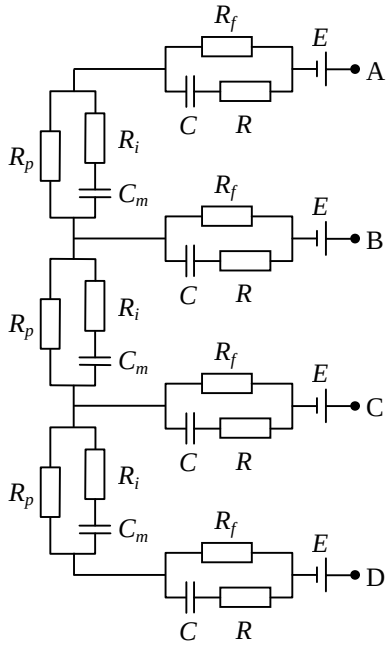

Figure 4-7: *Equivalent electrical model of a four-electrode sensor immersed in blood.*

Choosing the most appropriate technique to correct the polarization impedance depends on the particular measurement setup and its specific limitations. Additionally, an impedance sensor immersed in blood often develops a thin biolayer coating. This results in a measurable contact impedance that adds to the polarization impedance. In this case, the use of the four-electrode technique is a must.

A complete electrical model of a four-electrode sensor immersed in blood, is shown in Fig. 4-7. Electrodes A and D are the excitation (current) electrodes. Electrodes B and C are the measurement (potential or sense) electrodes.

Half-cell-potential stability and ECG noise considerations

The electrical characterization of blood takes place typically at frequencies that exceed 20 kHz. Hence, the measured signals will not be affected by the fluctuation in the half-cell potential when a proper signal filtering is applied. However, in our system, signals occupying the millihertz range are important and had to be considered as well. For example, the ECG signal we measure, covers the bandwidth from 0.5 Hz to 250 Hz [4.5].

With respect to the ECG signal and data processing, there are three main noise sources that should be taken into account in this frequency range. These include baseline wander, power line interference, and muscle noise. The baseline wander can be due to perspiration, respiration or body movements and may negatively affect the ECG analysis. The half-cell potential is considered to be a DC component. Nonetheless, it demonstrates some fluctuations that contribute to the baseline wander noise as well.

In theory, two electrodes with the same geometry and consisting of the same material should not produce a potential difference if placed in the same electrolyte. In practise, a pair of measurement electrodes is always asymmetrically contaminated or has differences in the surface condition, thus creating a nonzero net potential. This potential is not constant, and as with the electrode polarization impedance, it is influenced by many factors. We have measured fluctuating potential differences in the range of a few tens of millivolts using a pair of stainless steel electrodes.

Mechanical disturbance in the area around a sensor which is in contact with electrolyte is likely to provoke a potential difference as well. It is referred to as a movement artifact. Because the double layer is a region with charge gradients, and thus a source of potential, disturbance of it

causes voltage fluctuations that can be even larger than the magnitude of the bioelectric ECG event.

Electrical field distribution

In a series of *in vivo* animal trials, the catheter impedance-sensor was optimised for better performance, especially for the moments when excessive heart rates occur. High heart rates can in theory cause deviation in the measured parameters due to an affection of the impedance measurements by the approach of the atrial wall during each contraction. The right atrium diameter is about 41 mm in an average-sized adult [4.6], but it may shrink down to 25 mm at very high rates, from our observations. Precise experiments have estimated the exact electrical-field-distribution profile around the electrodes (Fig. 4-8). The tests were carried out in glass tubes with different diameters filled with saline solution. The sensor has been designed in such a way that its electrical field optimally covers the right-atrium size and shows no deviation from the overall *in vitro* picture over a large range of heart rates. The latest results were obtained in a series of animal trials with sheep. The highest rate we reached was 175 beats/min.

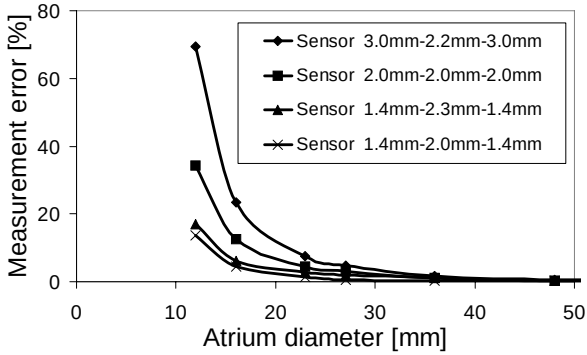

Figure 4-8: *Measurement error induced by the limited electrical-field distribution for various sensor configurations that include four 0.8 mm wide stainless steel electrodes. The distance between the electrodes is measured centre-to-centre. The tests were carried out in glass tubes with different diameters filled with saline solution.*

Figure 4-9 shows the two different sensor configurations we used to examine the electrical field distribution *in vivo* in a sheep. The bottom one measures (centre-to-centre) 2.0 mm-2.0 mm-2.0 mm between the rings and, as predicted by our *in vitro* electrical-field-distribution analysis, resulted in impedance measurements that were strongly affected by the atrial wall. At the same time, the sensor measuring 1.4 mm-2.0 mm-1.4 mm in dimension demonstrated results almost unaffected by the atrial contractions.

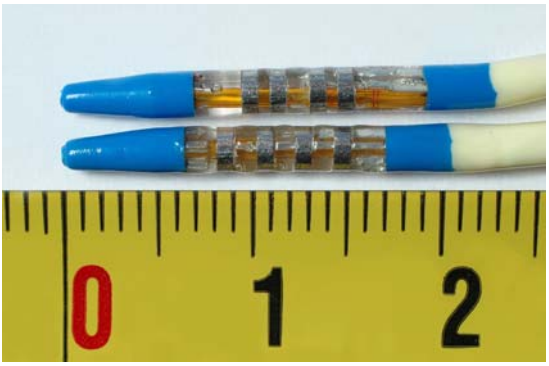

Figure 4-9: *Two different sensor configurations used to examine the electrical field distribution in vivo in a sheep. The distance between the electrodes measures 1.4 mm-2.0 mm-1.4 mm for the top one and 2.0 mm-2.0 mm-2.0 mm for the bottom one (measured centre-to-centre).*

Addition information and general considerations related to the electrical field distribution for various sensor configurations can be found in [4.7].

Radiographic visibility

Radiographic visibility of an implant is a common requirement. It is highly desirable to be able to monitor the placement of the catheter and the integrity of the sensor, especially if an abnormal response is encountered. Implanted electrodes are often small, therefore it is wise to select a metal that absorbs X-rays strongly. This narrows the choice of metals to those with higher atomic number. Gold, platinum, platinum-iridium, tungsten and tantalum are among the most radiographically visible materials. For

larger implants, the atomic number is less important. Despite the use of stainless steel electrodes, our sensor is well visible, as shown in Fig. 4-10.

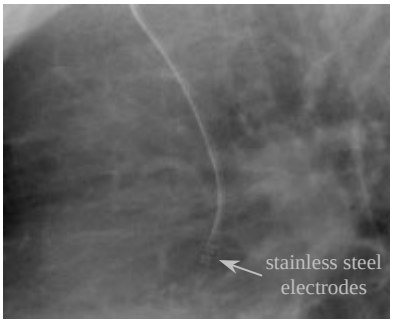

Figure 4-10: *X-ray image of the HemoCard Vision catheter.*

MRI safety consideration

The growing popularity of interventional magnetic resonance imaging (MRI) has introduced a new range of safety requirements for this medical equipment. Radio-frequency (RF) heating of guidewires, catheters, and other wire-shaped devices during MRI has given raise to important safety issues [4.8, 4.9]. In order to estimate the MRI safety level of the HemoCard Vision catheter, we have considered the regulations issued by the US Food and Drug Administration (FDA). These regulations include the following three groups of devices:

MR-Safe: The device or implant is completely non-magnetic, non-electrically conductive, and non-RF reactive, eliminating all of the primary potential threats during an MRI procedure.

MR-Conditional: A device or implant that may contain magnetic, electrically conductive or RF-reactive components that is safe for operations in proximity to the MRI, provided the conditions for safe operation are defined and observed.

MR-Unsafe: Objects that are significantly ferromagnetic and pose a clear and direct threat to persons and equipment within the magnet room.

In general, electric conductors, even if not ferromagnetic such as metallic elements or cables situated near or inside the human body, could potentially cause hazardous heating in the surrounding tissue due to induced currents during MRI scanning. Therefore, the ring electrodes and connecting wires of the catheter have been identified as a potential source of concern. The ring electrodes are relatively small and the resulting

specific absorption rate (SAR) is expected to fall within the safety limits. This opinion is based on literature sources reporting experimental results with metal objects of a similar configuration that have been examined in a standard (up to 1.5 T) MRI safety test. It is expected that the HemoCard Vision catheter will be rated as MRI-conditional in this respect.

The maximum length of a wire during an MRI scan needs to be shorter than the RF-electromagnetic wave length, e.g. shorter than 20-30 cm. Longer wires result in standing electromagnetic waves that cause heat dissipation at both wire ends. One coaxial and three triaxial cables are connected to the metal electrodes inside the HemoCard Vision catheter. The core wires of these cables are connected to the rings while the shields are loose at the tip of the catheter. It is known that, in the case of shielded cables, the RF-electromagnetic waves induce current in the outer conductor only. Therefore, heat dissipation will not occur in the core wires. This heat dissipation effect will be observed within the shields, but since they are buried deep inside the catheter, the result is a very high thermal resistance between the heat source and the surrounding tissue. This will help in cases when the MRI scan time is too short to allow enough time for the heat generated in the cables to reach the surface of the catheter. It is expected, that the HemoCard Vision catheter will also be rated as MRI-conditional with respect to its connecting wires.

4.1.2 Detection of intracavitary ECG. Sensor positioning

From an electrical stand point, the contraction of the cardiac muscle is associated with electrical changes called depolarization. The electrical discharge for each cardiac cycle normally starts in a special area of the right atrium called the sinoatrial node (SA node, Fig. 4-11). Depolarization then spreads through the atrial muscle fibres. There is a delay while the depolarization spreads through another special area in the atrium: the atrioventricular node (AV node). Thereafter, the electrical discharge travels very rapidly down specialized conduction tissue: first down a single pathway–the bundle of His–which splits in the septum between the ventricles into right and left bundle branches.

Within the mass of the ventricular muscle, conduction spreads somewhat more slowly through specialized tissue called Purkinje fibres. These electrical events can be detected by electrodes attached to the surface of the body as well as electrodes placed inside the right atrium. Hence, our sensor, being located inside the right atrium (RA), detects signal which is a mixture of an impedance and an ECG signal.

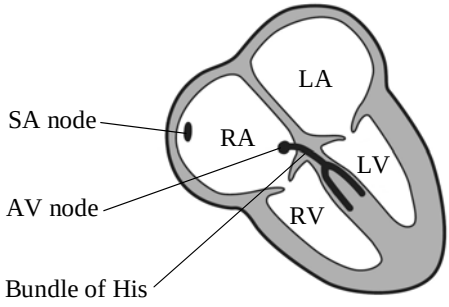

Figure 4-11: *A simplified cardiac-conduction-system model.*

Figure 4-12 shows a typical internal ECG signal for a well-positioned catheter, as measured with the HemoCard Vision. The figure shows four consecutive cardiac cycles. Each cycle starts with the P-wave, which represents the atrial contraction, followed by the QRS-complex and the T-wave.

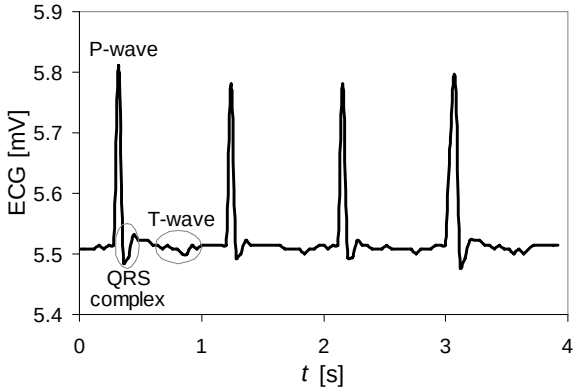

Figure 4-12: *Intracavitary ECG as measured with the HemoCard Vision.*

The QRS-complex is readily visible once the catheter is introduced deep into the right atrium, i.e. beyond its ideal position. On the contrary, it is expected that the QRS-complex amplitude is relatively low for a well-positioned sensor (one example is depicted in Fig. 4-12). Hence, the heart rate should typically be estimated by measuring the time between the P-waves. Therefore, the heart rate cannot be determined with the

HemoCard Vision in patients with atrial fibrillation, AV-block or ventricular arrhythmias.

When triggering the impedance measurements on the intracavitary ECG signals, the impedance samples should be taken ideally at the end of diastole, just before the atrial contraction. At that moment the right atrium is completely filled with blood and the impedance signal is least influenced by the proximity of the atrial wall. Furthermore, at this moment the flow in the atrium is low and hence the blood viscosity will be at its highest level.

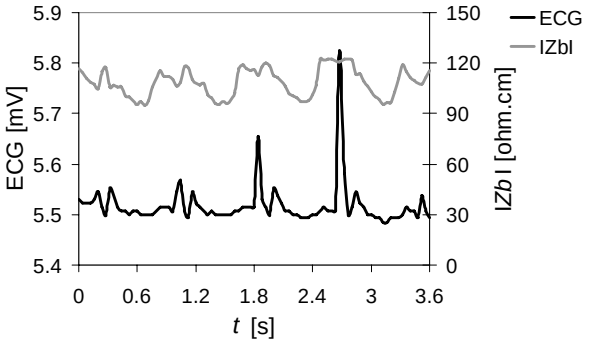

Figure 4-13: $|Z_b|$ *and ECG measured in vivo in a sheep.*

Figure 4-13 shows $|Z_b|$ and ECG as measured *in vivo* in a sheep. Clearly, the atrial wall has the least effect on the measured impedance during the T-wave. Thus, proper ECG-data processing and the implementation of a triggering algorithm are essential for correctly estimating the moment when the impedance has to be measured.

Positioning a central venous catheter is sometimes guided and often controlled afterwards with an X-ray. The form and amplitude of the internal ECG measured by the HemoCard Vision system can also be used to indicate the precise sensor location. Therefore, an X-ray is no longer needed for confirmation of the right position. An ECG sensor, which is located high in the atrium, results in a high P-wave amplitude and an almost indistinguishable QRS-complex pattern and vice versa: a sensor positioned close to the tricuspid valve gives a low P-wave amplitude and a high QRS-complex amplitude. Based on our measurements, the optimal sensor position corresponds to P-wave amplitudes in the range from 0.3 mV to 0.8 mV. Note that these levels are specific for our sensor only.

4.2 Interface electronics

The equivalent electrical model for blood was determined by Fricke back in 1925 [4.10]. As described in Chapter 3 and depicted in Fig. 3-9b, the hematocrit is represented by R_p, the cell's interior resistance is represented by R_i, while C_m is the cell membrane capacitance, which was found to be in good correlation with whole blood viscosity.

As with any living tissue, blood impedance has frequency-dependent behaviour. For frequencies below 100 kHz, the electrical current passes through the plasma only, while the cell membranes act as insulators. For frequencies above 200 kHz, the electrical current passes through the phospholipid membrane layer and is strongly affected by the high specific capacitance of the membrane. Therefore, an accurate R_p measurement can be carried out in the sub-100 kHz frequency range, while an accurate measurement of C_m and R_i can only be obtained above several hundred kHz. Figure 4-14 shows a typical impedance plot of human blood.

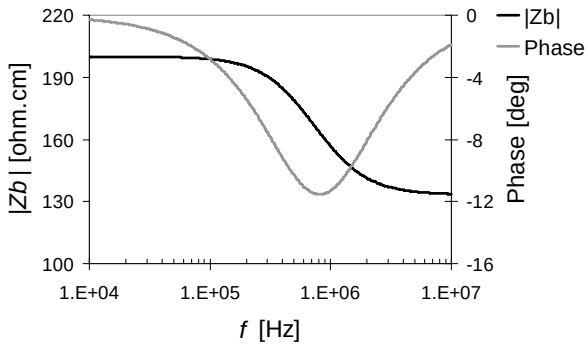

Figure 4-14: *Typical complex-impedance plot of whole blood.*

Measurement methods

Blood-complex-impedance characterization, which is also known as blood impedance spectroscopy, has been carried out by many research groups in a wide frequency range from a few Hz up to a few GHz [4.10-4.12]. The investigations have mainly focused on the hematocrit dependence [4.13-4.15], flow [4.16-4.18], and temperature-induced changes to the measured complex-impedance parameters [4.11, 4.19]. The red blood cell aggregation, sedimentation rate and fibrinogen

concentration and their influence on the measured impedance have become interesting research topics as well [4.20-4.22]. The instrumentation used to conduct these measurements include two and four-electrode sensors as well as square and sinusoidal-wave excitation signals. In general, the wide variety of existing bioimpedance measurement methods can be summarized into the following four groups:

Transimpedance methods: The passive electrical properties are reconstructed from transimpedance data obtained by injecting currents into the object and measuring the potential differences between selected surface points. The measurement device is coupled to the object via electrodes. The frequencies range from a few Hz to several MHz.

Transmission line methods: In the middle of the 20th century the frequency range was extended towards several GHz. Tissue characterization in this range is mostly based on measuring the reflection coefficient of a coaxial transmission line or of a wave-guide, which is terminated by the sample. Measurements of the resonant frequency of cavity resonators have been applied as well.

Microwave methods: One of the most recent disciplines in the bioimpedance field is microwave tomography, where a microwave field is coupled to the object via antennas. The information is obtained by measuring the scattered electromagnetic field.

Inductive methods: In the 1970s the “magnetic sounding” method was introduced to biomedical research. This approach, which was originally applied in geophysics, is based on coupling an alternating magnetic field to the object. The weak response field, which is generated by the induced eddy currents, is then measured via pick-up coils.

4.2.1 HemoCard Vision: first generation

Figure 4-15 shows a block diagram of the HemoCard Vision interface electronics we have designed to perform the electrical characterization of whole blood. The interface is built around the phase-gain analyzer AD8302 [4.23] and applies the transimpedance measurement method.

The AD8302 integrates two closely matched wideband demodulating logarithmic amplifiers and a wideband digital phase detector which measure the magnitude ratio and phase difference, respectively, between two independent input signals. By applying both a reference signal to one of the AD8302 inputs and the voltage difference measured between the sense electrodes to the other AD8302 input, we are able to measure the whole-blood complex-impedance magnitude, given that the excitation

current through the sensor and the signal-path gain are known. The magnitude of the measured complex impedance is then used to compute the three components found in the whole-blood equivalent electrical model. In order to do this, we need to measure the magnitude of the unknown impedance at least at three different frequencies. In this method, the phase information of the complex impedance is not used. This is because, firstly, the AD8302 phase channel shows a higher relative error in comparison with the AD8302 gain channel, and secondly, the phase difference between the two AD8302 input signals depends largely on the excitation-electrode polarization impedance.

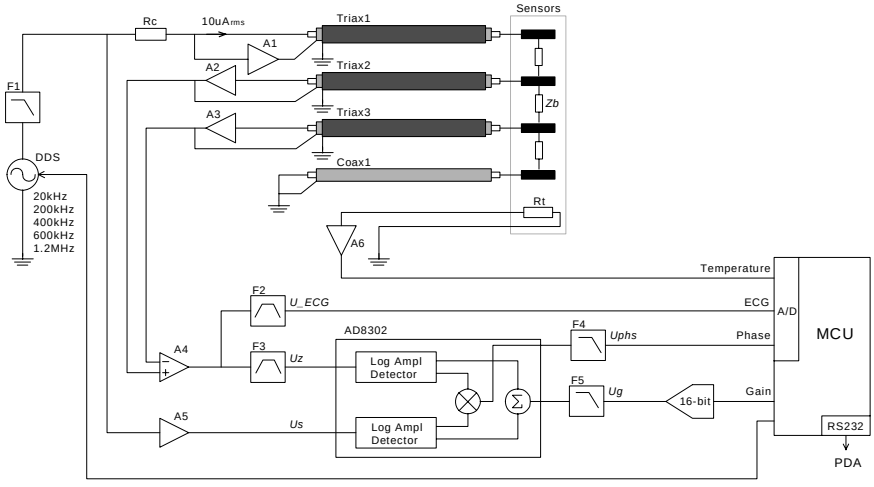

Figure 4-15: *Block diagram of the interface-electronics of the first generation HemoCard Vision.*

The whole-blood complex-impedance is measured by applying a sinusoidal excitation signal at five discrete frequencies: 20 kHz, 200 kHz, 400 kHz, 600 kHz, and 1.2 MHz. The frequencies are applied consecutively each for 8 ms at a time. A direct digital synthesizer DDS (AD9832BRU) generates the excitation signals, which signals are filtered by F1 (AD8039AR) and then applied to the high-potential excitation electrode via a clamp resistor R_C. F1 is a low-pas, third-order, Butterworth filter with a cut-off frequency of 2.85 MHz. The cut-off frequency selected is lower than half of the clock frequency (20 MHz) of the direct digital synthesizer, which according to the theory is sufficient to recover a perfect sine wave [4.24]. At the same time, the AD9832BRU has a clock

frequency feedthrough of -60 dBc, which F1 is expected to improve by adding approximately -50 dB to it.

The voltages at the two sense electrodes are buffered by A2 and A3 and then fed to the differential amplifier A4 (OPA4820). In order to minimize the effect of the electrode polarization impedance and electrode contact resistance, the current through the sense electrodes should be minimal; therefore, the buffer amplifiers should have a high input impedance. The general recommendation for the amplifiers used to record bioelectric events is to have a common-mode input impedance higher than 100 MΩ [4.25]. Therefore, for A2 and A3 as well as for A1 we used OPA656U, which has an FET input.

The connecting cables have a stray capacitance C_s of 75 pF. This capacitance induces phase and gain errors. Eliminating these errors is achieved by applying active guarding. The downside of this solution is the potential instability of the buffer amplifiers. This instability is caused by the positive feedback from the stray capacitance. Let us consider a single buffer with a first-order, low-pass transfer function:

$$G(s) = \frac{1}{1 + s\tau_1} \quad , \tag{4-4}$$

which feeds a single coaxial cable attached to the patient via a metal electrode. This configuration, in which the measured signals enter at the electrode side and exit at the output of the buffer amplifier, has the following response:

$$H(s) = \frac{1 + \tau_1 s}{1 + \tau_1 s + \tau_1 \tau_2 s^2} \quad . \tag{4-5}$$

The time constant $\tau_2 = C_s R_e$ is defined by the stray capacitance and the total electrode serial resistance R_e [4.26]. The characteristic polynomial (4-5) is of the second order and has positive coefficients. Therefore, its roots have a negative real part and the circuit should be stable for any τ_1 or τ_2 [4.27].

In order to satisfy the electromagnetic-emission requirements of the IEC60601 norm, the actively-guarded cables are enveloped by a second, grounded shield. The capacitance between the first and the second shield of each cable is about 290 pF. This capacitance loads the A1, A2 and A3 outputs, and together with the output resistance of the amplifiers, creates a

second pole in the $G(s)$ (Eq. 4-4). In order to avoid peaking in the buffer transfer characteristic, we cancelled the additional pole by adding snubbing resistors at the output of each buffer. The values of these resistors were optimized by examining the step response of the active guarding circuit.

The tip of the catheter is located inside the right atrium, between the sinoatrial node and the atrioventricular node. Consequently, the signal after the differential amplifier A4 is a mixture of an impedance signal and an ECG signal. The ECG component covers the frequency range from 0.5 Hz to 250 Hz. The impedance signal covers the bandwidth from 20 kHz to 1.2 MHz. Thus, the two signals can be separately extracted from the mixture with proper filtering. This is done by incorporating the two band-pass filters F2 and F3.

F2, which extracts the ECG component, consists of a low-pass, third-order Butterworth filter followed by a high-pass, first-order filter. An optimally positioned catheter results in an impedance and an ECG signals that have roughly the same amplitudes. Hence, the third-order filter, which has a corner frequency of 1 kHz, ensures a minimum signal-to-noise ratio of 78 dB with respect to the impedance signal when the catheter is in its optimal position.

The high-pass filter has a corner frequency of 1.59 Hz and it filters out the fluctuations of the half-cell potential. Typically, these fluctuations have a period of a few seconds and a maximum peak amplitude of a few hundred of microvolts, as measured with our sensor.

F3, which extracts the impedance signal U_z, consists of a low-pass, first-order filter followed by a high-pass, third-order Butterworth one. The low-pass filter has a corner frequency of 10.3 MHz. It aims to improve the system immunity in the frequency range between 80 MHz and 2.5 GHz, which is a common IEC60601-norm requirement. A theoretical analysis of the system susceptibility to signals in this range has been hindered by the complexity of the connecting cables. Therefore, the filter has been optimized by measuring the system response in the standard test setup described in the IEC60601 norm, and by applying an electrical field with a strength of 3 V/m.

The high-pass, third-order part of the F3 filter has a corner frequency of 2 kHz and aims to sufficiently suppress the T wave while the impedance measurements are being performed. The highest T-wave amplitude we recorded had a peak level of 80 μV. In terms of bandwidth, the T-wave resides in the low end of the ECG spectrum, below 20 Hz

[4.28, 4.29]. Typically, the impedance-signal peak amplitude will be higher than 0.5 mV. Then, the signal-to-noise ratio with respect to the T-wave will exceed 135 dB. While such a high signal-to-noise ratio is not a must, we have designed the filter such that it will also ensure a decent 53 dB suppression for all ECG components.

A Butterworth-type of filter is used in all three filters: F1, F2 and F3. This ensures a maximal flatness in the transfer characteristics of the signal channels.

Already filtered, the impedance signal U_z is compared with the source signal U_s by the phase-gain analyzer. The magnitude ratio of the compared signals and their phase difference are converted into DC voltages U_g and U_{phs} according to the equations:

$$U_g = U_{gslp} \log \frac{U_Z}{U_S} = U_{gslp} \log \frac{k|Z_b|}{|R_c + 3kZ_b + 2Z_p|} \approx U_{gslp} \log \frac{k|Z_b|}{|R_c + 3kZ_b|} \quad (4\text{-}6)$$

$$U_{phs} = U_{pslp}(\varphi(U_z) - \varphi(U_s)) \approx U_{pslp}\varphi(U_z) \quad , \quad (4\text{-}7)$$

where Z_b is the complex impedance, which consists of R_p, R_i and C_m (Fig. 3-9b), Z_p represents the polarization impedance of the excitation electrodes, k is the cell constant of the sensor and $\varphi(U_z)$ is the phase of Z_b. The gain slope-voltage U_{gslp} and phase slope-voltage U_{pslp} of AD8302 were set to 1.2 V/decade and 0.01 V/deg, respectively.

Equations 4-6 and 4-7 are valid for an impedance sensor with a uniform electrical-field distribution, and under the assumption that $R_c \gg |Z_p|$ and $\mathrm{Im}(Z_b) \ll R_c$. The latter requirement concerns the phase error, which was kept ultimately within 0.25 deg. Controlled measurements have shown that the polarization impedance does not exceed a few tens of ohms for a saline solution and is considerably smaller: a few ohms, when the sensor is in contact with blood. For an R_c resistor of 43 kΩ, neglecting the effect of Z_p in Eq. 4-6 yields a relative error of less than 0.3% for the measured Z_b.

The modulus of the impedance, which is derived after reversing Eq. 4-6, is used to calculate R_p, R_i, and C_m (Eq. 4-8 to Eq. 4-10). The Zhao method is applied [4.30], using the magnitudes $|Z_b(\omega_0)|$, $|Z_b(\omega_1)|$,

$|Z_b(\omega_2)|$ at frequencies $\omega_0 = 2\pi f_0$, $\omega_1 = 2\pi f_1$, and $\omega_2 = 2\pi f_2$, respectively, which yields:

$$R_p = \sqrt{K_0}\left|Z_b(\omega_0)\right| \tag{4-8}$$

$$R_i = \frac{R_p}{\sqrt{(K_0(K_1 - K_0 - F_1(1-K_0)))/(K_1 - K_0 - F_1K_1(1-K_0))} - 1} \tag{4-9}$$

$$C_m = \frac{1}{\omega_0\sqrt{(1-K_0)/(K_0R_i^2 - (R_p + R_i)^2)}} \ , \tag{4-10}$$

where:

$$F_1 = \left(\frac{\omega_1}{\omega_0}\right)^2 \tag{4-11}$$

$$F_2 = \left(\frac{\omega_2}{\omega_0}\right)^2 \tag{4-12}$$

$$K_1 = \left(\frac{\left|Z_b(\omega_1)\right|}{\left|Z_b(\omega_0)\right|}\right)^2 \tag{4-13}$$

$$K_2 = \left(\frac{\left|Z_b(\omega_2)\right|}{\left|Z_b(\omega_0)\right|}\right)^2 \tag{4-14}$$

$$K_0 = \frac{F_1K_2(1-K_1)(1-F_2) - F_2K_1(1-K_2)(1-F_1)}{F_1(1-K_1)(1-K_2F_2) - F_2(1-K_2)(1-K_1F_1)} \ . \tag{4-15}$$

The following three frequencies were selected for the calculation of the blood impedance components in the final HemoCard Vision design: f_0 = 20 kHz, f_1 = 600 kHz and f_2 = 1.2 MHz. The measurements conducted at 200 kHz and 400 kHz and the phase measurements were not used in this calculation. Nonetheless, these measurements were performed

in order to reconstruct and graphically present a more detailed, complex impedance plot.

The interface electronics apply an excitation current of 10 μA_{rms}, which is the maximum excitation current allowed by the EMC regulations for human use.

Extensive tests for *in vitro* blood characterization enabled the correlations to be found between the hematocrit and R_p, and between whole-blood viscosity and C_m, respectively (see Chapter 5). The tests show that for the HemoCard Vision catheter, the impedance sensor of which has a cell constant k of about 0.4 cm^{-1}, the interface electronics should be optimized to measure complex impedances in the range from 30 Ω to 120 Ω. Effectively, R_p varies from 40 Ω to 100 Ω, while C_m is found to be between 0.3 nF and 1.5 nF. The best resolution figures we could achieve in these ranges were ±0.2 Ω for R_p and ±25 pF for C_m. These resolution figures were obtained without averaging. As explained above, each of the five excitation-signal frequencies is applied for 8 ms. Therefore, it takes 40 ms to perform a single R_p, R_i and C_m measurement. The ECG is captured every 10 ms, while the temperature is measured every 40 ms. The ECG and temperature measurements are performed in parallel with the impedance measurements.

The *in vitro* blood-characterization tests show that an R_p resolution of ±0.2 Ω translates into a ±0.2% *Ht* resolution for the measured hematocrit, which is considered to be sufficient. The C_m resolution of ±25 pF translates into a ±1.73 mPa.s resolution for the measured viscosity. The latter figure is found to be too large when compared to the target specification of ±0.5 mPa.s. Therefore, it was concluded that the noise of the impedance channel needs to be lowered.

A detailed signal analysis identified the phase-gain analyzer AD8302 as the dominant noise source. For example, at the AD8302 magnitude output for an input-signal-level of -30 dBm, we measured a noise floor of 1140 $nV/\sqrt{Hz}$ (from 1 kHz to 10 kHz). According to the AD8302 datasheet, however, this figure should not exceed 350 $nV/\sqrt{Hz}$. Additionally, the AD8302 chip showed a pronounced spurious signal ripple at its magnitude output for input signals in the sub-50 kHz range. The AD8302 designers observed similar phenomena but could not offer a solution to prevent them from occurring.

Besides the poor C_m resolution figures, the first animal trials showed a a drop in the excitation current of few percent in the first few hours after the catheter was introduced. As explained above, the sensor electrodes

were not covered by the heparin coating. It has been found that after introducing the catheter into a living body, a thin fibrin layer develops over each separate electrode. The layer has an impedance that can reach several hundred ohms. It is obvious that similar to the electrode polarization impedance, this parasitic component cannot be compensated for and its influence over the measurement accuracy will remain uncontrolled unless the measurement principle involves measuring the current flowing through the sensor. This, in combination with the necessity to improve the C_m-resolution figures, led to the development of the second generation HemoCard Vision.

4.2.2 HemoCard Vision: second generation

Figure 4-16 shows the block diagram of the second generation HemoCard Vision. In this system, the phase-gain analyzer AD8302 has been replaced by two precision, OpAmp-based, full-wave rectifiers (amplitude detectors) [4.31]. The detectors are followed by two identical low-pass, third-order Bessel filters (F5, F6) with a corner frequency of 250 Hz and a 0.1% settling time of 4.6 ms. We have opted for the Bessel-type filters for F5 and F6 because they offer a good step response.

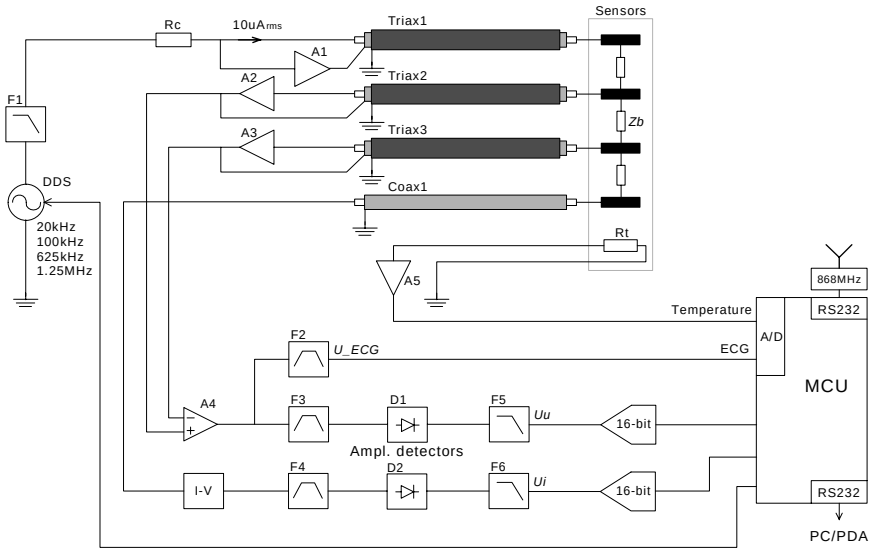

Figure 4-16: *Block diagram of the interface-electronics of the second generation HemoCard Vision.*

A current-to-voltage converter (I-V), known also as transimpedance amplifier, senses the current through the sensor. The filter F4 is identical to F3. This ensures a good match between the voltage and the current-measurement channels. Two matching 16-bit analog-to-digital converters digitize the voltages U_U and U_I, which are proportional to the amplitudes of the voltage over the measured impedance Z_b and the current flowing through it, respectively. Then $|Z_b(\omega)|$ is calculated as it follows:

$$\left|Z_b(\omega)\right| = \frac{G}{k}\frac{U_U}{U_I} \quad , \tag{4-16}$$

where G is a transimpedance conversion factor constant that accounts for the transfer factors in the voltage and the current channels. The cell constant of the sensor is denoted by k.

As the excitation current of the sensor is measured now, the fluctuations in the net current-path impedance no longer influence the total measurement accuracy.

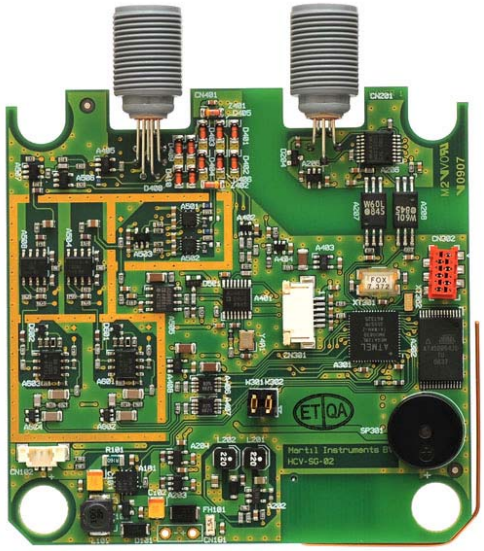

Figure 4-17: *Photograph of the interface-electronics board of the second generation HemoCard Vision.*

The new, second generation design, the implementation of which is shown in Fig 4-17, incorporates input buffers A2, A3 (ADA4817-1) and a

differential amplifier A4 (OPA846), which have slightly improved noise figures in comparison with the components used in the first generation design. The current-to-voltage converter is based on the use of the low-noise amplifier OPA820. As a result of this component selection and mainly as a result of eliminating the dominant noise source (the AD8302), the second generation device has reached the resolution figures of ±0.035 Ω for R_p and ±5.75 pF for C_m. These values correspond to a ±0.027% *Ht* resolution for the measured hematocrit, and to a ±0.39 mPa.s resolution for the measured viscosity, which now falls within the target specifications.

In terms of functionality, the second generation system has been improved by adding an extra measurement mode, in which the ECG sampling frequency is increased from 100 Hz to 1 kHz. The addition of a 868 MHz wireless link enables immediate data transfer to the external monitor.

4.3 Conclusions

An online hematology and cardiology diagnostic system has been designed which comprises of a central venous catheter, interface electronics, and interface software. The system, named HemoCard Vision, has been optimized to perform the electrical analysis of whole blood in the frequency range from 20 kHz to 1.2 MHz. Consequently, it has the potential to detect hematocrit and whole blood viscosity by measuring plasma resistance R_p and cell membrane capacitance C_m, respectively. The impedance sensor, which is positioned inside the right atrium, captures the intracavitary ECG as well. Additionally, the core body temperature is detected by a thermistor incorporated at the tip of the catheter.

The R_p and C_m measurements are synchronized with the detected ECG signal and are taken ideally at the end of diastole, just before the atrial contraction. At that moment the right atrium is completely filled with blood and the blood electrical properties being measured are least influenced by the proximity of the atrial wall. Furthermore, at this moment the flow in the atrium is low and hence the blood viscosity will be at its highest level.

With the existing three lumens for administering fluid infusions and/or measuring atrial pressure, the HemoCard Vision catheter features all the characteristic functionalities of a standard central venous catheter, along with impedance, ECG and temperature measurement capabilities.

4.4 References

4.1 Blagoy P. Iliev, Gheorghe A. M. Pop and Gerard C. M. Meijer, “In-vivo Blood Characterization System”, IMTC 2006 – Instrumentation and Measurement Technology Conference, Sorrento, Italy, 24-27 April 2006

4.2 A. B. Anderson, A. W. Dallmier, S. J. Chudzik, L. W. Duran, P. E. Guire, R. W. Hergenrother, M. A. Lodhi, A. E. Novak, R. F. Ostead, K. Wormuth, “Technologies for the surface modification of biomaterials”, In: Biomaterials in Orthopedics, Marcel Dekker, Inc, New York, NY, 2003, pp. 93-148

4.3 Yvette B.J. Aldenhoff, Menno L.W. Knetsch, Johannes H.L. Hanssen, Theo Lindhout, Simone J.H. Wielders, Leo H. Koole, “Coils and tubes releasing heparin. Studies on a new vascular graft prototype”, Biomaterials 25 (2004) 3125–3133

4.4 L. A. Geddes, R. Roeder, “Criteria for selection of materials for implanted electrodes”, Annals of Biomedical Engineering, Vol. 31. pp. 879-890, 2003

4.5 P. R. Rijnbeek, J. A. Kors, M. Witsenburg, “Minimum Bandwidth Requirements for Recording of Pediatric Electrocardiograms“, Circulation, 2001, Vol. 104; 25, pp. 3087-3090

4.6 Qiqiong Cui, Wei Zhang, Hu Wang, Xin Sun, Huanyi Yang, Xianqiang Meng, Yun Zhang, Hao Wang, “Left and right atrial size and the occurrence predictors in patients with paroxysmal atrial fibrillation“, International Journal of Cardiology, 130 (2008), pp. 69–71

4.7 Lee B. Baker, “Principles of the impedance technique”, IEEE Engineering in Medicine and Biology Magazine, March 1989, pp. 11-15

4.8 Christopher J. Yeung, Robert C. Susil, Ergin Atalar1, “RF Safety of Wires in Interventional MRI: Using a Safety Index”, Magnetic Resonance in Medicine, Vol. 47, 2002, pp. 187–193

4.9 Peter Vernickel, Volkmar Schulz, Steffen Weiss, Bernhard Gleich, “A Safe Transmission Line for MRI”, IEEE Transactions on Biomedical Engineering, Vol. 52, No. 6, June 2005

4.10 H. Fricke, S. Morse, “The electrical resistance and capacity of blood for frequencies between 800 and $4\frac{1}{2}$ million cycles”, The Journal of General Physiology 9, pp. 153-157, 1925

4.11 T. Chelidze, “Dielectric spectroscopy of blood”, Journal of Non-Crystalline Solids, Vol. 305, 2002, pp. 285-294

4.12 Jian-Zhong Bao, Christopher C. Davis, Mays L. Swicord, “Microwave dielectric measurements of erythrocyte suspensions”, Biophysical Journal, Vol. 66, June 1994, pp. 2173-2180

4.13 F. Jaspard, M. Nadi, A. Rouane, “Dielectric properties of blood: an investigation of haematoctrit dependence”, Physiol. Meas. Vol. 24, 2003, pp. 137-147

4.14 E. F. Treo, D. O. Cervantes, C. J. Felice, M. Tirado, M. E. Valentinuzzi, “Hematoctrit measurements by dielectric sprectroscopy”, Proceedings of the Second Joint EMBS/ BMES Conference, Huston, TX, USA, October 23-26, 2002, pp. 1750-1751

4.15 Yekta Ulgen, Mana Sezdi, “Hematoctrit dependence of the Cole-Cole parameters of human blood”, Proceedings od the 2^{nd} International Biomedical Engineering Days, 1998, pp. 71-74

4.16 Tuqiang Xie, Swee Chuan Tjin, Qingping Yang, Seng Lee Ng, “Effect of blood’s velocity on blood resistivity”, IEEE Transactions on Instrumentation and Measurement, Vol. 47, No. 5, October 1998, pp. 1197-1200

4.17 Jerzy Wtorek, Artur Polinski, “The contribution of blood-flow-induced conductivity changes to measured impedance”, IEEE Transactions on Biomedical Engineering, Vol. 52, No. 1, January 2005

4.18 A. E. Hoetink, Th. J. C. Faes, K. R. Visser, R. M. Heethaar, “On the flow dependency of the electrical conductivity of blood”, IEEE Transactions on Biomedical Engineering, Vol. 51, No. 7, July 2004

4.19 F. Jaspard, M. Nadi, “Dielectric properties of blood: an investigation of temperature dependence”, Physiol. Meas., Vol. 23, 2002, pp. 547-554

4.20 A. Pribush, D. Meyerstein, N. Meyerstein, “Study of red blood cell aggreagtion by admitance measurements”, Biorheology, Vol. 33, No. 2, 1996, pp. 139-151

4.21 Tian-Xian Zhao, Dieter Lockner, “Elelctrical impedance and erythrocyte sedimentation rate (ESR) of blood”, Biochimica et Biophysica Acta., Vol. 1153, 1993, pp. 243-248

4.22 Tian-Xian Zhao, B. Jacobson, “Quantitative correlation among fibrinogen concentration, sedimentation rate and electrical impedance of blood”, Medical & Biological Engineering & Computing, May 1997, pp. 181-185

4.23 Analog Devices, AD8302 LF-2.7 GHz, RF/IF Gain phase detector, datasheet

4.24 V. S. Reinhardt, “Spur Reduction Techniques in Direct Digital Synthesizers”, Proceedings of the 47th Frequency Control Symposium (IEEE/ERADCOM, Salt Lake City), 1993, pp. 230-241

4.25 A. C. Metting van Rijn, A. Peper, C. A. Grimbergen, “High-quality recording of bioelectric events. Part 2. Low-noise, low-power multichannel amplifier design”, Med Biol Eng Comput. 1991 Jul, 29(4), pp. 433-40

4.26 A. C. Metting van Rijn, A. Peper, C. A. Grimbergen, “High-quality recording of bioelectric events. Part 1. Interference reduction, theory and practice“, Med Biol Eng Comput. 1990 Sep, 28(5), pp. 389-97

4.27 E. M. Spinelli, F. Reverter, “On the stability of shield-driver circuits”, IEEE Transactions on Instrumentation and Measurement, Vol. 59, No. 2, February 2010, pp. 458-462

4.28 Desiderio Gross, “The duration of the T wave and its relation to the cardiac rate in healthy adults“, American Heart Journal, Vol. 47, Issue 4, April 1954, pp. 514-519

4.29 A. Ibanez, J. M. Ferrero Jr, “The ECG T-Wave Duration as an Index of Dispersion of Ventricular Repolarization Insights from Simula”, Computers in Cardiology 2006; 33, pp. 793-796

4.30 Tian-xian Zhao, Bertil Jacobson and Tommy Ribbe, “Triple-frequency method for measuring blood impedance”, Physiol. Meas., Vol. 14, 145-156, 1993, UK

4.31 National Semiconductor, Comlinear CLC418 Dual High-Speed, Low-Power Line Driver, datasheet, August 1996, Lit #150418-003

5 *Experimental results*

The HemoCard Vision blood analysis system described in Chapter 4 has been tested in a series of studies which include *in vitro* studies with human blood, animal *in vivo* studies in sheep, and a human *in vivo* pilot study in patients who underwent an autologous peripheral blood stem-cell transplantation.

The aim of the *in vitro* studies was to characterize the correlation between the blood electrical properties (plasma resistance R_p and cell membrane capacitance C_m) and those blood properties that strongly influence the rheological characteristics, i.e. hematocrit, viscosity, shear rate, acute-phase protein concentration, and temperature.

The main goals of the *in vivo* animal studies included optimization of the impedance sensor electrical-field distribution, especially for the moments when excessive heart rate occurs, and examination of the effectiveness of a range of biocompatibility-improving measures. These measures aimed to reduce the catheter surface imperfections and improve its hemocompatibility, e.g. by using special materials and overmolding techniques and coating the catheter with a drug-containing (heparin-based) adherent hydrophilic coating. The latter is an effective strategy to prevent the formation of thrombotic adhesions and, subsequently, the occurrence of emboli. Additionally, such coatings

greatly reduce the coefficient of friction between the catheter and the vessel wall, thus eliminating tissue irritation and damage.

The sensor electrical-field optimization and the biocompatibility-improving measures (see Chapter 4) resulted in first-hand practical experience when it comes to developing implantable catheter-based sensors. The sheep proved to be a good model for evaluating catheter biocompatibility and hemocompatibility. Unfortunately, the test animals demonstrated very low blood hematocrit and, hence, very low viscosity, especially the first few days after catheter introduction and the induced anaesthetization. Most of the time, the hematocrit did not exceed 30%. This resulted in viscosity levels that could not be detected reliably with the HemoCard Vision system, which is optimized to measure viscosity levels typical for human blood. The viscosity measurements, which were obtained with a Contraves LS30 as the reference instrument, show similar uncertainties, despite the fact that this instrument is able to perform the measurements under shear rates much lower that those existing in the right atrium. As a result of this, we could not derive measurements that would signify a substantial scientific achievement, therefore the animal studies will not be covered extensively in this book.

During the *in vivo* human pilot study, the HemoCard Vision system was used to monitor patients who underwent autologous peripheral blood stem-cell transplantation after receiving intensive chemotherapy and/or radiation therapy. Such patients have a significantly diminished immune system response, which makes them susceptible to inflammation and ultimately sepsis. In 10% of the cases, this leads to mortality. An early detection of inflammation with the HemoCard Vision may result in timely antibiotic treatment for high-risk patients, leading to decreased rates of morbidity and mortality.

5.1 *In vitro* blood analysis

The *in vitro* study aimed to investigate the behaviour of plasma resistance R_p and cell membrane capacitance C_m, with respect to the main blood rheological determinants, i.e. hematocrit (Ht), viscosity (η), shear rate (SR), acute-phase protein concentration and temperature. Ultimately, we aimed to derive the following correlations: $R_p=f(Ht)$ and $C_m=f(\eta)$.

The study included eight healthy volunteers with no history of infections in the weeks prior to the blood donation. Approximately 450 ml

blood was collected from each individual. It was then heparinized (25 IU/ml blood) and placed into a dedicated *in vitro* setup (Fig. 5-2), which allowed variation of the following blood parameters:

- Temperature in the range from 25°C to 37°C, divided into four steps.
- Hematocrit in the range from 30% to 50%, divided into four steps. The variation was induced by means of dilution with Voluven (Fresenius Kabi AG, Germany).
- Acute-phase protein (fibrinogen) concentration in the range from 2 g/l to 6 g/l, divided into four steps. The variation was induced by adding purified human fibrinogen. A dialysis of the fibrinogen was performed prior to the experiments for 24 hours in a 0.9% NaCl solution.
- Shear rate in the range from 0.24 s^{-1} to 1.95 s^{-1}, divided into ten steps. The variation was induced by means of blood flow variation.

The R_p and C_m were measured with the HemoCard Vision at each corresponding temperature, hematocrit and fibrinogen levels for the entire shear rate range in the order presented in the list above. At the same time, reference blood-viscosity measurements were performed in the same shear rate range using a Contraves LS30 rotational viscometer. A micro-capillary centrifuge served as the reference hematocrit meter.

Throughout the experiments, the activated clotting time (ACT) was monitored and kept above 300 s in order to avoid blood clotting. It has been found that blood clots rarely occur in an extracorporeal circuit when the ACT is longer than 300 s [5.1].

Erythrocyte sedimentation is an effect that should be monitored closely when performing *in vitro* blood analyses [5.2]. Even when blood is constantly circulating, sediments can form and alter the measurement results. To avoid this, prior to every R_p and C_m measurement we conducted, the blood was mixed for 5 s at the highest shear rate that could be achieved with the setup. It is important to note that one should not perform the anticipated measurement immediately after the shear rate has been restored to its intended level. The blood should be given time to settle and form the erythrocyte aggregates. The process of aggregation, as noted by our C_m measurements (Fig. 5-1), is governed by the term $1-e^{-t/\tau_a}$, where t is the time and τ_a is the aggregation time constant. Thus, the R_p and C_m measurements should be performed approximately in $4.61\,\tau_a$, if C_m is to reach at least 99% of its final value. Performing the

measurement later than this would invalidate the results since erythrocyte sedimentation–albeit much slower than aggregation–is already occurring and will continue to govern the C_m increase almost indefinitely [5.3]. This effect can be seen in Fig. 5-1: at $4.61\,\tau_a$, after the shear rate has been stepped, the C_m value appears to be lower than the calculated 99% of its final value.

Since τ_a depends on the hematocrit [5.4], and probably also on the fibrinogen concentration and temperature, it is more practical to use the criterion $\Delta C_m/\Delta t \approx Const$ (for $\Delta t = \tau_a$) to define the moment in time C_m is likely to be most accurately measured. When the term $\Delta C_m/\Delta t$ reaches a constant level, C_m will be mainly defined by the aggregation and only slightly influenced by the sedimentation [5.5].

The typical aggregation time constants τ_a we observed by applying the step shear rate changes approximate 7 s for a blood sample with a hematocrit of 43%, a fibrinogen concentration of 2.3 g/l, and a temperature of 37 °C. The shear rate was changed from 1.38 s^{-1} down to 0.24 s^{-1} and then back to 1.38 s^{-1}. The disaggregation time constant τ_{da} appears to be much shorter and was about 1.63 s for the blood sample we have depicted above.

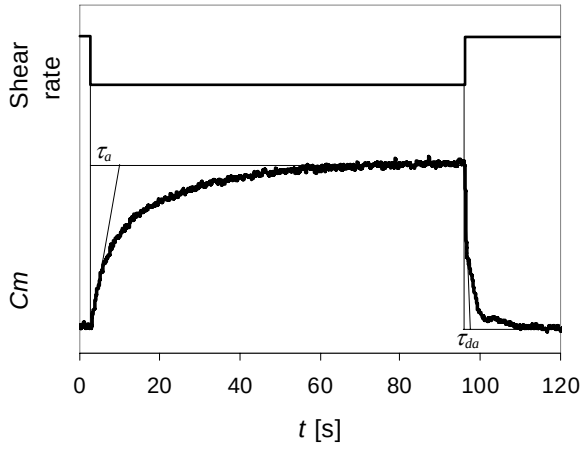

Figure 5-1: *The observed erythrocyte aggregation and disaggregation by means of C_m measurements for a shear rate step change.*

5.1.1 Experimental setup

Following the blood-flow considerations described in Chapter 2, we developed an *in vitro* blood-analysis setup. The setup, shown in Fig. 5-2, is optimised to work with flow rates between 0.1 l/min and 1 l/min, thus low shear conditions can be achieved. Such shear properties guarantee an apparent blood cell aggregation and correspond, at the same time, to the lowest shear conditions typical for the right atrium.

Figure 5-2: *In vitro setup for blood analysis.*

The *in vitro* setup consists of a main tube (on the left), where the catheter is inserted, a RotaFlow centrifugal pump (RFC 20-970 Console) with a built-in ultrasound flow meter (on the right), and a heat exchanger for temperature stabilization (on the back). The complete configuration has a volume of approximately 450 ml.

A detailed picture of the main tube can be seen in Fig. 5-3. Its special geometry-design complies with Eq. 2-8 and is set for an *Re* below 100; thus flow instabilities are reduced to a minimum. The cone, which is fixed against the inlet, prevents formation of a jet-like flow.

The shear conditions inside the setup must be well specified and controlled in order to correctly perform the electrical characterization of blood. In a separate experiment, the electrical field distribution around the

catheter was examined (Fig. 4-8, the 2 mm-2 mm-2 mm sensor). It covered the entire cross section of the setup, therefore the shear conditions around the sensor can be derived by simply calculating the mean shear stress and mean shear rate across the main tube. The mean shear stress is found from [5.6]:

$$\tau_{mean} = \frac{4\eta Q}{\pi R^3} \quad , \tag{5-1}$$

where R is the internal radius of the tube, and Q is the volumetric flow rate. The mean shear rate can then be calculated using Eq. 2-4:

$$\dot{\gamma}_{mean} = \frac{\tau}{\eta} = \frac{4Q}{\pi R^3} \quad . \tag{5-2}$$

Figure 5-3: *Main tube of the in vitro setup.*

Figure 5-4 shows the calculated shear rate (curve a) of the main tube without a built-in jet-flow-preventing cone as a function of the flow through the system. The jet-flow-preventing cone slightly alters the flow and shear profile conditions, which renders Eq. 5-2 almost invalid. An accurate shear rate estimation was then performed by using a Fluid Dynamics Analysis Package (FIDAP) simulations the results of which are depicted by curve “b” in Fig. 5-4.

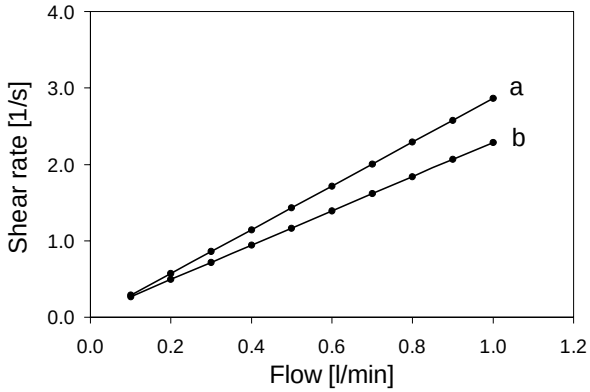

Figure 5-4: *Calculated (a) and simulated (b) mean shear rates across the in vitro setup main tube.*

5.1.2 Experimental results

Plasma-resistance characterization

Figure 5-5 shows the measured R_p versus *Ht* at different shear rates.

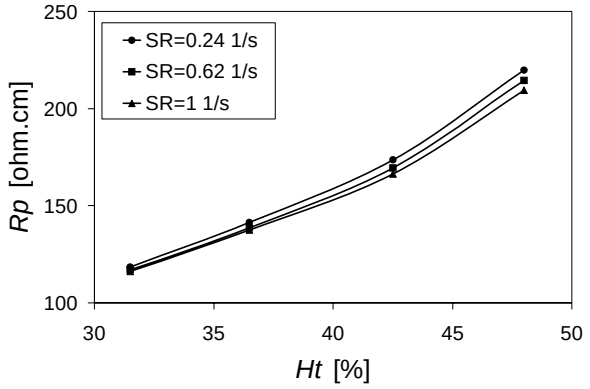

Figure 5-5: *R_p versus Ht measured at 37° C and at different shear rates.*

As expected, the plasma resistance R_p is a sensitive and accurate measure for the hematocrit. Slight variation, however, is observed at

different flow conditions due to the cell deformation when stress is applied. In addition, a cell orientation is provoked at higher shear/flow rates, which shortens the electrical current path [5.7].

The resistance R_p is strongly influenced by temperature, which is due to the temperature coefficient α_p of the specific plasma resistivity (Fig. 5-6). Our measurements show that α_p = -0.02 °C^{-1}, which is typical for mixtures with constituents similar to a saline solution. This temperature coefficient is only expected at frequencies in the kHz range or lower, where conduction can be considered to be purely ionic. At higher frequencies, a new conduction phenomenon appears which are bound to the dipolar losses of water molecules [5.8]. The two conductivities add to each other but do not react in the same manner to an increase in temperature. Even though the ionic conductivity increases, the conductivity due to the dipolar losses of water molecules decreases. At frequencies in the GHz range, the conductive characteristics are hardly caused by ionic phenomena and the variation coefficient may even become negative. Fortunately, our measurements were performed at relatively low frequencies and from our observations, α_p remains constant in the frequency range between 20 kHz and 1.2 MHz.

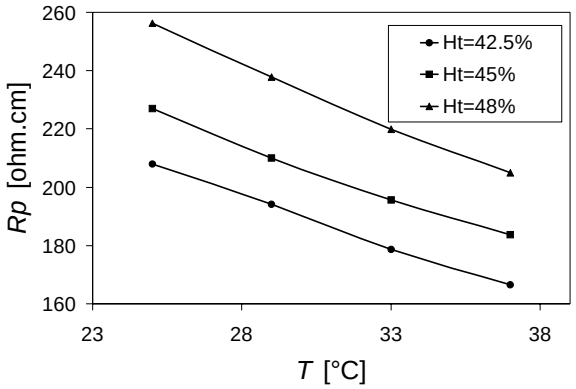

Figure 5-6: *R_p versus T measured at a shear rate of 1 s^{-1}.*

An elevated acute-phase protein level results in a slight increase in R_p (Fig. 5-7). With its large molecules, fibrinogen apparently contributes to the cellular phase of whole blood and limits the electrical current path at low frequencies. The current path is additionally influenced by the bigger erythrocyte aggregates formed at higher fibrinogen concentrations [5.9].

Nevertheless, the cumulative effect of fibrinogen concentration on R_p is negligible, as is the shear rate influence. Therefore, these two will not be taken into account in the $R_p=f(Ht)$ correlation.

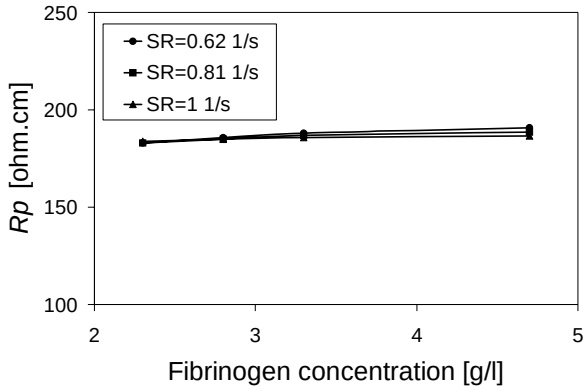

Figure 5-7: *R_p versus fibrinogen level measured at an Ht of 45%, a temperature of 37°C, and at different shear rates.*

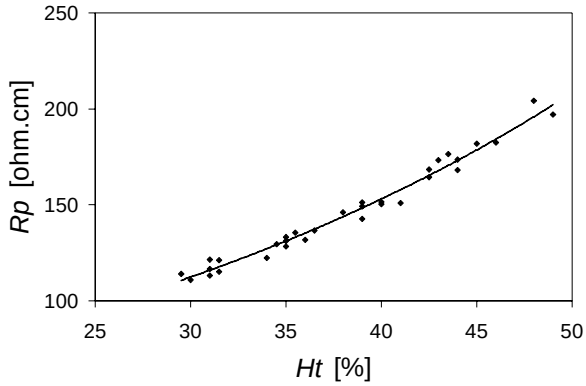

Figure 5-8: *R_p versus Ht and the least-squares fit curve (R^2 = 0.98, $\sigma = \pm 3.7\ \Omega.cm$). The measurements were conducted at 37°C.*

Figure 5-8 shows the measured R_p versus *Ht*. The graph includes data from all eight *in vitro* experiments. After applying a least-squares curve fitting, we found the following correlation between R_p and *Ht*:

$$R_p = \rho_p(1+\alpha_p(T_p - T_{ref}))\,\mathrm{e}^{C_e Ht} \quad , \tag{5-3}$$

where R_p is the plasma resistance in [Ω.cm], $\rho_p = 40.368$ Ω.cm is the specific plasma resistance at 37 °C, $\alpha_p = -0.02$ °C^{-1} is the temperature coefficient. The hematocrit *Ht* is presented as a volume fraction, T_p is patient's temperature in [°C], $T_{ref} = 37$ °C is the reference temperature, and $C_e = 3.3$ is the red blood cell form-factor constant, which is derived experimentally. Hence, the HemoCard Vision can be used to measure *Ht* by applying:

$$Ht = \frac{1}{C_e}\ln\left(\frac{R_p}{\rho_p(1+\alpha_p(T_p - T_{ref}))}\right) \quad . \tag{5-4}$$

For a limited *Ht* range, an exponential R_p=*f*(*Ht*) correlation is known to offer better curve fitting than the Maxwell-Fricke equation (Eq. 3-13) [5.10]. Equation 5-4 is found to be in good agreement, i.e. within ±1% *Ht,* with the results we obtained from measuring the hematocrit with a micro-capillary centrifuge. However, the measurement error is larger for the patients who underwent acute hemodilution therapy, which is due to the specific conductivity variation among the typical plasma expanders [5.11]. Table 5-1 shows the specific conductivity and the corresponding temperature coefficient we measured for Voluven (Fresenius Kabi AG, Germany), Gelofusine (B. Braun Melsungen AG, Germany) and Plegisol (Abbott Laboratories, USA).

Table 5-1. *The measured specific conductivity and its temperature coefficient for typical plasma expanders.*

	Conductivity at 25 °C [mS.cm^{-1}]	Temperature coefficient [°C^{-1}]
Voluven	13.54	0.023
Gelofusine	12.64	0.022
Plegisol	16.37	0.021

Cell-membrane-capacitance characterization

As described in Chapter 2, whole blood viscosity strongly depends on the hematocrit, the acute-phase protein concentration, the shear properties, and to a lesser degree on the temperature. While blood-plasma viscosity is relatively low, the high-viscous, non-Newtonian properties of blood appear in the presence of packed cell and rise exponentially with the *Ht*. Furthermore, the formation of red cell aggregates (rouleaux), the formation of which is governed by the acute-phase protein concentration, the shear properties, and the temperature, elevates the apparent whole blood viscosity even further.

The equivalent bulk capacitance of a simplified two-phase blood suspension is expressed by Eq. 3-17. This model involves the packed cell volume (*n* and *Ht*), as well as the state of the suspended particles (*N*). Hence, the bulk capacitance, as well as the cell membrane capacitance (see Eq. 3-22) of such a two-phase suspension, are expected to closely follow the viscosity of the suspension.

Figure 5-9 shows the measured C_m versus *Ht* at 37°C and different shear rates. Hematocrit, being the main determinant of whole blood viscosity, affects C_m in a way similar to how it affects viscosity (Fig. 2-7), though not in such a strong exponentially increasing form [5.12].

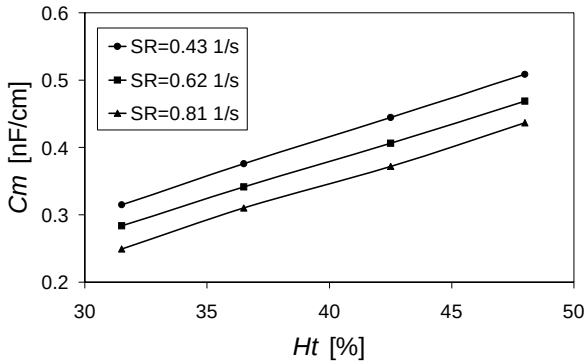

Figure 5-9: *C_m versus Ht measured at 37° C and at different shear rates.*

In electrical terms, the number of cells in a suspension is equivalent to the number of capacitors in a network (Eq. 3-17). A larger number of capacitors results in a higher bulk capacitance and vice versa. Nevertheless, the way the capacitors are arranged should also be taken

into account. The total bulk capacitance will increase or decrease when the capacitors are connected in parallel or in series, respectively. This effect can directly be associated with the red blood cell aggregation. When the aggregates are formed, the "capacitors" (cells) create predominantly parallel connections. Then, the bulk capacitance will increase. On the contrary, an increase in the shear rate results in more dispersed and randomly oriented cells, which leads to a lower bulk capacitance for the same *Ht* (Fig. 5-10).

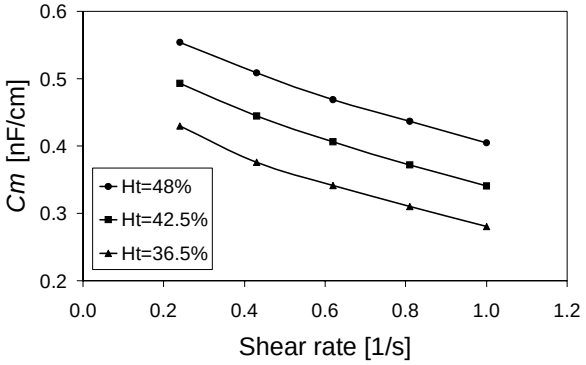

Figure 5-10: *C_m versus shear rate measured at 37° C and different hematocrits.*

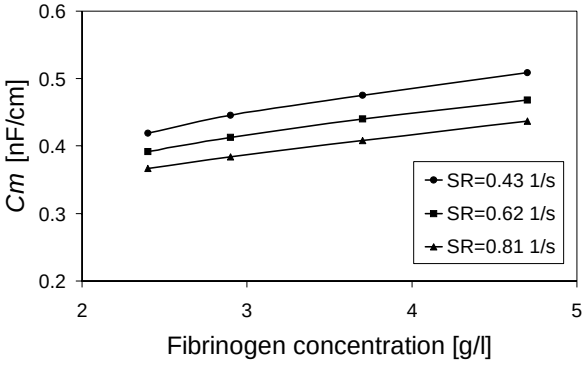

Figure 5-11: *C_m versus fibrinogen level measured at 37° C, an Ht of 48% and different shear rates.*

Red cell aggregation is the prime factor in whole blood viscosity. It is a reversible process caused by large proteins, e.g. fibrinogen or immunoglobulins, by bridging between the cells. Being involved in the interaction between the cells and altering the aggregation process, these proteins have a direct effect on the measured C_m (Fig. 5-11) [5.12, 5.13] and on the measured blood viscosity (Fig. 2-9). However, this influence is less pronounced than the corresponding *Ht* and shear-rate induced changes.

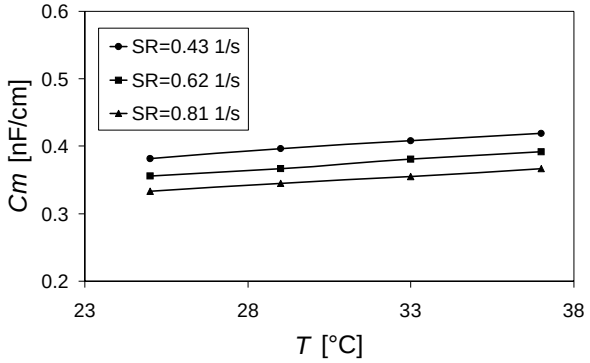

Figure 5-12: *C_m versus temperature measured at an Ht of 48% and at different shear rates.*

Although quite insensible, temperature also influences whole blood viscosity (Fig. 2-10). A decrease in temperature induces a higher viscosity for several reasons. It causes an increase in adsorptive energy of red cell aggregation due to a stronger molecular adsorption stress and weaker electrostatic repulsion. Additionally, red blood cell deformability is impaired when lowering the temperature, which creates a larger contact area between aggregating cells. Another factor is the plasma protein adsorption, which is an exothermic process that is stronger at lower temperatures and associated with the formation of rouleaux. With all that being said, it is expected that the temperature should affect C_m in the way it affects the red blood cell aggregation. For example, C_m should decrease at higher temperatures and vice versa. However, as shown in Fig. 5-12, C_m exhibits exactly the opposite trend. It has been found that the C_m decrease resulting from a lesser aggregation at higher temperatures, is counteracted by a marked rise in the specific cell membrane capacitance C_{0m}. This is due to a transition phenomenon occurring at the erythrocyte-membrane

phospholipid bilayer, which phenomenon peaks at 37°C where C_{0m} is at its maximum [5.14, 5.15].

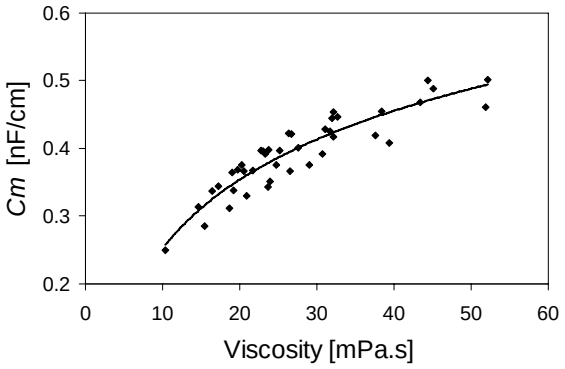

Figure 5-13: *C_m versus whole blood viscosity and the least-squares fit curve (R^2 = 0.85, σ = ±0.022 nF.cm^{-1}).*

Irrespective of the reasons for blood-viscosity changes, our ultimate goal is to find a simplified $C_m=f(\eta)$ correlation. Figure 5-13 shows the measured C_m versus whole blood viscosity including data from the eight *in vitro* experiments. The measurements were performed at a constant temperature of 37°C. The *Ht* ranged from 42.5% to 49%. The fibrinogen concentration was between 1.8 g/l and 2.8 g/l, while the shear rate was varied from 0.24 s^{-1} to 1 s^{-1}.

A least-squares curve fitting resulted in the following correlations:

$$C_m = \alpha \ln \frac{\eta}{\eta_0} + \beta \tag{5-5}$$

$$\eta = \eta_0 \, e^{\frac{1}{\alpha}(C_m - \beta)} \quad , \tag{5-6}$$

where $\alpha = 0.1544$ nF.cm^{-1}, $\beta = -0.1025$ nF.cm^{-1}, and $\eta_0 = 1$ mPa.s are constants.

Failing to perform a more precise C_m versus T characterization prevent us from compensating Eq. 5-5 and Eq. 5-6 for the temperature variations. Yet, Eq. 5-6 has been found to be in good agreement, i.e. within ±3 mPa.s, with the results we have obtained when measuring the

viscosity with the Contraves LS30 in the temperature range from 36°C to 38°C.

5.2 *In vivo* blood analysis

5.2.1 Clinical background

The HemoCard Vision system was used in an *in vivo* human pilot study to monitor the inflammation in recipients of a peripheral blood hematopoietic stem-cell transplant (PBHSCT) after myeloablative therapy. This therapy consists of an intensive chemotherapy alone or in combination with a radiation therapy. In this patient group, inflammation occurs due to mucosal barrier injury (MBI). This is an inevitable side-effect of the conditioning regimens used for hematopoietic stem-cell transplantation and is primarily the result of toxicity [5.16]. An MBI is known to appear around a week after starting myeloablative therapy and worsens until a peak is reached. Under normal circumstances, the intact mucosa forms the first defence against systemic infections and plays an active role in the crucial balance between the host and the environment. Damaged mucosa creates a nidus for infection, which is the leading cause of morbidity and mortality. Given the inability of immunocompromised hosts to mount an adequate inflammatory response, the classic signs and symptoms of infection in hematopoietic stem-cell transplant recipients, other than fever, may be minimal or even absent [5.17].

Normally, all PBHSCT recipients have a long-term venous catheter, which enables ready-access for administering high-dose chemotherapy, other drugs, blood products and total parenteral nutrition, as well allowing blood to be obtained for laboratory investigation and for cultures. After hospital admission, a standard triple or quadruple lumen catheter is inserted under local anaesthesia into the left or right subclavian vein (Fig. 5-14) using the Seldinger technique. This device remains in place during the entire hospital stay. In this study, the HemoCard Vision catheter was used instead of a standard catheter. Coupled to its electronics, it offers a continuous monitoring of core body temperature, hematocrit (Eq. 5-4), whole blood viscosity (Eq. 5-6), and heart rate. It is expected that the combination of all four parameters will help to predict the development of inflammation and provide critical data used for rapid decisions with respect to the optimal moment to start empirical antibiotic therapy [5.18]. The results obtained using the HemoCard Vision were compared with the

results obtained by the standard management of the PBHSCT recipients. Currently, this management consists of a daily physical examination and observation of every subtle sign or symptom of infection by conducting axillary temperature measurements five times daily, as well as monitoring heart rate and blood pressure.

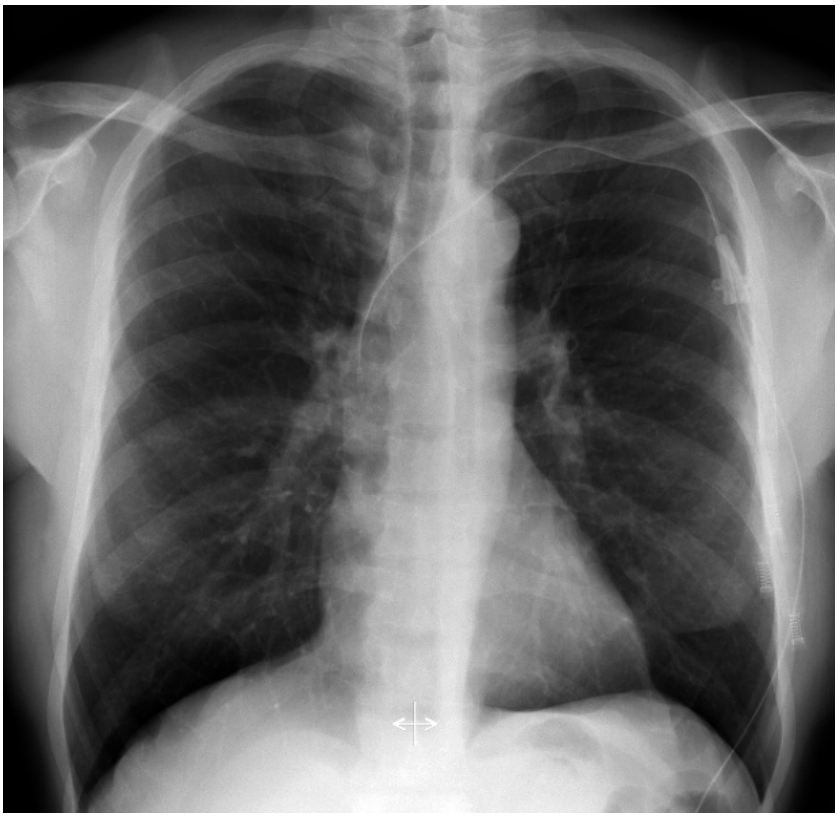

Figure 5-14: *X-ray showing an implanted HemoCard Vision catheter. The tip of the catheter is located in the upper part of the right atrium.*

5.2.2 Experimental results

Six patients were included in the *in vivo* human pilot study. One of the patients developed mild sepsis, which was detected using the viscosity-measurement capabilities of the HemoCard Vision and Contraves LS30 (Fig. 5-15).

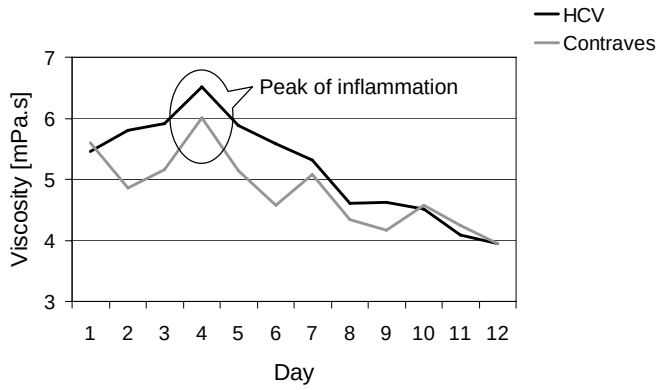

Figure 5-15: *Whole blood viscosity measured in vivo with the HemoCard Vision and in vitro with the Contraves LS30 at a shear rate of 4.04 s^{-1}.*

As seen in Fig. 5-15, the rise in viscosity coincided with the increase in the inflammatory proteins fibrinogen and C-reactive protein (CRP) (Fig. 5-16).

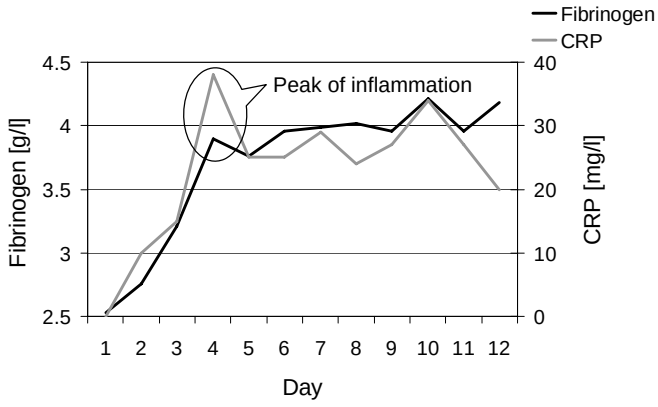

Figure 5-16: *Increase in the inflammatory proteins fibrinogen and CRP as a result of inflammation.*

The rise in core body temperature measured by the HemoCard Vision appeared several hours earlier than the temperature detected by the

axillary thermometer (Fig. 5-17). Figure 5-17 also depicts the heart rate extracted from the HemoCard Vision ECG measurements. Both, the heart rate and temperature appear to advance and increase earlier than the increase in the inflammatory proteins and subsequent increase in whole blood viscosity.

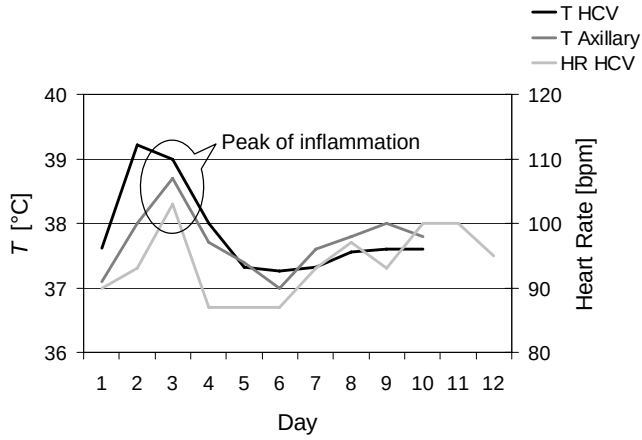

Figure 5-17: *Core body temperature and heart rate as measured with the HemoCard Vision in comparison with the axillary temperature.*

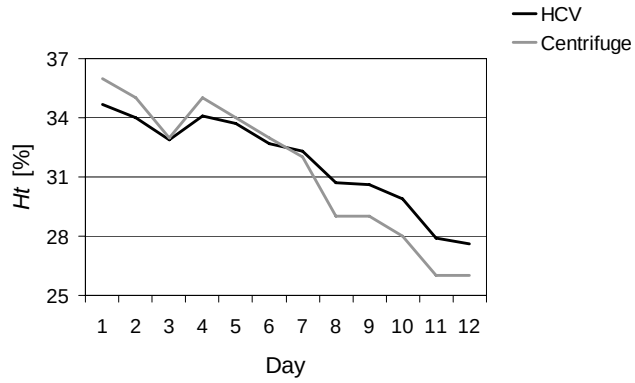

Figure 5-18: *Hematocrit measured in vivo with the HemoCard Vision and in vitro with a micro-capillary centrifuge.*

As inflammation persists, anemia appears (Fig. 5-18). Lowering of the hematocrit is a physiological response of the organism to the increased blood viscosity, which acts to counterbalance the presence of the inflammatory protein overload. Lowering blood viscosity by decreasing the hematocrit improves tissue perfusion, especially in microcirculation.

It can be concluded that the parameters measured by the HemoCard Vision can be used to detect inflammation. Nevertheless, determining the exact combination of parameters and their critical threshold levels for the optimal moment to start antibiotic therapy, requires a wider patient population study to be conducted.

Finally, as shown in Fig. 5-15 and Fig. 5-18, whereas hematocrit decreases from 34% on day 4 to 28% on day 12 (a decrease of about 18%), the blood viscosity at the same time decreases from 6.6 mPa.s to 4 mPa.s (a decrease of about 40%). This means that although normally the hematocrit accounts for almost 90% of the total whole blood viscosity level, during inflammation–which involves increased levels of acute-phase proteins–the influence of these proteins on blood viscosity becomes significantly greater. Apparently, such a considerable inflammatory-protein influence can only be counteracted by lowering the hematocrit. The way these processes reflect on the tissue perfusion, which can be associated with Q in the law of Hagen-Poiseuille (Eq. 2-11), can directly be linked to the blood viscosity variations, i.e. a 40% increase in blood viscosity will equally diminish the tissue perfusion by 40%. Therefore, it can also be concluded that the HemoCard Vision might be useful in estimating and improving tissue perfusion by guiding the hemodilution therapy in intensive care settings, where blood viscosity has been recognized in recent clinical studies as being an important factor in the microcirculation of different tissues [5.19-5.21].

5.3 Conclusions

From a series of dedicated *in vitro* studies, the correlation between the electrical and the rheological properties of blood has been found. This correlation concerns plasma resistance R_p and cell membrane capacitance C_m on the one hand, and hematocrit, viscosity, shear rate, acute-phase protein concentration and temperature on the other. It has been found that R_p can be a very accurate measure for the hematocrit, provided that the temperature coefficient of the specific blood-plasma resistance is taken into account. At the same time, C_m correlates well with the whole blood

viscosity measured in the temperature range from 35°C to 39°C. In a wider temperature range, there is a transition phenomenon occurring at the erythrocyte-membrane phospholipid bilayer which alters the specific membrane capacitance: this effect needs additional data to be collected before it can be fully understood and compensated for.

With its abilities to continuously monitor core body temperature, heart rate, hematocrit and whole blood viscosity, the HemoCard Vision system was successfully used in a limited *in vivo* human pilot study where it monitored peripheral blood hematopoietic stem-cell transplant (HSCT) recipients after myeloablative therapy. It has been shown that it is possible to measure core temperature, heart rate, blood viscosity and hematocrit reliably and continuously *in vivo* in awake patients by using a specially designed catheter. This can lead to timely institution of therapy with the prospect of improving the outcome by preventing the development of life-threatening, infectious complications, and by reliably detecting inflammation in general, since whole blood viscosity reflects the inflammatory level in blood.

5.4 References

5.1 B. S. Bull, R. A. Korpman, W. M. Huse, B. D. Briggs, “Heparin therapy during extracorporeal circulation. I. Problems inherent in existing heparin protocols”, J Thorac Cardiovasc Surg, 1975, Vol. 69, pp. 674–684

5.2 Tian-Xian Zhao, D. Lockner, “Electrical impedance and erythrocyte sedimentation rate (ESR) of blood”, Biochim Biophys Acta., 1993 Dec 12; 1153(2):243-248

5.3 W. T. Hung, A. F. Collings, J.Low, “Erythrocyte sedimentation rate studies in whole human blood”, Phys Med Biol. 1994 Nov; 39(11):1855-1873

5.4 V. Musumeci, G. Cremona, S. Baroni, A. Bisbano, F. Tutinelli, C. Zuppi, “Inhibitory interference of red cells in the measurement of whole blood platelet aggregation by the impedance method”, Thromb Res. 1987 Jan 1; 45(1):95-100

5.5 A. Pribush, D. Meyerstein, N. Meyerstein, “Study of red blood cell aggregation by admittance measurements”, Biorheology. 1996 Mar-Apr; 33(2):139-151

5.6 F. M. White, “Viscous fluid flow, Third edition”, McGraw-Hill International Edition, ISBN: 0390547743

5.7 A. E. Hoetink, Th. J. C. Faes, K. R. Visser, and R. M. Heethaar, "On the Flow Dependency of the Electrical Conductivity of Blood", IEEE Transactions on biomedical engineering, Vol. 51, No. 7, JULY 2004, pp. 1251-1261

5.8 F. Jaspard, M. Nadi, "Dielectric properties of blood: an investigation of temperature dependence", Physiol. Meas. 23 (2002), pp. 547–554

5.9 Tian-Xian Zhao, B. Jacobson, "Quantitative correlations among fibrinogen concentration, sedimentation rate and electrical impedance of blood", Med Biol Eng Comput. 1997 May; 35(3):181-185

5.10 L. A. Geddes, C. Sadler, "The specific resistance of blood at body temperature", Med Biol Eng. 1973 May;11(3):336-339

5.11 J. Steinfelder-Visscher, P. W. Weerwind, S. Teerenstra, G. A. Pop, R. M. Brouwer, "Conductivity-based hematocrit measurement during cardiopulmonary bypass", J Clin Monit Comput. 2007 Feb;21(1):7-12. Epub 2006 Nov 4

5.12 Tian-Xian Zhao, "Contributions of suspending medium to electrical impedance of blood", Biochimica et Biophysica Acta, 1291, 1994, pp. 179-185

5.13 L. Mannucci, R. Redaelli, E. Tremoli, "Effects of aggregating agents and of blood cells on the aggregation of whole blood by impedance technique", Thromb Res., 1988, Oct 15; 52(2):143-151

5.14 J. Z. Bao, C. C. Davis, R. E. Schmukler, "Frequency domain impedance measurements of erythrocytes. Constant phase angle impedance characteristics and a phase transition", Biophys J. 1992 May; 61(5):1427–1434

5.15 T. Chelidze, "Dielectric spectroscopy of blood", Journal of Non-Crystalline Solids, Volume 305, Issues 1-3, July 2002, pp. 285-294

5.16 N. M. A. Blijlevens, J. P. Donnelly and B. E. De Pauw, "Mucosal barrier injury: biology, pathology, clinical counterparts and consequences of intensive treatment for haematological malignancy: an overview", Bone Marrow Transplantation, June 2000, Volume 25(12), pp. 1269-1278

5.17 J. P. Donnelly, B. E. de Pauw, “Diagnosis and treatment of infection in the uimmunocompromised host”, Current opinions in infectious diseases, Volume 5, Issue 3, June 1992, pp. 415-421

5.18 L. S. Elting, E. B. Rubenstein, K. Rolston, S. B. Cantor, C. G. Martin, D. Kurtin, S. Rodriguez, T. Lam, K. Kanesan, G. Bodey, “Time to clinical response: an outcome of antibiotic therapy of febrile neutropenia with implications for quality and cost of care”, Journal of Clinical Oncology, November 1, 2000, Volume 18, pp. 3699-706

5.19 A. G. Tsai, P. Cabrales, M. Intaglietta, “Blood viscosity: a factor in tissue survival?”, Crit Care Med., July 2005, Volume 33(7), pp. 1662-3

5.20 A. Cortinovis, A. Crippa, R. Cavalli, M. Corti, L. Cattaneo, “Capillary blood viscosity in microcirculation”, Clinical Hemorheology and Microcirculation, July 2006, Volume 35(1-2), pp. 183-92

5.21 H. H. Lipowsky, “Microvascular rheology and hemodynamics”, Microcirculation, Jan-Feb 2005, Volume 12(1), pp. 5-15

6 *Conclusions and suggestions for future work*

6.1 Conclusions

This thesis has focused on the development of an online *in vivo* hematology and cardiology diagnostic system, named HemoCard Vision, which consists of a central venous catheter, interface electronics, and data processing software. The tip of the catheter incorporates a thermistor and a four-electrode impedance sensor used for both detecting the intracardiac ECG and performing the electrical analysis of blood inside the right atrium. The electrical parameters measured in blood are plasma resistance R_p and cell membrane capacitance C_m. These parameters are used to calculate the hematocrit and whole blood viscosity. The main achievement of this system is the ability to monitor *in vivo* blood rheological properties and especially whole blood viscosity.

The basic concepts and clinical aspects of blood analysis were described in Chapter 2. Blood rheology and particularly whole blood viscosity depends largely upon the packed cell volume, which is dominated by the volume of erythrocytes (red blood cells). Thus, the hematocrit, i.e. the red blood cell volume fraction, is seen as the main determinant of whole blood viscosity. A linear increase in hematocrit leads to an exponential rise in blood viscosity.

Red-cell aggregation is the prime factor in whole blood viscosity at low shear rate. It is a reversible process caused by large proteins such as fibrinogen and immunoglobulins, by bridging between the cells.

Red blood cell deformability plays an important role in blood rheology too. It is defined by the mechanical properties of the cell membrane and the cell-content viscosity. In microcirculation, red-cell deformability and plasma viscosity are the main determinants of resistance to flow.

When blood flows through a vessel, it splits into layers with different velocities, due to the high cellular content. The quantitative measure of this effect is called the shear rate. The frictional force between two adjacent layers is directly proportional to the shear rate and to the internal frictional property of the fluid, i.e. its viscosity. This interaction causes the non-Newtonian characteristics of blood, of which viscosity is not constant but changes with the liquid shear properties.

In the pathophysiology of vascular diseases, blood viscosity is a major factor with implications in cardiovascular hemodynamics and tissue perfusion. An elevated blood viscosity also increases thromboembolic risk and can be correlated with systemic inflammatory activities.

Performing an electrical analysis of blood, which was discussed in Chapter 3, opens up the opportunity to derive a number of blood rheological properties. Among them, hematocrit and whole blood viscosity can be found.

Complex-impedance measurement techniques demonstrate significant potential for analysing physiological phenomena and for recording bioelectrical events. When an impedance-measurement sensor comes into contact with a tissue or an aqueous solution and an excitation signal is applied, conduction and polarization mechanisms occur. Blood behaves similarly to a complex biological tissue, thus its electrical properties involve identical conduction and polarization mechanisms. In general, the equivalent electrical model of whole blood consists of three main components: plasma resistance R_p, cell membrane capacitance C_m and cell interior resistance R_i. The R_p component represents the specific plasma resistance affected by the amount and orientation of cells in it. The resultant bulk cell-membrane capacitance is represented by C_m, while R_i reflects the equivalent intracellular resistance.

Electrodes used for impedance measurements exhibit DC offset potentials and polarization impedance, both of which can cause significant measurement errors. The offset potentials are frequently unstable and

result in drift and noise. The polarization impedance, at the same time, can cause a voltage drop on each sensor electrode due to either the excitation or sensing currents coupled to the interface electronics.

The above-listed considerations have become the basis for the HemoCard Vision system development described in Chapter 4. The system is optimized to perform electrical analysis of whole blood in the frequency range from 20 kHz to 1.2 MHz. It incorporates a four-electrode impedance sensor and a high input-impedance differential amplifier to counteract the influence of the low-frequency polarization mechanisms occurring at the electrode surface. The system has the potential of detecting hematocrit and whole blood viscosity by measuring plasma resistance R_p and cell membrane capacitance C_m, respectively. The impedance sensor, which is positioned inside the right atrium, captures the intracardiac ECG as well. Additionally, the core body temperature is detected by a thermistor incorporated in the tip of the catheter.

The R_p and C_m measurements are synchronized with the detected ECG signal and are taken ideally at the end of diastole, just before the atrial contraction. At that moment the right atrium is completely filled with blood and the measured blood electrical properties are least influenced by the proximity of the atrial wall. Furthermore, at this moment the flow in the atrium is low and hence the blood viscosity will be at its highest level.

With the existing three lumens for administering fluid infusions and/or measuring atrial pressure, the HemoCard Vision catheter has been designed such that it features all the characteristic functionalities of a standard central venous catheter together with the impedance, intracardiac ECG, and temperature measurement capabilities.

A series of dedicated *in vitro* and *in vivo* studies were conducted with the newly designed system, the outcomes of which are shown in Chapter 5. The *in vitro* studies resulted in correlating the blood electrical properties, plasma resistance R_p and cell membrane capacitance C_m, with the corresponding blood rheological properties. It has been found that when the temperature coefficient of the specific plasma resistance is considered appropriately, R_p can be a very accurate measure for the hematocrit. At the same time, C_m correlates well with the measured whole blood viscosity in the temperature range from 35°C to 39°C. In a wider temperature range, a transition phenomenon occurring at the erythrocyte-membrane phospholipid bilayer alters the specific membrane

capacitance. For better understanding of this effect more experimental research must be performed.

The HemoCard Vision system has been successfully used in a limited *in vivo* human pilot-study where it monitored peripheral blood hematopoietic stem cell transplant (HSCT) recipients after myeloablative therapy. It has been shown that it is possible to measure core body temperature, heart rate, blood viscosity and hematocrit reliably and continuously *in vivo* in awake patients. This can lead to a timely institution of therapy with the prospect of improving the outcome by preventing the development of life-threatening, infectious complications and by reliably detecting inflammation, since whole blood viscosity reflects the inflammatory level in blood.

Besides the HSCT recipients, other patient groups that are managed with a central venous catheter could also benefit from this innovation. These groups include patients in the intensive care (after major surgery or after out-of-hospital cardiac arrest), immunocompromised patients, and patients with malignancies.

6.2 Suggestions for future work

There are a number of areas, in which the HemoCard Vision system can and should be improved before it becomes a truly reliable monitoring device. The most critical areas include impedance sensor positioning, optimization of data-processing algorithms, and temperature characterization of the cell-membrane capacitance over a wider temperature range. In addition, measurement results obtained in a wider patient population are needed in order to find the optimal hematocrit and whole blood viscosity levels. This will allow the measurement system to turn into a tool that will guide the therapeutic decisions of clinicians.

6.2.1 Electrical field and positioning optimization of the sensor

As described in Chapter 4, the impedance sensor has been designed such that its electrical field optimally covers the right atrium. The tip of the catheter has been bent in order to match the angle between the superior vena cava and the right atrium. The sensor position, in terms of right atrium depth, is guided and accurately fixed with the help of the detected ECG signal. Despite taking all these measures, the sensor-section of the catheter frequently tends to come close or even touch the atrial wall. Then,

the measured impedance becomes distorted, as do the measured hematocrit and viscosity. These moments are also clearly indicated by the ECG, for which the amplitude becomes notably higher than the what is typical for a well-positioned sensor. The measurement results that are affected by the atrial wall can easily be recognized and discarded. Nevertheless, the catheter needs further development to make way for a sensor design that would prevent the tendency of the sensor to touch the atrial wall. Using a balloon that pushes the sensor away from the atrial wall is one feasible option. The balloon would have to be inflated only when measurements are conducted.

6.2.2 Data-processing algorithm optimization

When triggering the impedance measurements on the intracavitary ECG signals, the impedance samples should ideally be taken at the end of diastole, just before the atrial contraction. At that moment, the right atrium is completely filled with blood and the impedance signal is least influenced by the proximity of the atrial wall. Unfortunately, the T-wave has a very low amplitude and cannot be detected easily. As an option, one may detect the P-wave and with the help of the P-P interval calculate the exact moment in time when the impedance should be recorded. A P-wave recorded by a sensor that floats inside the right atrium, demonstrates a significant amplitude variation. An improved data processing algorithm that is able to cope with such an amplitude variation and that offers a more accurate P-wave detection, may result in a notable increase in the impedance-measurement accuracy.

6.2.3 Temperature dependence of cell membrane capacitance

The *in vitro* characterization of the cell-membrane-capacitance versus blood-viscosity (see Chapter 5), has revealed slightly unexpected temperature dependence. For example, a higher temperature should result in a lower blood viscosity and hence, in a lower C_m, given that all other parameters are constant. However, it has been found that for temperatures lower than 37°C the C_m increases instead. This is due to a transition phenomenon occurring at the erythrocyte-membrane phospholipid bilayer, which phenomenon alters the specific cell membrane capacitance. Various literature sources have described similar effects and have shown that these effects have an optimum at exactly 37°C. Additional C_m versus whole blood viscosity measurements, in a wider temperature range, are needed in

order to fully understand the behaviour of C_m and to compensate for its temperature dependence in the final blood-viscosity calculation.

Summary

This thesis is focused on the development of an online *in vivo* hematology and cardiology diagnostic system, called HemoCard Vision, which consists of a central venous catheter, interface electronics and data processing software. As a result of direct measurement and/or additional data post-processing, the system derives core body temperature, intracardiac ECG, hematocrit, and whole blood viscosity. The main achievement of this work is the ability of the system to monitor *in vivo* blood rheological properties and especially whole blood viscosity.

Chapter 2 depicts the basic concepts and clinical aspects of blood analysis. Blood is a non-Newtonian fluid, the rheology and particularly viscosity of which largely depend upon the hematocrit, acute-phase protein concentration, temperature, and the shear properties.

Red cell aggregation is the prime factor in whole blood viscosity at a low shear rate. It is a reversible process caused by large proteins, e.g. fibrinogen and immunoglobulins, by bridging between the cells. Red blood cell deformability also plays an important role in blood rheology. It is defined by the mechanical properties of the cell membrane and the cell-content viscosity. In microcirculation, red-cell deformability and plasma viscosity are the main determinants of resistance to flow.

In the pathophysiology of vascular diseases, blood viscosity is a major factor, with implications for cardiovascular hemodynamics and tissue perfusion. An elevated blood viscosity also increases the thromboembolic risk and can be correlated with systemic inflammatory activities.

Performing an electrical analysis of blood, which is discussed in Chapter 3, provides the opportunity to derive a number of blood rheological properties. Among them, hematocrit and whole blood viscosity are found.

The above-listed considerations have become the basis for the HemoCard Vision system development, which is described in Chapter 4. The system is optimized to perform the electrical analysis of whole blood in the frequency range from 20 kHz to 1.2 MHz by using a four-electrode impedance sensor. This approach has the potential of detecting hematocrit and whole blood viscosity by measuring plasma resistance R_p and cell membrane capacitance C_m, respectively. The impedance sensor, which is positioned inside the right atrium, captures the intracardiac ECG as well. Additionally, the core body temperature is detected by a thermistor incorporated at the tip of the catheter.

The R_p and C_m measurements are synchronized with the detected ECG signal and are taken ideally at the end of diastole, just before the atrial contraction. At that moment the right atrium is completely filled with blood and the measured blood electrical properties are least influenced by the proximity of the atrial wall. Furthermore, at this moment the flow in the atrium is low and hence the blood viscosity will be at its highest level.

A series of dedicated *in vitro* and *in vivo* studies have been conducted with the newly designed system, the outcomes of which are shown in Chapter 5. The *in vitro* studies resulted in correlating the blood electrical properties, plasma resistance R_p and cell membrane capacitance C_m, with the corresponding blood rheological properties.

The HemoCard Vision system has been successfully used in a limited *in vivo* human pilot study where it monitored peripheral blood hematopoietic stem cell transplant (HSCT) recipients after myeloablative therapy. The promising results show that it is possible to measure core body temperature, heart rate, blood viscosity and hematocrit reliably and continuously *in vivo* in awake patients. This can lead to a timely institution of therapy with the prospect of improving the outcome by preventing the development of life-threatening, infectious complications and by reliably

detecting inflammation in general, since whole-blood viscosity reflects the inflammatory level in blood.

Besides the HSCT recipients, other patient groups that are managed with a central venous catheter could also benefit from this innovation. These groups include patients in intensive care (after major surgery or after out-of-hospital cardiac arrest), immunocompromised patients, and patients with malignancies.

Samenvatting

Dit proefschrift beschrijft de ontwikkeling van een *in vivo* hematologisch en cardiologisch on-line diagnostisch system, genaamd HemoCard Vision. Het systeem bestaat uit een centraal-veneuze katheter, een elektronisch interface en gegevensverwerkende software. Op basis van directe meetgegevens en/of toegevoegde nabewerking daarvan bepaalt het systeem de inwendige lichaamstemperatuur, het intracardiale ECG, het hematocriet, en de viscositeit van bloed.

Hoofdstuk 2 beschrijft de concepten en klinische aspecten van de analyse van bloed. Bloed is een niet-Newtoniaanse vloeistof, waarvan de rheologische aspecten en in het bijzonder de viscositeit sterk afhangen van het hematocriet, de concentratie van acute-fase proteïne, de temperatuur en de snelheid van de bloedstroom (met name de "shearrate"). "Shearrate" staat voor de snelheid, waarmee 2 naast elkaar liggende vloeistoflaagjes over elkaar schuiven.

Aggregatie van rode bloedcellen is de primaire factor die bepalend is voor de bloedviscositeit bij lage schuifsnelheden. Het betreft hier een omkeerbaar proces dat wordt veroorzaakt door grote eiwitcellen, zoals fibrinogeen en immunoglobine, die de rode bloedcellen met elkaar verbinden.

Ook de vervormbaarheid van rode bloedcellen speelt een grote rol bij de stromingseigenschappen van bloed. Deze vervormbaarheid hangt af van de mechanische eigenschappen van de celwanden en de viscositeit van de cel-inhoud. Vervormbaarheid van rode bloedcellen en plasmaviscositeit vormen de doorslaggevende factoren voor weerstand tegen stroming in de microcirculatie.

In de pathofysiologie van hart- en vaatziekten is de viscositeit van bloed een belangrijke factor vanwege de implicaties, die ze heeft met betrekking tot de dynamica van bloed in hart en bloedvaten en de microcirculatie in weefsel. Een verhoogde bloedviscositeit verhoogt ook de kans op trombose en is gecorreleerd met systemische ontstekingsactiviteit.

Het uitvoeren van een analyse van de elektrische eigenschappen van bloed, welke worden besproken in Hoofdstuk 3, geeft de gelegenheid om een aantal daarmee gecorreleerde eigenschappen met betrekking tot bloeddoorstroming te bepalen, waaronder hematocriet en bloedviscositeit.

De bovengenoemde beschouwingen vormden de basis voor de ontwikkeling van het HemoCard Vision systeem, dat beschreven is in Hoofdstuk 4.

Dit systeem is geoptimaliseerd om een analyse van de elektrische eigenschappen van bloed uit te voeren voor het frequentiebereik van 20 kHz tot 1.2 MHz met gebruikmaking van een vier-elektroden impedantiesensor. Hierdoor is het mogelijk om hematocriet en bloedviscositeit te bepalen door meting van respectievelijk de plasmaweerstand R_p en de celmembraamcapaciteit C_m. De impedantiesensor, die in het rechteratrium wordt geplaatst, meet eveneens het ECG. In aanvulling hierop wordt met een thermistor, die geplaatst is in de punt van de katheter, ook de temperatuur gemeten.

De metingen van R_p en C_m zijn gesynchroniseerd met het gedetecteerde ECG-signaal en worden idealiter bepaald aan het einde van de diastole, vlak voor de atriale contractie. Op dat moment is het atrium volledig gevuld met bloed en hierdoor worden de gemeten elektrische eigenschappen van het bloed het minst beïnvloed door de nabijheid van de wand van het atrium. Bovendien is op dat moment de bloedstroom in het atrium laag en zal daardoor de viscositeit van bloed het hoogste zijn.

Met de nieuw ontworpen systemen zijn een serie specifieke *in vitro* en *in vivo* studies uitgevoerd. De uitkomsten van deze studies worden in Hoofdstuk 5 besproken.Met de resultaten van de *in vitro* studies kon de

correlatie tussen de plasmaweerstand R_p en de celmembraamcapaciteit C_m met derheologische eigenschappen van bloed worden vastgesteld.

Het HemoCard Vision systeem is succesvol gebruikt bij een beperkt aantal *in vivo* menselijke proefonderzoeken, met name voor het monitoren van bloed bij ontvangers van stamcel-transplantatie (HSCT) na myeloablatieve therapie. De positieve resultaten tonen aan, dat met het beschreven systeem de mogelijkheid bestaat om bij wakkere patiënten op betrouwbare wijze en continu *in vivo* metingen te verrichten van de inwendige lichaamstemperatuur, de hartslag, de bloedviscositeit en het hematocriet. Dit kan helpen om in een vroege fase therapie te starten, waarmee het optreden van levensbedreigende infectueuze complicaties kan worden voorkomen; immers de viscositeit van bloed is een goede weerspiegeling van de mate van systemische inflammatie.

Naast HSCT patiënten kunnen ook andere patiëntgroepen, bij wie een centraal veneuze katheter geïndiceerd is, voordeel hebben van deze vernieuwing. Deze groepen omvatten patiënten op de intensive care (na grote operaties of na out-of-hospital resuscitatie), immuun gecompromitteerde patiënten, en patiënten met maligniteiten.

List of publications

Blagoy P. Iliev, Stoyan N. Nihtianov, Georgi P. Shterev and Gerard C. M. Meijer, “Interface System for Impedance Measurement Based on a Relaxation Oscillator”, National Scientific and Applied Science Conference ELECTRONICS - ET'2000, Sozopol, Bulgaria, 20-22 September, 2000

Blagoy P. Iliev, Stoyan N. Nihtianov, Georgi P. Shterev and Gerard C. M. Meijer, “A Multi-Period Interface System for Impedance Measurements”, Sensor for Industry Conference, 2001, Proceedings of the First ISA/IEEE Conference SIcon'01, Rosemount, Illinois, USA, 5-7 November, 2001

Blagoy P. Iliev, Dr. Gheorghe A. M. Pop and Gerard C. M. Meijer, “low-cost System for Measuring Plasma Resistance”, National Scientific and Applied Science Conference ELECTRONICS - ET'2001, Sozopol, Bulgaria, 26-28 September, 2001

Blagoy P. Iliev, Gerard C. M. Meijer, “Electrical Characterization of Rockwool Substrates“, National Scientific and Applied Science Conference ELECTRONICS - ET'2003, Sozopol, Bulgaria, 24-26 September, 2003

Blagoy P. Iliev, Gerard C. M. Meijer, “An Impedance-Measurement System for Electrical Characterization of Rockwool Substrates”, Sensor for Industry Conference, 2004, New Orleans, Louisiana, USA, 27-29 January, 2004

Blagoy P. Iliev, V. P. Iordanov, J. Bastemeijer, A. Bossche, P. M. Sarro, I. T. Young, G. W. K. van Dedem, M. J. Vellekoop, “Integrated nanoliter sensors reactor chamber for PCR analysis - from the idea to a complete system”, The Sense of Contact VI - Sensor Workshop for Industry and Science, Wageningen, The Netherlands, 23 Mart, 2004

Blagoy P. Iliev, Zu-yao Chang, Gheorghe A. M. Pop and Gerard C. M. Meijer, “In-vitro and in-vivo plasma Resistance measurement system”, The Sense of Contact VII - Sensor Workshop for Industry and Science, Wageningen, The Netherlands, 31 Mart and 1 April, 2005

Blagoy P. Iliev, Gheorghe A. M. Pop and Gerard C. M. Meijer, “In-vivo Blood Characterization System”, Proceedings of the IEEE Instrumentation and Measurement Technology Conference, Sorrento, Italy, 2006, pp 1781-1785

Blagoy P. Iliev, Gheorghe A. M. Pop and Gerard C. M. Meijer, “Catheter-based measurement system for blood analysis in vivo”, The Sense of Contact VIII - Sensor Workshop for Industry and Science, Wageningen, The Netherlands, 28 of March, 2006

Blagoy P. Iliev, A. Herbers, J.P. Donnelly, N. Blijlevens and G. Pop, “Measuring in-vivo hemorheological parameters online with a central venous catheter in the right atrium”, 13th International Congress of Biorheology and 6th International Conference on Clinical Hemorheology, Penn State University, USA, July 9-13, 2008

S. N. Nihtianov, G. P. Shterev, **B. P. Iliev** and Gerard C. M. Meijer, “A Novel Technique to Measure Two Independent Components of Impedance Sensors With a Simple Relaxation Oscillator”, Proc. IEEE Instrumentation and Measurement Conference' 2000, Baltimore, USA, 1-4 May, 2000

S. N. Nihtianov, G. P. Shterev, **B. P. Iliev** and Gerard C. M. Meijer, “An interface Circuit for R-C Impedance Sensors with a Relaxation Oscillator”, Proc. IEEE Instrumentation and Measurement Conference' 2000, Baltimore, USA, 1-4 May, 2000

S. N. Nihtianov, G. P. Shterev, **B. P. Iliev** and Gerard C. M. Meijer, “An interface Circuit for R-C Impedance Sensors with a Relaxation Oscillator”, Instrumentation and Measurement, IEEE Transactions, Volume: 50 Issue: 6, Dec. 2001, Page(s): 1563-1567

V. P. Iordanov, **B. P. Iliev**, Victor Joseph, Andre Bossche, Jeroen Bastemeijer, Pasqualina M. Sarro, Ian T. Young, Gijs W. K. van Dedem and Michiel J. Vellekoop, “Sensorized nanoliter reactor chamber for DNA multiplication”, IEEE Sensors 2004, Vienna, Austria, 24-27 October 2004

V. P. Iordanov, **B. P. Iliev**, Victor Joseph, Andre Bossche, Jeroen Bastemeijer, Pasqualina M. Sarro, Ian T. Young, Gijs W. K. van Dedem and Michiel J. Vellekoop, “Integrated Sensor Arrays for Bioluminescence and Fluorescence Bio-Chemical Analysis”, IEEE Sensors 2004, Vienna, Austria, 24-27 October 2004

V. P. Iordanov, **B. P. Iliev**, J. Bastemeijer, A. Bossche, P. M. Sarro, I. T. Young, H. Dietrich, R. van den Doel, G. W. K. van Dedem, A. Kroon, M. J. Vellekoop, “Integrated sensors for nanoliter bioluminescence and fluorescence bio-chemical analysis”, The Sense of Contact VI - Sensor Workshop for Industry and Science, Wageningen, The Netherlands, 23 mart, 2004

V. P. Iordanov, **B. P. Iliev**, J. Bastemeijer, A. Bossche, P. M. Sarro, I. T. Young, G. W. K. van Dedem, M. J. Vellekoop, “Integrated nanoliter sensors reactor chamber for DNA multiplication - thermal characterization”, The Sense of Contact VI - Sensor Workshop for Industry and Science, Wageningen, The Netherlands, 23 mart, 2004

D. Tanase, **B. P. Iliev**, J.F.L. Goosen, Z. Chang, G.A.M. Pop, J.M.M. Verwiel, C.J. Slager, P.J. Trimp, L. Pakula1, G.C.M. Meijer, P.J. French, “Investigation of multi-sensor techniques for cardiac-output measurements in intensive care”, 3rd IEEE/EMBS Special Topic

Conference on Micro-technology in Medicine and Biology, 2005, pp 122-125

Zu-yao Chang, **B. P. Iliev** and Gerard C. M. Meijer, “High- and low-frequency model of blood impedance”, The Sense of Contact VII - Sensor Workshop for Industry and Science, Wageningen, The Netherlands, 31 Mart and 1 April, 2005

Zu-yao Chang, **B. P. Iliev**, J. Frank de Groot and Gerard C. M. Meijer, “Extending the Limits of a Capacitive Soil-Water-Content Measurement”, Proc. IEEE Instrumentation and Measurement Conference' 2005, Ottawa, Ontario, Canada, 17-19 May, 2005

Zu-yao Chang, **B. P. Iliev**, J. Frank de Groot and Gerard C. M. Meijer, “Extending the Limits of a Capacitive Soil-Water-Content Measurement”, Instrumentation and Measurement, IEEE Transactions, Volume: 56 Issue: 6, Dec. 2007, Page(s): 2240-2244

Zu-yao Chang, **B. P. Iliev**, Gerard C. M. Meijer, “A Sensor Interface System for Measuring the Impedance (Cx, Rx) of Soil at a Signal Frequency of 20MHz”, Proceedings of the IEEE SENSORS 2007 Conference, Atlanta, Georgia, USA, October 28-31, 2007

A. Firouzian, D. Tanase, **B. P. Iliev**, Z. Chang, W. A. van Duyl, and P. J. French, “Planar Sensor Structures for Whole Blood Viscosity Measurements”, Proceedings of the SAFE, Veldhoven, The Netherlands, 2006, pp 151-154

Gerard C.M. Meijer, Xiujun Li, Zu-Yao Chang and **B. P. Iliev**, “Smart Capacitive-Resistive Sensors”, Proceeding of the International Conference on Computer Systems and Technologies ICEST 2007, Ohrid, Macedonia, 2007

Gerard C.M. Meijer, Xiujun Li, Zu-yao Chang and **Blagoy P. Iliev**, “Dedicated Impedance Sensors with Reduced Influence of Undesired Physical Effects”, The 9th International Symposium on Measurement Technology and Intelligent Instruments ISMTII-2009, 29 June - 2 July 2009, Saint-Petersburg, Russia

About the author

Blagoy Petrov Iliev was born in Smolyan, Bulgaria in 1976. He studied in Technical University Sofia, Branch Plovdiv, Bulgaria in the Faculty of Electronics and Automatics, where he received his M.Sc. degree in 2000. His subject of education was Automatics, Information and Control Systems. From 2000 to 2006 he spent his time developing impedance measurement techniques for the oilfield, agricultural and medical industries in the Electronic Instrumentation Laboratory at Delft University of Technology. In December 2006 he joined Martil Instruments where he works as R&D engineer responsible for the development of a catheter-based *in vivo* blood analysis system.

Propositions accompanying the thesis

In Vivo Blood Analysis System

by Blagoy P. Iliev
Delft, January 17th, 2012

1. The apparent whole blood viscosity at a specific location in the circulatory system can only be measured if the sensor is positioned exactly at the location of interest.

2. An *in vivo* whole-blood viscosity measurement can never be truly compared to a golden standard *in vitro* reference instrument measurement.

3. The effective shear rate inside a vessel increases when a sensing element is implanted.

4. *In vivo* hematocrit measurements pose fewer challenges than *in vivo* whole blood viscosity measurements.

5. Sensor positioning is the most challenging aspect of the *in vivo* electrical analysis of whole blood.

6. Stainless steel is more suitable than platinum or gold for measuring the electrical properties of liquids at low frequencies.

7. Health insurers should also be required to take the Hippocratic Oath.

8. Nowadays, teamwork becomes more and more like extraterrestrial life, most of us believe in it, yet it is very difficult to prove that it exists.

9. Globalization will never exist naturally because, luckily, we people are all socially different.

10. Walking through town with a modern single-lens reflex camera hanging from your shoulder makes your day better. The locals simply think you are a tourist and treat you with the appropriate level of respect.

These propositions are considered defendable and as such have been approved by the supervisor Prof. dr. ir. G. C. M. Meijer

Stellingen behorende bij het proefschrift

In Vivo Blood Analysis System

door Blagoy P. Iliev
Delft, 17 januari 2012

1. De bloedviscositeit op een specifieke plek in de bloedsomloop kan slechts worden gemeten als de sensor precies is gepositioneerd op de plaats van belang.

2. Een *in vivo* meting van bloedviscositeit kan nooit volledig worden vergeleken met een *in vitro* meting middels een gouden-standaard referentie instrument.

3. De effectieve schuifsnelheid binnenin een bloedvat neemt toe indien een sensorelement is geïmplanteerd.

4. Het meten *in vivo* van hematocriet levert minder problemen op dan het meten *in vivo* van de viscositeit van bloed.

5. Het meest uitdagende aspect van een *in vivo* elektrische analyse van bloed betreft de plaatsing van de sensor.

6. Voor het meten van elektrische eigenschappen van vloeistoffen bij lage frequenties is roestvrij staal een meer geschikt elektrodemateriaal dan platina of goud.

7. Ook gezondheidsverzekeraars zouden de eed van Hippocratius moeten afleggen.

8. Tegenwoordig lijkt teamwerk hoe langer hoe meer op buitenaards leven. Velen geloven erin, maar het is moeilijk om aan te tonen dat het werkelijk bestaat.

9. Globalisatie zal nooit op een natuurlijke wijze bestaan omdat wij mensen gelukkig allemaal in sociaal opzicht verschillen.

10. Wandelen door de stad met een moderne spiegelreflexcamera hangend van je schouder maakt je dag beter. De lokale mensen denken eenvoudig dat je toerist bent en behandelen je met bijbehorend respect.

Deze stellingen worden verdedigbaar geacht en zijn als zodanig goedgekeurd
door de promotor Prof. dr. ir. G. C. M. Meijer